Multiphoton Ionization of Atoms by an Ultrashort Laser Pulse

V. S. Popov

*Institute of Theoretical and Experimental Physics, ul. Bol'shaya Cheremushkinskaya 25,
Moscow, 117218 Russia*

Closed analytical expressions for the probability of multiphoton ionization of atoms and ions by a time-varying electric field $\mathscr{E}(t)$ are obtained by the imaginary time method. These expressions apply for arbitrary values of the Keldysh parameter γ. The dependence of the ionization probability and the photoelectron momentum spectrum on the shape of an ultrashort laser pulse is considered. © *2001 MAIK "Nauka/Interperiodica".*

PACS numbers: 32.80.Rm; 32.80.Fb; 31.15.Gy

The generation of more and more intense electromagnetic fields is associated with the shortening of a laser pulse [1–3] whose duration becomes comparable with the optical period (see, e.g., [2–4] and references cited in [4]), so that the spectrum contains many higher harmonics. Being highly nonlinear, the multiphoton ionization process [5–7] cannot be reduced to the sum of contributions from individual harmonics. Besides, the ionization probability and the momentum spectrum of emitted photoelectrons depend strongly on the pulse shape, especially in the region $\gamma \gtrsim 1$. The revelation of this dependence becomes necessary for the analysis of experimental data.

In this connection, the problem of atomic ionization in an arbitrarily time-varying electric field (uniform in space and linearly polarized)

$$\mathscr{E}(t') = F\varphi(t), \quad t = \omega t' \tag{1}$$

will be considered in this work. In Eq. (1), F is the field amplitude, ω is its characteristic frequency, and t is the dimensionless time; the function φ specifies the pulse shape and satisfies the conditions $\varphi(-t) = \varphi(t)$ and $|\varphi(t)| \leq \varphi(0) = 1$ at $-\infty < t < \infty$ ($t = 0$ is the time instant where the field is maximal and an electron leaves the barrier). The calculations are carried out by the semiclassical imaginary time method [7, 8], which adequately describes the tunneling of particles through rapidly oscillating barriers. In this method, the subbarrier trajectories formally satisfying classical equations of motion (but with imaginary "time") are introduced. The main (exponential) factor in the ionization probability is determined by the so-called extremal subbarrier trajectory, for which the imaginary part $\text{Im}S$ of the action function is maximal (and which determines, according to Feynman [9, 10], the most probable trajectory of the tunneling particle). To find the momentum

spectrum of emitted electrons, the quadratic correction $\propto (\mathbf{p} - \mathbf{p}_{\max})^2$ to $\text{Im}S$ should be calculated for a bundle of classical trajectories close to the extremal one (see [8, 11] for more details).

It is assumed that the conditions

$$K_0 = \frac{I}{\hbar\omega} \gg 1, \quad \epsilon = \frac{e\hbar F}{(2I)^{3/2}m^{1/2}} = \frac{F}{\kappa^3 F_a} \ll 1, \tag{2}$$

ensuring the applicability of the semiclassical approach to the multiphoton processes, are fulfilled. Here, K_0 is the multiquantum parameter, ϵ is the reduced electric field, $I = \kappa^2 m e^4/2\hbar^2$ is the ionization potential, and κ is the characteristic dimensionless momentum in the bound state.[1] The tunneling process strongly depends on the Keldysh parameter [5] γ:

$$\gamma = \omega/\omega_t = \omega\sqrt{2mI}/eF, \tag{2'}$$

where ω_t is the tunneling frequency in the field F. In what follows, atomic units are used: $\hbar = m = e = 1$ (m is the electron mass, and $F_a = m^2 e^5/\hbar^4 = 5.14 \times 10^9$ V/cm).

It is clear from physical considerations that the extremal trajectory in field (1) is one-dimensional and directed along the field. By solving the equations of motion and evaluating $\text{Im}S$, one obtains for the proba-

---

[1] For the ground states of neutral atoms, parameter κ varies from 0.535 for Cs ($I = 3.89$ eV) to 1.344 for He ($I = 24.59$ eV; see [12] and [11, Table 1]). For the weakly bound states, it may be much less than unity. For example, $I = 0.754$ eV and $\kappa = 0.235$ for the negative hydrogen ion, $I = 0.077$ eV and $\kappa = 0.075$ for the He$^-$ ion, etc. In these cases, the values of reduced field ϵ and the ionization probabilities markedly increase (at a fixed F value).

bility of multiphoton ionization (to a preexponential factor)

$$w_i(\mathbf{p}) \equiv dw_i/d^3p \propto \exp\left\{-\frac{2}{3\epsilon}g(\gamma)\right.$$

$$\left.-\frac{\kappa}{F}[b_1(\gamma)(p_\parallel - p_{max})^2 + b_2(\gamma)p_\perp^2]\right\}, \quad (3)$$

where $p_\parallel$ and $p_\perp$ are, respectively, the longitudinal (with respect to the field) and transverse momenta of the emitted photoelectron and p_{max} is its most probable momentum,

$$g(\gamma) = \frac{3}{2}\int_0^1 \chi(\gamma z)(1-z^2)dz, \quad b_1(\gamma) = b_2(\gamma) - \chi(\gamma),$$

$$b_2(\gamma) = \int_0^1 \chi(\gamma z)dz = \gamma^{-1}\tau(\gamma), \quad p_{max} = \frac{F}{\omega}\int_0^\infty \varphi(t)dt. \quad (4)$$

After determining the function $\chi(z)$ that depends on pulse shape (1), the problem reduces to quadratures. This function can be defined parametrically

$$\chi = 1/\tilde{\varphi}(\tau), \quad z = h(\tau) \equiv \int_0^\tau \tilde{\varphi}(t)dt, \quad (5)$$

where $\tilde{\varphi}(t) \equiv \varphi(it)$. The last equation in (5) also determines the inverse function $\tau(z) = h^{-1}(z)$ (in the implicit form). The "initial moment" of the subbarrier motion of an electron is

$$t_0' = i\omega^{-1}\tau(\gamma). \quad (6)$$

In the tunneling limit $\gamma \ll 1$ (low-frequency laser field), the ionization occurs at times close to $t = 0$. Assuming that

$$\varphi(t) = 1 - \frac{a_2}{2!}t^2 + \frac{a^4}{4!}t^4 - \frac{a^6}{6!}t^6 + \dots, \quad a_2 > 0 \quad (7)$$

at $t \longrightarrow 0$, one finds from Eq. (5) that

$$\chi(z) = \sum_{n=0}^\infty (-1)^n \frac{\chi_n}{(2n)!}z^{2n}, \quad \chi_0 = 1, \quad \chi_1 = a_2, \quad (7')$$

$$\chi_2 = 10a_2^2 - a_4, \quad \chi_3 = a_6 - 56a_4a_2 + 280a_2^3, \dots.$$

Then, using Eq. (4), one obtains the expansions

$$g(\gamma) = 1 + \sum_{n=1}^\infty (-1)^n g_n \gamma^{2n},$$

$$g_n = \frac{3}{(2n+1)!(2n+3)}\chi_n,$$

$$b_1(\gamma) = \sum_{n=0}^\infty (-1)^n \frac{\chi_{n+1}}{(2n+1)!(2n+3)}\gamma^{2n+2}, \quad (8)$$

$$b_2(\gamma) = \sum_{n=0}^\infty (-1)^n \frac{\chi_n}{(2n+1)!}\gamma^{2n},$$

which permit the calculation of adiabatic corrections. In the first approximation in γ^2, the dependence of Eq. (3) on the pulse shape is universal:

$$w_i(\mathbf{p}) \propto \exp\left\{-\left[\frac{2\kappa^3}{3F}\left(1 - \frac{a_2}{10}\gamma^2\right)\right.\right.$$

$$\left.\left.+ \frac{\kappa}{F}\left(\frac{1}{3}a_2\gamma^2(p_\parallel - p_{max})^2 + p_\perp^2\right)\right]\right\}, \quad (9)$$

where $a_2 = -\varphi''(0)$ is the pulse curvature near its top. In Eq. (9), $\Delta p_\perp \sim \sqrt{\epsilon}\,\kappa \ll \kappa$ and $\Delta p_\parallel \sim \gamma^{-1}\Delta p_\perp \sim \sqrt{\epsilon}\,F/\omega$. In this case, the longitudinal momentum of an electron is much larger than its transverse momentum, because it is accelerated along the slowly varying electric field $\mathcal{E}(t)$.

In the other limit ($\gamma \gg 1$), it is convenient to recast Eq. (3) in the form

$$w_i(\mathbf{p}) \propto \exp\left\{-\left[\frac{\kappa^2}{\omega}f(\gamma) + \frac{1}{\omega}(c_1 p_\parallel^2 + c_2 p_\perp^2)\right]\right\}, \quad (10)$$

where

$$\kappa^2/\omega = 2K_0 \gg 1, \quad f(\gamma) = \frac{2}{3}\gamma g(\gamma),$$

$$\text{and} \quad c_{1,2}(\gamma) = \gamma b_{1,2}(\gamma).$$

In physical problems, the function $f(\gamma)$ either tends to a constant limit at $\gamma \longrightarrow \infty$ [if the function $\varphi(t)$ has a singularity in the complex plane at a finite distance from the real time axis] or increases logarithmically. Let us consider some characteristic examples.

(1) Monochromatic laser light corresponds to $\varphi(t) = \cos t$. In this case, $\chi(z) = (1 + z^2)^{-1/2}$, and the integrals in Eqs. (4) are tabular and give[2]

$$f(\gamma) = \left(1 + \frac{1}{2\gamma^2}\right)\text{arcsinh}\gamma - \frac{\sqrt{1+\gamma^2}}{2\gamma},$$

$$c_1 = \text{arcsinh}\gamma - \gamma/\sqrt{1+\gamma^2}, \quad (11)$$

$$c_2 = \tau_0(\gamma) = \text{arcsinh}\gamma, \quad p_{max} = 0.$$

---

[2] A comparison with [5–7] demonstrates how much the use of Eqs. (4)–(6) obtained by the imaginary time method simplifies the calculation.

(2) For a solitonlike pulse with $\varphi(t) = 1/\cosh^2 t$, one has $\chi(z) = (1 + z^2)^{-1}$, whence

$$f(\gamma) = (1 + \gamma^{-2})\arctan\gamma - \gamma^{-1},$$

$$c_1 = \arctan\gamma - \gamma/(1 + \gamma^2), \quad c_2 = \arctan\gamma. \qquad (12)$$

(3) For a Gaussian pulse, $\varphi(t) = \exp(-t^2/2\sigma^2)$, the function $\chi(z)$ is found from the equation

$$\chi^{-1}w(\sqrt{-\ln\chi}) = z/\sqrt{2}\sigma, \quad 0 < \chi \leq 1, \qquad (13)$$

where

$$w(z) = e^{-z^2}\int_0^z e^{u^2}du$$

is the well-known Doson integral. Further calculations by Eqs. (4) are straightforward.[3]

(4) For the pulse field

$$\varphi(t) = (1 + t^2)^{-\alpha}, \quad \alpha > 1, \qquad (14)$$

Eqs. (5) take the form

$$\chi = (1 - \tau^2)^{\alpha}, \quad z = \tau F(\alpha, 1/2; 3/2; \tau^2), \qquad (15)$$

where $0 \leq \tau < 1$ and $F(\ldots) \equiv {}_2F_1(\ldots)$ is the hypergeometric Gauss function. At $\gamma \longrightarrow \infty$, the initial point $t_0 = i\tau_0(\gamma)$ approaches the singularity $t_s = i$ of field (14):

$$\tau_0(\gamma) = \begin{cases} 1 - 2\exp(-2\gamma) + \ldots, & \alpha = 1, \\ 1 - k\gamma^{-1(\alpha-1)} + \ldots, & \alpha > 1, \end{cases} \qquad (15')$$

where $k = [2^{\alpha}(\alpha - 1)]^{-1/(\alpha-1)}$. This example is typical for those cases where the nearest singularity $t_s = i\tau_s$ of the field function $\varphi(t)$ lies at a finite distance from the real axis and is a pole ($\alpha = 1, 2, \ldots$) or a power-type branch point. In this case, Eq. (10) takes the asymptotic form

$$w_i(\mathbf{p}) \propto \exp\left\{-\frac{\tau_s}{\omega}[\kappa^2 + (p_{\parallel} - p_{max})^2 + p_{\perp}^2]\right\}, \qquad (16)$$

$$\gamma \gg 1,$$

and, therefore, $w_i = \int w_i(\mathbf{p})d^3p \propto \exp(-2K_0\tau_s)$, which is much higher than the probability $w_i \propto \exp(-2K_0\ln 2\gamma)$ of ionization by the monochromatic field. The respective photoelectron distribution is nearly isotropic (about the point $\mathbf{p}_{max}$ in the momentum space): $\Delta p_{\parallel} \approx \Delta p_{\perp} \sim \sqrt{\omega/\tau_s} \ll \kappa$.

---

[3] Note that the individual terms in the expressions for $f(\gamma)$ and $g(\gamma)$ at $\gamma \longrightarrow 0$ tend to infinity (they cancel each other). For this reason, to obtain the expansions in the adiabatic region $\gamma \ll 1$, it is more convenient to use Eqs. (8) than the exact formulas of the type (11) or (12).
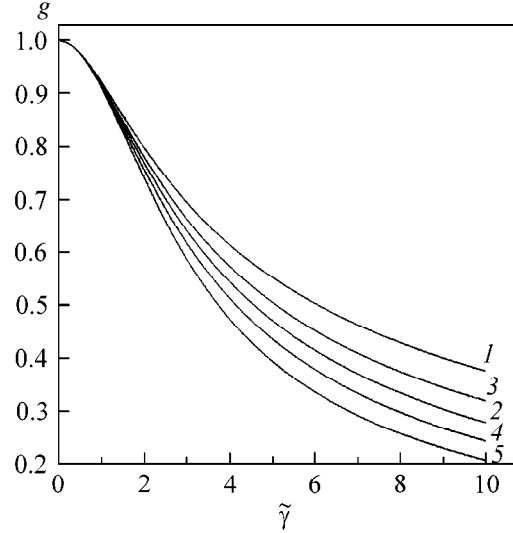
Fig. 1. The functions $g(\gamma)$ for the fields of form (1). Lines *1–3* correspond to the respective examples; (*4*) $\varphi = (1 + t^2)^{-3/2}$ and (*5*) $\varphi = (1 + t^2)^{-1}$. The scaled variable $\tilde{\gamma} = \sqrt{a_2}\,\gamma$ is plotted on the abscissa, where a_2 is the coefficient in expansion (7).

An analytical solution is also possible for $\varphi(t) = 1/\cosh t$, $(1 + t^2)^{-1}$ (Lorentzian pulse shape), $(1 - t^2)/(1 + t^2)^2$, $(1 + t^2)^{-3/2}$, $(\cosh^2 t + \beta^2\sinh^2 t)^{-1}$ for $0 < \beta < \infty$, etc. For any physically reasonable pulse shape $\varphi(t)$, the numerical calculation by Eqs. (4)–(6) is not a problem.

Let us now discuss the numerical results. Functions $g(\gamma)$ for several pulse fields are presented in Fig. 1, where this function is also shown for a monochromatic field for comparison (curve *1*). The time axis is scaled so that all pulses have the same curvature at the top $[\varphi''(0) = -1]$, which corresponds to passing from the parameter γ to $\tilde{\gamma} = \sqrt{a_2}\,\gamma$, where a_2 is the coefficient in Eq. (7). Figures 2 and 3 refer to a modulated light pulse of the form

$$\varphi(t) = \exp\left\{-\frac{t^2}{2\sigma^2}\right\}\cos t, \qquad (17)$$

which is close to the real experiment. Here, one has for small γ

$$g(\gamma) = 1 - \frac{1}{10\sigma^2}(1 + \sigma^2)\gamma^2$$

$$+ \frac{1}{280\sigma^4}(9\sigma^4 + 14\sigma^2 + 7)\gamma^4 + \ldots. \qquad (18)$$

With a decrease in σ, the pulse shortens; its amplitude decreases by a factor of $\delta \approx \exp(-2\pi^2/\sigma^2)$ per one period of the laser field. The functions $g(\gamma)$ and $f(\gamma)$ also decrease, resulting, due to Eqs. (2), in a sharp increase
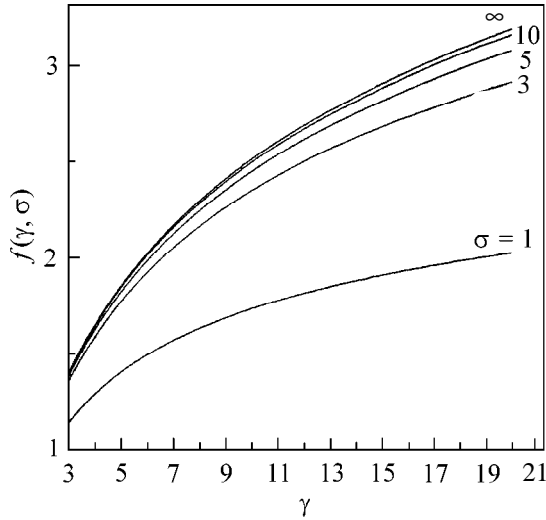
Fig. 2. The function $f(\gamma, \sigma)$ from Eq. (10) for field (17). The lines correspond to (from bottom to top) $\sigma = 1, 3, 5, 10$, and ∞.
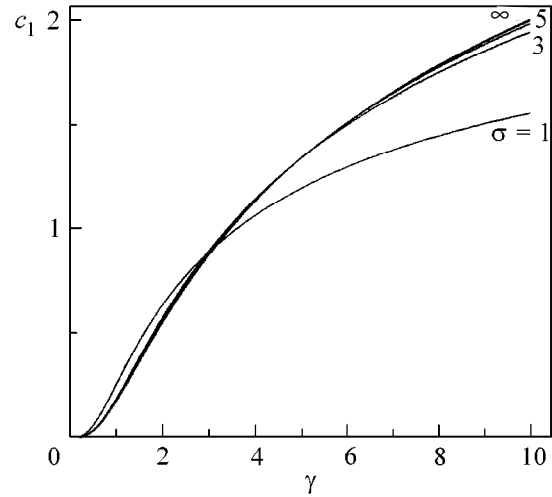

Fig. 3. The coefficient c_1 of the momentum spectrum vs. the parameter γ. The numbers near the lines are the σ values in Eq. (17).

in the ionization probability, especially in the $\gamma \gtrsim 1$ region (rapidly varying fields). As is seen from Fig. 1, the same takes place when going from the monochromatic field to the pulse fields of various shapes concentrated at a finite time interval. Thus, the pulse shortening leads to an increase in the ionization probability. Physically, this is caused by an increase in the weight of higher harmonics ω_n in the pulse spectrum, because they can ionize atoms even in the first order of perturbation theory if $\omega_n > I$ (whereas monochromatic light does not contain higher harmonics and, therefore, provides only the multiphoton ionization mechanism [5]). For field (17), this becomes noticeable at $\sigma \lesssim 10$, when the pulse covers $N \sim 2\sigma/\pi \sim 5$–10 periods of the laser field. As for the pulse spectrum shape, it follows from Fig. 3 that the dependence of the coefficient $c_1(\gamma, \sigma)$ on parameter σ can be neglected if $\sigma \gtrsim 3$ [the same is also true for the coefficient c_2 in Eq. (10)].

Similar results were obtained for the Lorentzian envelope, i.e., for

$$\varphi(t) = [1 + (2t/\sigma)^2]^{-1} \cos t. \qquad (19)$$

Here, as also for Eq. (17), the ionization probability monotonically increases with decreasing σ (i.e., with pulse shortening—see Fig. 4). However, Eqs. (17) and (19) are qualitatively different at large γ values, as directly follows from the analytical properties of the function $\varphi(t)$ in the complex plane. Namely, the functions $f(\gamma, \sigma)$ in Fig. 2 increase logarithmically with γ and tend to a constant limit $f(\gamma, \sigma) \longrightarrow \tau_s = \sigma/2$ for Eq. (19), as in the case of pulse (14).[4] This is explained by the fact that Eq. (17) is an entire function without

singularities in a finite part of the t plane, whereas Eq. (19) has a pole at the point $t = t_s = i\sigma/2$.

It should be emphasized that Eqs. (4)–(6) allow the calculation of all the quantities entering into the semiclassical formulas for $w_i(\mathbf{p})$ for an arbitrary pulse $\mathscr{E}(t)$ and for any γ value, thereby providing the possibility for a detailed comparison of multiphoton ionization theory with experiments with strong fields and ultrashort pulses.[5]

Note in conclusion that the imaginary time method can also be applied to the problem of electron–positron pair production from vacuum in the presence of a time-varying electric field (1). This problem formally differs from the problem considered above in that the subbarrier electron motion between the boundaries of the lower and upper continua is essentially relativistic and should be treated with the relativistic Lagrangian $L = -m\sqrt{1 - \dot{x}^2} + e\mathscr{E}(t)x$. In this case, the differential probability of pair production is represented by Eq. (3), in which the coefficient $2/3$ is replaced by π; $\epsilon = F/F_0$, where $F_0 = m^2 c^3/e\hbar$ is the "critical," or Schwinger, field [14], typical for QED; $\gamma = mc\omega/eF$; and

$$g(\gamma) = \frac{4}{\pi}\int_0^1 \chi(\gamma z)\sqrt{1 - z^2}\,dz = \frac{4}{\pi\gamma}\int_0^1 \frac{\tau(\gamma z)z}{\sqrt{1 - z^2}}\,dz, \quad (20)$$

while the expressions for the coefficients $b_1(\gamma)$ and $b_2(\gamma)$ are not presented. The similarity to Eq. (3) is apparent if it is considered that both formulas include the same functions χ and τ, which are uniquely determined by field shape (1), and that $\chi(z) = \tau'(z)$. However, the

---

[4] With an increase in σ, the region of establishing this asymptotic behavior is shifted to larger γ values, and, for $\sigma = \infty$, one has $f(\gamma) = \ln 2\gamma - 1/2 + O(\ln\gamma/\gamma^2)$, in accordance with Eq. (11).

[5] For monochromatic laser radiation, the energy, momentum, and angular distributions of photoelectrons were studied in detail in [13] over the entire range of the Keldysh parameter γ.
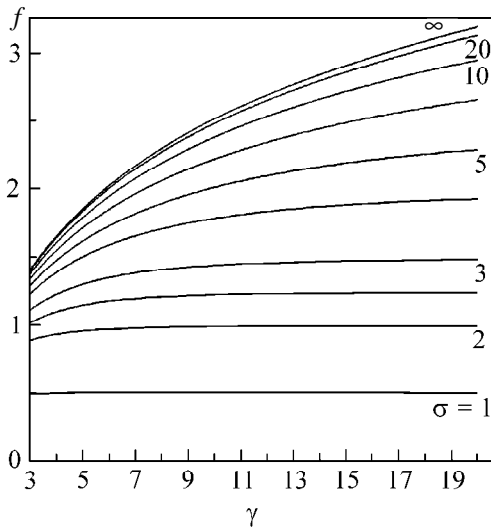
Fig. 4. The function $f(\gamma, \sigma)$ from Eq. (10) for a light pulse with Lorentzian envelope (19). The lines correspond to (from bottom to top) $\sigma = 1, 2, 2.5, 3, 4, 5, 6.67, 10, 20$, and ∞ (σ is the width of envelope at half maximum).

parameters F_0 and γ have quite a different order of magnitude, as compared to those in the atomic problem: $F_0/F_a = (\hbar c/e^2)^3 \approx 2.6 \times 10^6$. An immense value $F_0 = 1.32 \times 10^{16}$ V/cm indicates that the observation of this process is as yet far beyond the possibilities of experiments. However, in solid-state physics and, in particular, for semiconductors, the following dispersion law is used [5]:

$$\varepsilon(p) = \Delta(1 + p^2/m_*\Delta)^{1/2}, \qquad (21)$$

where m_* is the effective mass and Δ is the band gap separating the valence band from the conduction band. Formally, Eq. (21) has the same form as the formula $\varepsilon(p) = \sqrt{m^2 + p^2}$ for a free particle in relativistic mechanics. Therefore, after changing notations, formulas of type (20) can be used in the theory of multiphoton ionization of semiconductors by a laser pulse. For a monochromatic light field, this was already done in [5].

After this paper had been finished, it came to my attention that similar problems were considered in [4], where, in particular, solitonlike, Gaussian, and Lorent-

REFERENCES

1. F. J. McClung and R. W. Hellwarth, J. Appl. Phys. **33**, 888 (1962).

2. S. Dobosz, M. Lezius, M. Shmidt, *et al.*, Phys. Rev. A **56**, R2526 (1997).

3. N. Bloembergen, Rev. Mod. Phys. **71**, S283 (1999).

4. L. Keldysh, *Multiphoton Ionization by a Very Short Pulse* (in press).

5. L. V. Keldysh, Zh. Éksp. Teor. Fiz. **47**, 1945 (1964) [Sov. Phys. JETP **20**, 1307 (1964)].

6. A. I. Nikishov and V. I. Ritus, Zh. Éksp. Teor. Fiz. **50**, 255 (1966) [Sov. Phys. JETP **23**, 168 (1966)].

7. A. M. Perelomov, V. S. Popov, and M. V. Terent'ev, Zh. Éksp. Teor. Fiz. **50**, 1393 (1966) [Sov. Phys. JETP **23**, 924 (1966)]; Zh. Éksp. Teor. Fiz. **51**, 309 (1966) [Sov. Phys. JETP **24**, 207 (1967)].

8. V. S. Popov, V. P. Kuznetsov, and A. M. Perelomov, Zh. Éksp. Teor. Fiz. **53**, 331 (1967) [Sov. Phys. JETP **26**, 222 (1968)].

9. R. P. Feynman, Rev. Mod. Phys. **20**, 367 (1948).

10. R. P. Feynman and A. R. Hibbs, *Quantum Mechanics and Path Integrals* (McGraw-Hill, New York, 1965; Mir, Moscow, 1968).

11. V. S. Popov, B. M. Karnakov, and V. D. Mur, Zh. Éksp. Teor. Fiz. **113**, 1957 (1998) [JETP **86**, 860 (1998)].

12. A. A. Radtsig and B. M. Smirnov, *Reference Data on Atoms, Molecules, and Ions* (Énergoatomizdat, Moscow, 1986; Springer-Verlag, Berlin, 1985).

13. V. S. Popov, Pis'ma Zh. Éksp. Teor. Fiz. **70**, 493 (1999) [JETP Lett. **70**, 502 (1999)]; Zh. Éksp. Teor. Fiz. **118**, 56 (2000) [JETP **91**, 48 (2000)].

14. J. Schwinger, Phys. Rev. **82**, 664 (1951).

Translated by R. Tyapaev

Rydberg Matter as a Metastable State of Strongly Nonideal Plasma

G. É. Norman

Moscow Institute of Physics and Technology, Institutskiĭ per. 9, Dolgoprudnyĭ, Moscow region, 141700 Russia
e-mail: henry_n@orc.ru
Received November 15, 2000

The phase diagram of cesium is complemented by an isolated region of metastable states of a strongly nonideal plasma. © *2001 MAIK "Nauka/Interperiodica".*

PACS numbers: 52.27.-h; 64.60.My

1. Rydberg matter at $T = 0$. The concept of "Rydberg matter" is developed in [1–6]. By this term is meant a crystal at $T = 0$ formed from highly excited atoms (with the same principal quantum number n). The formulation of the mechanism responsible for the metastability of the Rydberg matter to the radiative recombination is a crucial achievement of the authors of [1–6]. The point is that the authors of [1–6] have recognized that the electron density distribution in the Rydberg matter is highly nonuniform: electrons are at the periphery of the Wigner–Seitz cell. Moreover, the domain of their residence is separated from the central region by a potential barrier. Therefore, the atomic ground-state wave functions do not overlap with the valence states of the Rydberg matter. Accordingly, the matrix element for the radiative recombination is virtually zero. The recombination proceeds only through the intermediate tunneling transition to the center of the Wigner–Seitz cell; i.e., it is slow, which is necessary for the metastability. The stability to Auger processes was also analyzed.

In [1–6], the principal quantum numbers were $n = 10$–20; i.e., the density of the Rydberg matter was equal to 10^{19}–10^{16} cm^{-3}. In other words, the Rydberg matter is a condensed state with gas density.

2. Experimental observations. The results [7, 8] are considered as an evidence for the existence of long-lived low-density condensed states. The concepts developed in [1–6] are compared with the observations [7, 8] in [5, 9].

A setup based on a thermionic converter was designed in [7, 8]. A container with metallic cesium at $T = 400$–420 K served as a source of cesium atoms. The excited cesium atoms were emitted from a graphite foil, $T = 1300$ K. The cesium atoms were excited upon impact on the emitter. The flux of excited atoms from the emitter was as high as 10^{15} cm^{-3} s^{-1}. In addition to the cesium atoms, clusters of approximately forty thousand cesium atoms were detected in the flux. These clusters were subsequently collected onto a trap cooled with liquid nitrogen. The resulting microflashes were about 0.5 mm in diameter and had a density of approximately 10^{18} cm^{-3}, i.e., typical of gas.

3. Phase state. The lifetimes of the microflashes observed in [7, 8] were equal to tens of seconds and even minutes before their radiative deexcitation. This is much longer than the time of establishing equilibrium over the internal degrees of freedom. One can thus introduce the notions of temperature, pressure, and specific volume, i.e., standard thermodynamic parameters. Since the energy was not delivered under the conditions of observation of the clusters and microflashes, the microflash state can be related to the metastable states that are considered in thermodynamics.

Point B in Fig. 1 corresponds to the observations [7, 8]. It is plotted on the conventional cesium phase diagram [10, 11] in density–temperature coordinates. The measured density is assigned to the final temperature of 70 K, while the initial state A is conventionally assigned to the temperature 1300 K and a slightly lower density, both points being connected by the assumed AB curve of the cooling process.

One can hardly expect that the metastable states are represented by a single point or curve. The authors of [7, 8] also assume that the Rydberg matter exists in a certain finite range of densities (or quantum numbers $n = 10$–14). For this reason, the metastable states in Fig. 1 are represented by a certain conventional region bounded by the dashed line. At low densities, this region is bounded due to the bond energy decrease that was found in [1–6]. The transition to higher densities would mean the transition to smaller n values. As a result, the boundary of the Wigner–Seitz cell approaches the central region, and the conditions ensuring, according to [1–6], the stability to radiative recombination are lost. At high temperatures, the region is bounded by the absolute level of bond energy that was found in [1–6].
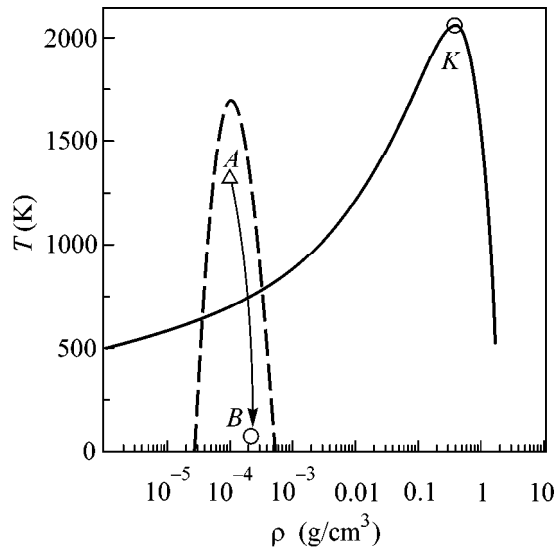
Fig. 1. Cesium phase diagram in density–temperature coordinates. Standard phase diagram: solid line is the liquid–saturated vapor coexistence curve; K is the critical point. Schematic representation of metastable states: A and B are the experimental microdrop states; AB arrow is the cooling path; dashed line bounds the isolated region of existence of the homogeneous metastable states of non-ideal plasma.
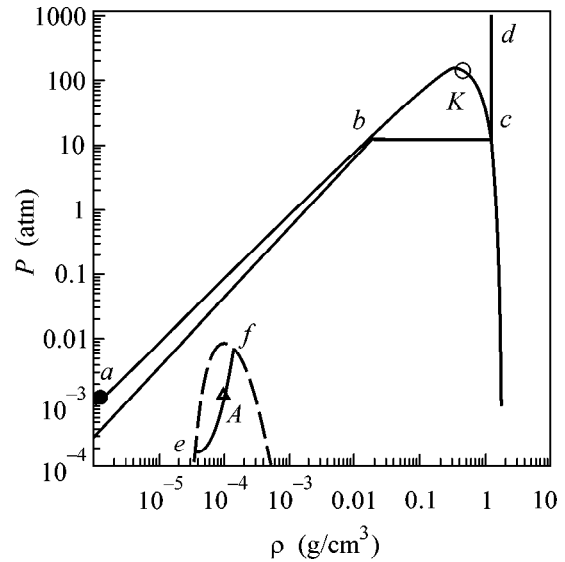
Fig. 2. Cesium phase diagram in density–pressure coordinates. The solid line, the point K, the triangle A, and the dashed line denote the same as in Fig. 1. 1300 K isotherm, $abcd$: (ab) vapor, (bc) two-component region, and (cd) liquid. eAf is the isolated segment of metastable states; points a and A correspond to the same pressure.

4. Isolated segment of isotherm. Point A in Fig. 2 corresponds to the observations [7, 8] and is plotted on the cesium phase diagram [10, 11] in density–pressure coordinates. This point [7, 8] is assigned a pressure of 1 torr. This value belongs to the pressure range that is typical of thermionic converters. The isotherm ($abcd$ + eAf) is schematically drawn for the conventional temperature of 1300 K. The eAf segment of the isotherm is bounded from the left by the point where $(dP/dv)_T = 0$ and from the right by the loss in stability against radiative recombination. As in Fig. 1, the possible metastable states are represented in Fig 2 by a certain conventional region bounded by the dashed line. Therefore, it follows from the results [7, 8] that an isolated segment eAf of metastable states exists at $T = 1300$ K, in addition to the main isotherm branch $abcd$. The same segments occur for any temperature near 1300 K and below.

The notion of isolated metastable segment of the $P(v)$ isotherm was introduced in [12] and discussed later in [13, 14]. The metastable states were considered for a supercooled nonideal plasma. The hypothesis [12–14] was based on the assumption about plasma phase transition [13, 15] (see also [16–18]). According to these ideas, the phase transitions may occur as a result of the competition between the Coulomb attraction of charges and their quantum repulsion at small distances. The situation is quite similar to the van der Waals equation, for which the phase transition is a result of the competition between the long-range attraction of molecules and their short-range repulsion. The only distinction is that plasma contains two sorts of

charged particles: electrons and ions, which, moreover, are in equilibrium with the particles of the third sort—atoms. The latter were assumed in [15] to be an ideal gas. Contrary to [15], the phase transition [15] considered in [12–14] occurs in the region where atoms do not form an ideal gas. For this reason, the phase transition [15] may disappear, while the segment of metastable states may be retained. Estimates show that such a segment may occur in the isotherms of various substances, e.g., air [12, 14] and cesium [13] at temperatures close to room temperatures.

Turning back to Figs. 1 and 2, let us emphasize that the solid curve passing through point K separates the regions of two-phase (below the curve) and one-phase (vapor on the left, liquid on the right, and fluid above) states. The dashed lines bound the region of existence of the homogeneous metastable states. This region superposes on the stable (one- or two-phase) states. Thus, the states bounded by the dashed lines are two-valued. For instance, rarefied vapor a coexists with a much denser nonideal plasma state A at the same pressure and temperature. The possibility of such a metastable state A coexisting with the stable state was discussed in [12, 13]. States like supercooled vapor or superheated liquid are absent because they cannot coexist with the stable state.

5. Unified approach. An analysis of the hypothesis [1–6] shows that it does not address the crystallinity of the Rydberg matter, because the calculations are based on the use of a density functional, while the Wigner–Seitz cell is taken to be spherical. Hence, the same cal-

culation may apply, with no changes, to the system with short-range order, dealt with in [12–14]. The only modification is that the radius of the Wigner–Seitz cell should then be equated to the mean distance between the charges rather than to the radius of the excited state. The estimate of the Madelung energy [12–14], like estimate [1–6], is independent of temperature, so that the approach [1–6] can be regarded as a quantum refinement of the classical Madelung estimate.

Although the radiative instability [1–6] is disregarded in the hypothesis [12–14], it can naturally be included in this hypothesis. Conversely, the concept [12–14] can be included in the hypothesis [1–6]. Both approaches complement each other and can be combined into a unified approach, which may lay claim to the theory of supercooled metastable dense-plasma states. These are the states of the type of condensed matter plasma with a density several orders of magnitude lower than the metal density. Accordingly, the degeneracy temperature becomes lower than its normal value. The experimental results [7, 8] can be considered as the confirmation of both concepts [1–6] and [12–14]. The metastable states may occur in the disordered (liquid) state at relatively high temperatures and in the crystal state at low temperatures.

6. The Manykin, Ozhovan, and Poluéktov Rydberg matter [1–6], the microflashes of Holmlid *et al.* [7, 8, 19, 20], and the plasma phase transition [12–14] are different facets of the same phenomenon. The presence of an isolated region of metastable nonideal plasma can hardly be restricted to cesium alone. The authors of [12–14] and [1–6] considered this to be the general property. The authors of [7, 8] also observed microdrops for various substances other than cesium. One can expect that the isolated regions of metastable states of nonideal plasma are present in a broad range of phase diagrams. This region superposes on and supplements the standard phase diagrams.

REFERENCES

1. É. A. Manykin, M. I. Ozhovan, and P. P. Poluéktov, Dokl. Akad. Nauk SSSR **260**, 1096 (1981) [Sov. Phys. Dokl. **26** (10), 974 (1981)].

2. É. A. Manykin, M. I. Ozhovan, and P. P. Poluéktov, Zh. Éksp. Teor. Fiz. **84**, 442 (1983) [Sov. Phys. JETP **57**, 256 (1983)].

3. É. A. Manykin, M. I. Ozhovan, and P. P. Poluéktov, Zh. Éksp. Teor. Fiz. **105**, 50 (1994) [JETP **78**, 27 (1994)].

4. E. A. Manykin, M. I. Ozhovan, and P. P. Poluektov, J. Mosc. Phys. Soc. **8**, 19 (1998).

5. É. A. Manykin, M. I. Ozhovan, and P. P. Poluéktov, Khim. Fiz. **18** (7), 87 (1999) [Chem. Phys. Rep. **18**, 1353 (2000)].

6. E. A. Manykin, M. I. Ozhovan, and P. P. Poluektov, J. Phys. IV **10**, Pr5-333 (2000).

7. C. Aman, J. B. C. Pettersson, and L. Holmlid, Chem. Phys. **147**, 189 (1990).

8. C. Aman, J. B. C. Pettersson, L. Lindroth, and L. Holmlid, J. Mater. Res. **7**, 100 (1992).

9. L. Holmlid and E. A. Manykin, Zh. Éksp. Teor. Fiz. **111**, 1601 (1997) [JETP **84**, 875 (1997)].

10. N. B. Vargaftik, *Handbook of Thermal Properties of Gases and Liquids* (Nauka, Moscow, 1972).

11. S. Jungst, B. Knuth, and F. Hensel, Phys. Rev. Lett. **55**, 2160 (1985).

12. L. M. Biberman and G. É. Norman, Teplofiz. Vys. Temp. **7**, 822 (1969) [High Temp. **7**, 767 (1969)].

13. G. É. Norman and A. N. Starostin, Teplofiz. Vys. Temp. **8**, 413 (1970) [High Temp. **8**, 381 (1970)].

14. G. É. Norman, Khim. Fiz. **18** (7), 78 (1999) [Chem. Phys. Rep. **18**, 1335 (2000)].

15. G. É. Norman and A. N. Starostin, Teplofiz. Vys. Temp. **6**, 410 (1968) [High Temp. **6**, 394 (1968)].

16. W. Ebeling and W. Richert, Phys. Lett. A **108**, 80 (1985).

17. W.-D. Kraeft, D. Kremp, W. Ebeling, and G. Röpke, *Quantum Statistics of Charged Particle Systems* (Akademie-Verlag, Berlin, 1986; Mir, Moscow, 1988).

18. G. E. Norman, Contrib. Plasma Phys. **41** (2) (2001).

19. R. Svensson and L. Holmlid, Phys. Rev. Lett. **83**, 1739 (1999).

20. L. Holmlid, Phys. Rev. A **63** (6), 013817 (2001).

Translated by V. Sakun

Phase Composition of Ti–C Films Obtained under the Technological Conditions of Diamond Formation at a Carbon Content of Above 50 at. %

V. I. Perekrestov and A. V. Pavlov

Sumy State University, Sumy, 40007 Ukraine

Received August 28, 2000; in final form, November 9, 2000

The phase composition of Ti–C films (with the carbon content varying from 50 to 100 at. %) is studied by electron diffraction. The films are obtained by C and Ti ion sputtering followed by vapor deposition in the regime of the lowest possible supersaturation. It is found that the condensation in a certain proportion of components leads to the formation of a TiC_2 compound, which has the bcc lattice with a period of 0.294 nm. When the carbon content is increased above 64 at. %, a transition to the diamond phase is observed. © *2001 MAIK "Nauka/Interperiodica".*

PACS numbers: 68.55.Nq; 81.15.-z; 61.14.-x

Among the known low-temperature ion technologies used for obtaining diamond and diamondlike carbon films, three directions can be distinguished [1]. The first of them includes the sequential processes of graphite ion sputtering, vapor deposition, and formation of condensates whose structure is then transformed to the diamond phase upon fast heating and cooling by electron beams. In the second direction, the transformation of graphite films to the diamond phase occurs under the action of ion beams in the process of ion sputtering and deposition of carbon. And, finally, the third direction includes the technologies that are based on the synthesis of diamondlike films obtained by the deposition of carbon ions with energies of 80–110 eV on a substrate. It is stressed in [2] that the main general condition for the formation of diamond and diamondlike phases in ion technologies is that the processes occur at high supersaturations, to increase the probability of diamond nucleation. In our opinion, the latter statement is not always true, because the vapor deposition at an infinitely low supersaturation leads to an increase in the contribution of the diffusion processes to the structure formation, while these processes should also stimulate the diamond nucleation. In this paper, we study the process of structure formation in the films of the Ti–C system obtained by vapor condensation in the regime of an infinitely low supersaturation and with the carbon content varying from 50 to 100 at. %.

Experimental technique. It is known [3] that, in contrast to thermal evaporation, ion sputtering provides film deposition at a vapor supersaturation as small as one likes. This fact allows one to obtain infinitely low rates of film growth, and it is used as the basis for our experiment.

At the first stage of the experiment, the films of the Ti–C system were obtained with the help of two magnetron sputterers whose axes were oriented at an angle of 30° to each other and lay in one plane. One of the magnetrons was used for the carbon sputtering, and the other for the titanium sputtering. The orientation of an oblong substrate holder relative to the sputterers made it possible to vary the chemical composition of the condensates from 10 to 80 at. % of carbon. The deposition temperature varied from 60 to 500°C. Thin films were condensed on cleaved KCl facets and then, after the dissolution of the substrate, were studied by electron microdiffraction. To study the microhardness as a function of the chemical composition, we fabricated coatings 10–18 μm thick on oblong glass substrates, which were positioned along the axis of the substrate holder. To determine the behavior of the microhardness as a function of the chemical composition more accurately, we used a diamond indenter to make a scratch along the sample, the width of the scratch being determined by a scanning electron microscope. To determine the microhardness value with higher accuracy, we made, in addition to scratching, a microhardness indentation. Using the ratio between the microhardness values obtained with these two methods, we refined the numerical data on microhardness obtained from scratching.
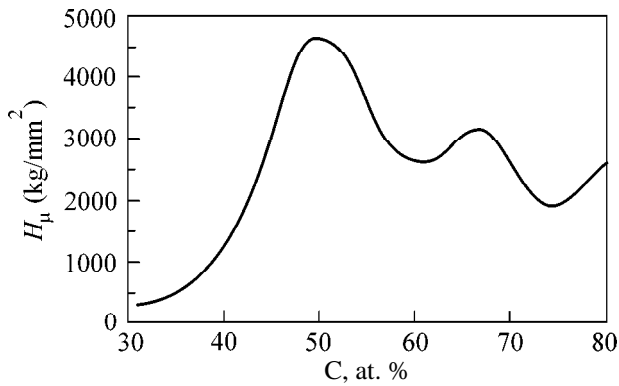
Fig. 1. Microhardness of Ti–C coatings as a function of the carbon concentration.

On the basis of the thickness distribution obtained for the Ti and C coatings deposited in equal time intervals with each of the two sputterers operating separately, we estimated the variations in the component concentrations along the axis of the substrate holder. To obtain the Ti–C coatings for the subsequent studies, we set the sputterers in the operating modes identical to those used in the determination of the chemical composition.

A serious technological problem that is encountered in the deposition of films with the lowest possible growth rates is the interaction of Ti with chemically active residual gases, which competes with the carbide process. Therefore, we paid special attention to the optimization of the vacuum conditions of condensate formation. Argon (used in our experiment as working gas) was subjected to a thorough cleaning, which allowed the partial pressure of chemically active gases to be maintained at a level not exceeding 10^{-6} Pa during the entire technological process. To test the vacuum conditions of film deposition, we studied the phase composition of Ti films deposited with low growth rates [4]. The condensates obtained under these conditions had an α-Ti face-centered close-packed lattice, which, with allowance for the getter properties of Ti, confirmed that the partial pressures of chemically active gases were sufficiently low. At the second stage of our studies, the films were deposited by a single-magnetron sputtering of a composite target consisting of Ti and C.

Results and discussion. In the case of film deposition by the two-magnetron sputtering with condensation temperature $T_{cond} \sim 60°C$ followed by the annealing of the condensates at $T = 430°C$ for 3 h, we observed no deviations from the constitution diagram of the Ti–C system [5]. This fact indirectly confirms the validity of the calculated chemical composition. At higher condensation temperatures, the phase composition of the films remained coincident with the constitution diagram of the Ti–C system up to $T_{cond} \sim 350°C$. At

the same time, with an increase in the carbon content above 55 at. %, the microhardness decreased and the dispersivity of films increased. The electron diffraction studies showed that, when the carbon content in the films exceeded 65 at. %, the period of the fcc lattice of TiC increased to ~4.55 Å. Such a noticeable increase in the lattice period presumably testifies to the formation of interstitial defects upon the deposition of high-energy atoms that are always present in the sputtered vapor flow [3]. We also note that, as the carbon concentration grows and becomes higher than 60 at. %, the intensity of the diffraction lines gradually decreases and the background due to the diffusion scattering of electrons increases. All these facts testify to an increase in the concentration of free carbon.

At $T_{cond} \sim 400°C$, the mechanism of structure formation changes. In the region with a carbon content of about 65 at. %, a considerable growth of microhardness is observed (Fig. 1) and, simultaneously, three relatively intense but broadened lines of the bcc lattice with a period of ~0.3 nm appear in the electron diffraction patterns. The dynamics of the changes occurring in the film phase composition with an increase in the carbon content from 50 to 65 at. % is shown in Figs. 2a–2c.

To verify the fact of the bcc lattice formation, the film growth was also performed by using only one magnetron with a composite target of Ti and C. The necessary geometry of the composite target was calculated by a special technique and provided the vapor flow with the carbon contents of ~66 and 82 at. %. In this case, the film growth rate was reduced by approximately a factor of 60 (to 0.008–0.01 nm/s), and the condensation temperature was $T_{cond} \approx 500°C$. Simultaneously, the partial pressure of chemically active gases was reduced to 8×10^{-8} Pa. Such extreme conditions made it possible to obtain the bcc lattice in the pure state, with a simultaneous considerable decrease in both dispersivity (Fig. 2d) and lattice period (to 0.294 nm). At the carbon content of 82 at. %, the electron diffraction patterns show the lines belonging to the diamond phase (Fig. 2e). In this case, the diffraction peaks corresponding to the (111) and (220) planes of the diamond phase are superimposed on the diffraction peaks of the (110) and (211) planes of the bcc phase. This results in a relative growth of the intensities and a broadening of the corresponding lines in the electron diffraction pattern.

Using one magnetron and a pure carbon target with the technological parameters of the preceding experiment, we obtained films containing a diamond phase (Fig. 2f).

From the experimental results described above, we can draw the following conclusions:

(1) the chemical composition of the bcc phase approximately corresponds to the TiC_2 compound.
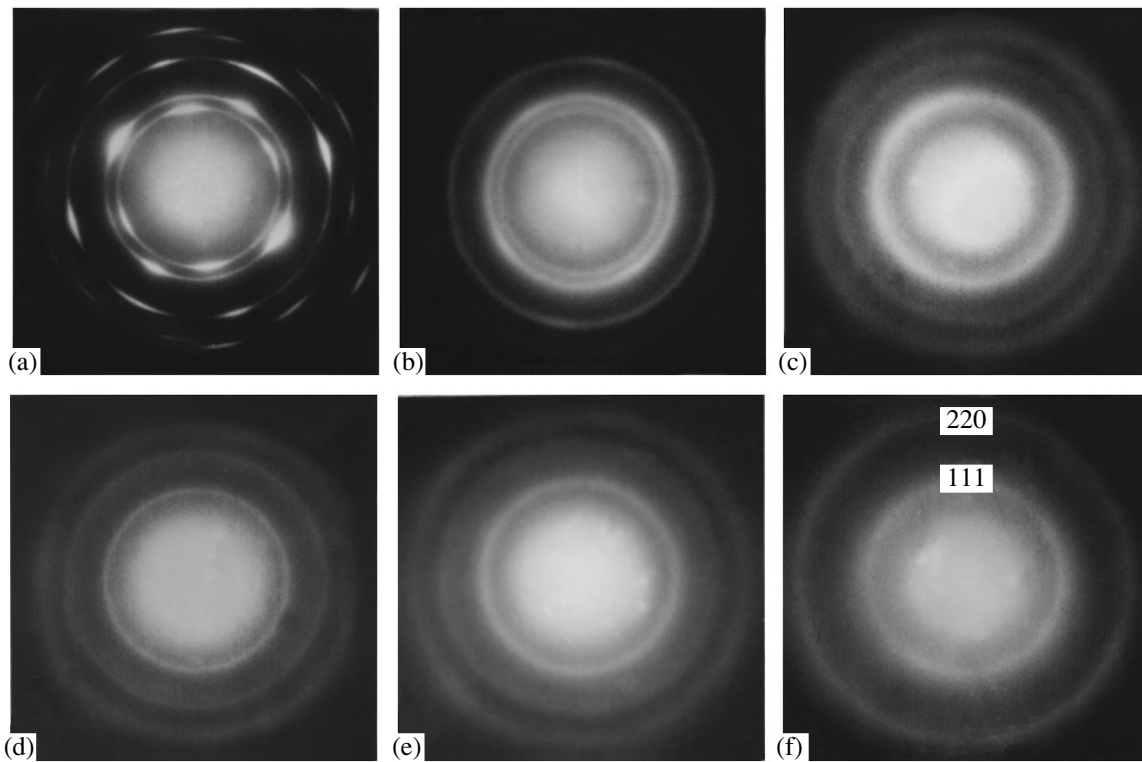
Fig. 2. Phase composition of Ti–C films with different carbon contents: (a) ~50, (b) 58, (c) 65, (d) 66, (e) 82, and (f) 100 at. %.

(2) the formation of the bcc phase is accompanied by an increase in the microhardness.

Using these experimental data, we constructed the TiC$_2$ lattice shown in Fig. 3. In essence, this lattice is a result of the introduction of four carbon atoms into the interstitial positions of the TiC fcc lattice. The transition from TiC$_2$ to the diamond phase with decreasing titanium concentration is presumably caused by the compression of the carbon sublattice to the diamond form.

The crystallographic density of TiC$_2$ is 2350 kg/m^3.

In the case under study, a decrease in T_{cond}, an increase in the film growth rate (i.e., in the supersaturation), and an increase in the partial pressure of chemically active gases lead to an increase in the dispersivity and to the appearance of the graphite phase. Presumably, the presence of atoms with higher energies in the ion-sputtered vapor flow is also the necessary condition for the formation of the diamond phase and TiC$_2$. Possibly, heating of the growth surface by secondary electrons and stability of the technological process are crucial factors as well.

It should be noted that the possibility of the existence of TiC$_2$ was considered earlier. In studying the reaction products of ethylene with titanium tetrachloride at high temperatures [6], it was found that the content of bound carbon in this product was higher than 50 at. %. It was assumed that the resulting carbide had a TiC$_2$ composition and a cubic lattice of the CsCl type with a period of 0.313 nm. However, these results were not confirmed by the subsequent studies [7]. The phase
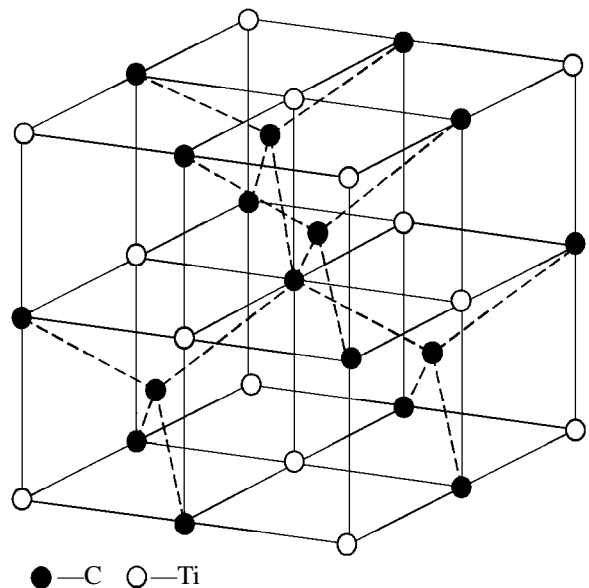
Fig. 3. Structure of the TiC$_2$ lattice.

observed in [6] could presumably be a transition phase between TiC and TiC_2.

Thus, the increase in the contribution of the diffusion process to the formation of a film structure extends the technological possibilities for obtaining the diamond phase and its associates.

REFERENCES

1. A. P. Semenov, I. A. Semenova, N. N. Smirnyagina, *et al.*, in *Proceedings of the IV International Symposium on Diamond Films and Related Materials, Kharkov, 1999.*

2. D. V. Fedoseev, *Diamond in Electronic Technology* (Énergoatomizdat, Moscow, 1990).

3. *Handbook of Thin-Film Technology*, Ed. by L. I. Maissel and R. Glang (McGraw-Hill, New York, 1970; Sov. Radio, Moscow, 1977), Vol. 1.

4. V. I. Perekrestov, S. N. Kravchenko, and A. V. Pavlov, Fiz. Met. Metalloved. **88**, 72 (1999).

5. V. I. Perekrestov, S. N. Kravchenko, and A. V. Pavlov, Vopr. At. Nauki Tekh. **2** (10), 82 (1999).

6. S. Raman and G. Ramachandran, Curr. Sci. A **31**, 321 (1962).

7. G. V. Samsonov, G. Sh. Upadkhaya, and V. S. Neshpor, *Physical Materials Science of Carbides* (Naukova Dumka, Kiev, 1974).

Translated by E. Golyamina

Dynamic Stability of a System of Concentric Circular Domains

V. N. Mal'tsev and N. M. Fakhrutdinov

Ural State University, pr. Lenina 51, Yekaterinburg, 620083 Russia
e-mail: vladimir.maltsev@usu.ru
Received August 22, 2000; in final form, November 21, 2000

The most prominent features of the behavior of domain structures of the "driving center" type were obtained within a simple phenomenological model. It was shown that the external field frequency is a stabilizing factor for such systems. © *2001 MAIK "Nauka/Interperiodica"*.

PACS numbers: 75.60.Ch

An excited state of a multidomain medium, named the Anger state, was found when studying garnet ferrite films with perpendicular anisotropy in an audio-frequency alternating magnetic field [1]. In this state, moving domain walls are self-organized to form diversified stable dynamic domain structures. For example [2, 3], dynamic systems of concentric circular domains arise on some local defects of the sample at certain values of the amplitude and frequency of a field perpendicular to the film surface. These domains propagate from the center with small velocity. Such a dynamic domain structure was named "driving center." Several driving centers may exist simultaneously in a sample, and the most active driving center may contain more than 30 circles. The rate of change in radii of domain walls and their number in a driving center depend on the field amplitude and frequency.

At present, there is no theory that would describe the process of formation and development of driving centers or even the amplitude–frequency domain of existence of the dynamic domain structures of this type. Static properties of systems of concentric circular domains were studied theoretically in [4, 5].

The aim of this work is to explain some features of dynamic domain structures of the driving center type. For this purpose, it is suggested that the existence of driving centers is primarily caused by the dynamic stability of the system of concentric circular domains rather than the features of magnetization reversal processes on a defect. Then, the amplitude–frequency domain of existence of driving centers must be the domain of stability for the systems of concentric circular domains. A defect is merely a source of circular domains whose formation mechanism is an independent problem, whereas the influence of a defect on the stability of the systems of concentric circular domains still remains to be clarified. Thus, to determine the amplitude–frequency domain of existence of driving centers, one should study the stability of systems of concentric circular domains rather than the conditions for magnetization reversal on a defect.

A phenomenological dissipative model was chosen as a basis for calculations. The geometry of the problem is shown in Fig. 1. It was assumed that the thickness of domain walls equals zero, and their effective mass is expressed in terms of the Döring mass. It was also assumed that a moving domain wall experiences a frictional force proportional to the velocity of motion (viscous friction) and a frictional force due to the interaction of the domain wall with inhomogeneities and defects (coercive force). These forces were expressed through a dissipative function of the following form:

$$\Re = \frac{1}{2}\frac{2M}{\mu}\sum_{k=1}^{N}2\pi r_k L\left(\frac{dr_k}{dt}\right)^2 + 2MH_c\sum_{k=1}^{N}2\pi r_k\left|\frac{dr_k}{dt}\right|.$$

Here, the following notation is introduced: M is the magnetization, $\mu = \gamma\Delta_0/\alpha$ is the domain wall mobility, α is the viscous dissipation factor, γ is the gyromagnetic ratio, $\Delta_0 = \sqrt{A/K}$, A is the exchange interaction constant, K is the uniaxial anisotropy constant, H_c is the coercive force, and N is the number of domain walls in the system of concentric circular domains. The first term in this expression is the Rayleigh dissipative function for a system of circular domain walls, and the second term describes the friction associated with the presence of defects and inhomogeneities, also for a system of N circular domain walls.

The equation of motion in a dimensionless form for an arbitrary kth domain wall was obtained from the Lagrange equation with allowance made for energy dissipation. The conversion to dimensionless quantities was carried out by dividing the energies by $(2\pi M)^2 L^3$ and by introducing "dimensionless time" $\tau = \omega_0 t$ and dimensionless variables $R_k = r_k/L$. In this notation, the
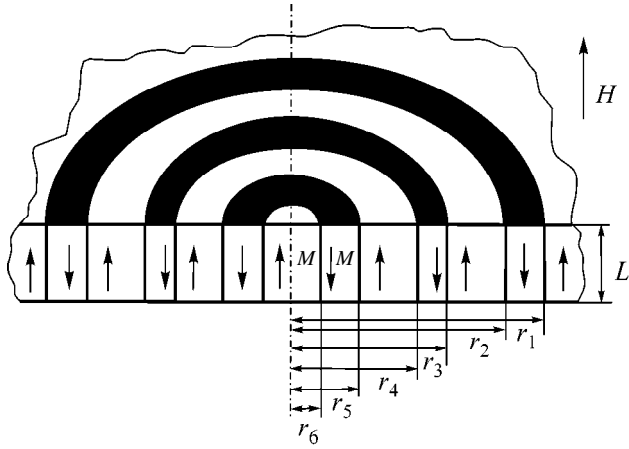
Fig. 1.

dissipative function takes the following form:

$$\Im = \frac{1}{2}\frac{L\omega_0^2}{\pi M \mu}\sum_{k=1}^{N}R_k(\dot{R}_k)^2 + 4h_c\omega_0\sum_{k=1}^{N}R_k|\dot{R}_k|,$$

where ω_0 is the frequency of external field and $h_c = H_c/4\pi M$ is the reduced coercive force. The kinetic energy in the Lagrangian was determined by the equation

$$T = \frac{Lm_D\omega_0^2}{4\pi M^2}\sum_{k=1}^{N}R_k(\dot{R}_k)^2.$$

The total potential energy of an isolated system of concentric circular domains in an infinite film (minus the energy of the film magnetized to saturation) was described by the equation given in [5]:

$$U = 2\tilde{l}\sum_{k=1}^{N}R_k - h(\tau)\sum_{k=1}^{N+1}s_kR_k^2 + \sum_{k=1}^{N+1}s_kR_k^2$$

$$+ \int_{0}^{\infty}\frac{1-e^{-x}}{x}\left[\sum_{k=1}^{N+1}s_kR_kJ_1(R_kx)\right]^2 dx,$$

where $\tilde{l} = l/L = \sigma_0/2\pi M^2 L$ is the reduced characteristic length; σ_0 is the energy density of domain wall

$$s_k = \begin{cases} 2(-1)^k, & k \le N \\ \rho - (-1)^N, & k = N+1; \end{cases}$$

$\rho = M_{def}/M$ is the "magnetic charge" of the defect; J_0 and J_1 are, respectively, the zero-order and first-order Bessel functions of the first kind; and $h(\tau) = H(\tau)/4\pi M$ is the reduced external magnetic field. The first term in the expression for the potential energy is the wall energy, the second term describes the energy of interaction with the external field, and the remaining terms represent the magnetostatic energy of a system of N

concentric circular domain walls with a defect with irreversible magnetization at the center of the system.

The following equation of motion was obtained for the kth domain wall:

$$\beta_1\left(\ddot{R}_k + \frac{1}{2R_k}(\dot{R}_k)^2\right) + \beta_2\dot{R}_k$$

$$+ 2h_c\text{sgn}(\dot{R}_k) + F_k(R_k, \tau) = 0, \tag{1}$$

where

$$\beta_1 = \frac{L}{\Delta_0}(1+\alpha^2)\left(\frac{1}{4\pi\gamma M}\right)^2, \quad \beta_2 = 2\frac{L}{\Delta_0}\left(\frac{1}{4\pi\gamma M}\right),$$

$$F(R_k, \tau) = \frac{\tilde{l}}{R_k}$$

$$+ s_k\left[1 - h(\tau) + \int_{0}^{\infty}\frac{1-e^{-x}}{x}J_0(R_kx)\sum_{n=1}^{N+1}s_nR_nJ_1(R_nx)dx\right].$$

In compliance with the experimental data [1, 2], the following values were used in calculations: $M = 11$ G, $L = 10^{-3}$ cm, $l = 10^{-4}$ cm, and $\Delta_0 = 1.3 \times 10^{-6}$ cm. Assuming that $\gamma \approx 2 \times 10^7$ Oe^{-1} s^{-1} and $\alpha^2 \approx 0$, we find that β_1 is seven orders of magnitude smaller than β_2. Therefore, the terms in Eq. (1) with the coefficient β_1 can be omitted in the first approximation. That is, the inertial effects were not taken into account. The model was further simplified by excluding from consideration both the coercivity of the walls and the defect at the center of the structure. Thus, the equation $\beta_2\dot{R}_k + F_k(R_k, \tau) = 0$ was used for calculations and solved numerically by the fourth-order Runge–Kutta method. The integrals of the form

$$\int_{0}^{\infty}\frac{1-e^{-x}}{x}J_0(ax)J_1(bx)dx$$

were either tabulated beforehand or approximated by the expression

$$\frac{1}{\pi}\left[\tan\left(\frac{(a-b)}{3}\frac{2\pi}{3}\right) + \tan\left(\frac{(2a+b)}{3}\frac{2\pi}{3}\right)\right].$$

The number of domain walls N, the field amplitude h, the field frequency ω_0, the character of field variations (sinusoidal or sawtooth oscillations), and the parameter β_2 were varied in calculations.

The dynamics of a system of concentric circular domains with $N = 2$, that is, a single circular domain, was initially studied. The calculation shows that, at small β_2 ($\ll 0.01$), the walls move synchronously in unipolar sinusoidal and sawtooth fields, the width of the circular domain remains unchanged, and the circle rapidly shrinks and collapses. At large β (≈ 0.01), the domain walls move nonsynchronously. As the field increases, the radius at the inner wall decreases, and the
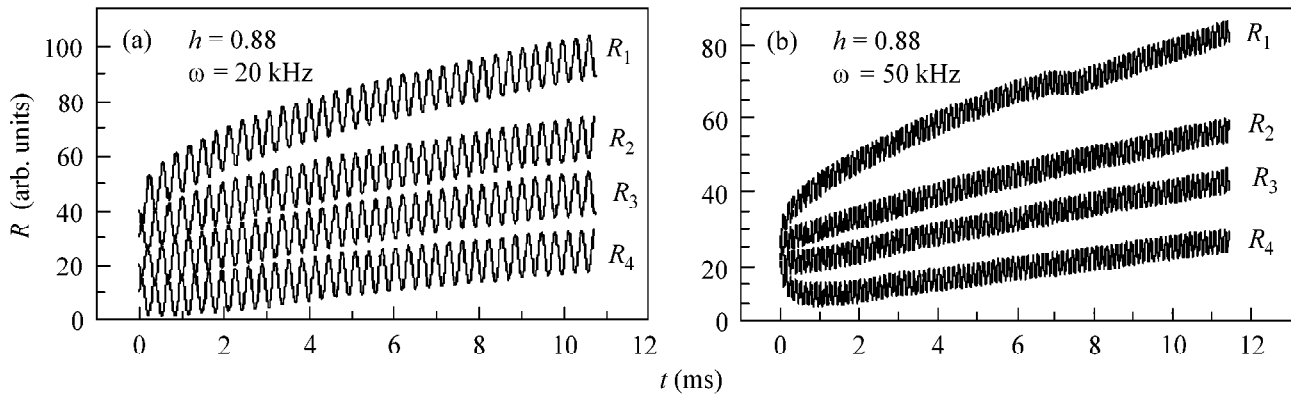
Fig. 2. Time dependence of the reduced radii of domain walls (R) in a system of four driving center (field amplitude $h = 0.88$): $\omega =$ (a) 20 and (b) 50 kHz.

radius at the outer wall remains unchanged. Conversely, as the field decreases, the radius at the inner wall remains unchanged, and the radius at the outer wall decreases. Previously, the same behavior of a circular domain was observed in orthoferrite plates placed in a unipolar alternating magnetic field [6, 7]. The dynamics of an isolated circular domain was also considered with inclusion of inertial effects; however, no qualitative difference was found, giving additional evidence in favor of the approximation chosen.

The behavior of a system of concentric circular domains in an alternating sinusoidal field (without magnetic biasing) was studied for various numbers of domain walls in the system. No significant qualitative difference was found in the behavior of a circular domain and a system with a large number of walls. The following stability test was used: if the radii of the neighboring domain walls are not equal and do not vanish at the initial stage of their existence, the system is assumed stable. It was found that an increase in frequency at a constant field amplitude may enhance the stability of systems of concentric circular domains. The variation of their radii with time is shown in Fig. 2 for a system of four domain walls. The field amplitudes in Figs. 2a and 2b are equal; however, the field frequency is 20 kHz in Fig. 2a and 50 kHz in Fig. 2b. Figure 2a demonstrates that the radius of the inner wall becomes equal to zero at a certain instant of time. According to the test chosen, this points to the instability of the system at this frequency. The radius of the inner wall becomes different from zero only after the outer walls have moved outward to a certain distance. The radii of all walls in Fig. 2b are different from zero; that is, an increase in the field frequency enhanced the stability of this system of concentric circular domains. A comparison of Figs. 2a and 2b indicates that the amplitude of domain wall oscillations decreases as the frequency of the external field increases. The outer size and, hence, its growth rate also decrease. A calculation shows that the system loses stability above a certain field amplitude. However, an increase in frequency restores the

system to a stable state. The dependence of stability on the field amplitude and frequency found here can be explained as follows: the increase in frequency leads to a decrease in the amplitude of wall oscillations; hence, the average distance between walls becomes larger in one period of field oscillation; that is, the walls have no time to collapse. Conversely, an increase in the field amplitude increases the amplitude of domain wall oscillations, resulting in their collapse; that is, the system loses stability.

The calculated curves for the upper bound (with respect to the field amplitude) of domain of stability are presented in Fig. 3 as functions of frequency for systems with various numbers of domain walls. This figure demonstrates that the system with $N = 2$ is unstable at a frequency of 20 kHz if the reduced field amplitude is $h = 0.54$, but it will be stable at this amplitude if the frequency is increased up to 25 kHz. A similar behavior is observed experimentally in [1, 2].

Figure 3 also demonstrates that, at a fixed frequency, the field oscillation amplitude at which the system still remains stable decreases with increasing number of domain walls. Consequently, the number of domain
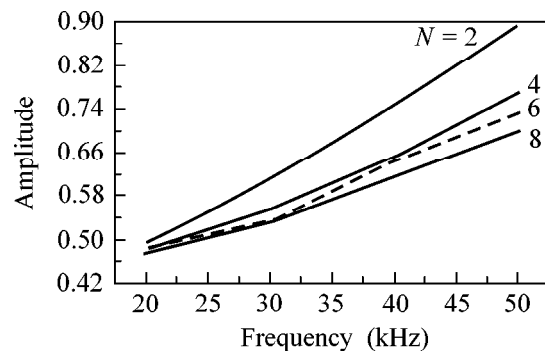
Fig. 3. Upper bounds of the amplitude–frequency domain of existence of a system of concentric circular domains containing two, four, six, and eight domain walls.

walls in a system of concentric circular domains will decrease if the field amplitude is increased at a constant field frequency. This decrease in the number of domain walls in a driving center upon an increase in the field amplitude is also observed experimentally [3].

According to Fig. 3, the system becomes unstable as the field amplitude reaches a certain value (at a fixed frequency); that is, the radius of the inner wall becomes different from zero only a certain time after switching on the field, as is shown in Fig. 2a. This means that the new wall forms in a longer time than at smaller amplitudes. A decrease in the frequency of driving center "operation" (the frequency of the formation of new walls) with increasing pumping field amplitude was also observed experimentally [2]. The results displayed in Figs. 2 and 3 were obtained for $\beta_2 = 10^{-6}$. This value corresponds to the garnet ferrite films used experimentally. A calculation shows that an increase in β_2 enhances the stability of the system. Thus, for example, the system at a fixed frequency will be stable at large amplitudes in films with large β_2.

A number of the most prominent features of the behavior of a driving center can be explained using the frequency dependence of the upper bound (for the field amplitude) of the stability domain of a system of concentric circular domains, calculated for various N. This demonstrates the effectiveness of the approach chosen and leads to the conclusion that the amplitude–frequency domain of existence of a driving center is the domain of its dynamic stability. It should especially be noted that the pumping field frequency is a stabilizing factor for a system of dynamic concentric circular domains.

REFERENCES

1. G. S. Kandaurova and A. É. Sviderskiǐ, Zh. Éksp. Teor. Fiz. **97**, 1218 (1990) [Sov. Phys. JETP **70**, 684 (1990)].
2. G. S. Kandaurova, Dokl. Akad. Nauk **331**, 428 (1993) [Phys. Dokl. **38**, 342 (1993)].
3. G. S. Kandaurova, Fiz. Met. Metalloved. **79**, 158 (1995).
4. A. F. Gal'tsev and Yu. I. Yalyshev, Fiz. Met. Metalloved. **85**, 5 (1998).
5. V. N. Mal'tsev and N. M. Fakhrutdinov, Fiz. Met. Metalloved. **88**, 17 (1999).
6. A. V. Antonov, A. M. Balbashov, *et al.*, Fiz. Tverd. Tela (Leningrad) **14**, 1901 (1972) [Sov. Phys. Solid State **14**, 1649 (1973)].
7. F. A. de Jonge, W. F. Druyvesteyn, and A. G. H. Verhulst, J. Appl. Phys. **42**, 1270 (1971).

Translated by A. Bagatur'yants

Structure of the Intersubband Collective Excitations in Quasi-Two-Dimensional Systems in a Magnetic Field

V. E. Bisti

Institute of Solid-State Physics, Russian Academy of Sciences, Chernogolovka, Moscow region, 142432 Russia

Received November 23, 2000

The spectrum of intersubband collective spin- and charge-density excitations is calculated for a system of quasi-two-dimensional electrons with $\nu \leq 10$ (ν is the filling factor) in a magnetic field. The transitions both without changing the Landau level and with its change (Bernstein modes) are considered. All excitations are shown to have a multimode structure, the number of modes being determined by the filling factor. The dispersion and interaction of small-quasimomentum collective excitations are also considered. The possibility of observing the multimode structure is predicted. © *2001 MAIK "Nauka/Interperiodica".*

PACS numbers: 73.20.Mf

Quasi-two-dimensional electron systems have been an object of investigation over the last several decades. Of particular interest are the collective excitations specific to these systems and caused by the presence of several size-quantization subbands. Charge-density excitations (CDEs) and spin-density excitations (SDEs) are the main collective excitations associated with the intersubband transitions. They were rather thoroughly studied, both theoretically and experimentally, in the absence of a magnetic field [1–8]. The theoretical methods of their description include the random phase approximation (RPA) [1, 2], the local density approximation (LDA) [3, 4], and the direct variational methods [5–7].

For the quasi-two-dimensional systems in a magnetic field, both the fundamental excitations without changing the Landau level (CDEs and SDEs) and the combined intersubband-cyclotron Bernstein modes (ISBMs) were considered [9–14]. The theoretical approach to this problem within the framework of RPA and LDA [9, 10] does not explain all the experimental results obtained in recent years by the Raman scattering technique [12–14]. For instance, the study of the CDEs and SDEs in strong magnetic fields [14] has revealed a new nonpolarized line that appears at $\nu = 2$ near the SDE line and persists at $\nu \geq 2$.

In my previous work [15], the spectrum of intersubband collective excitations was calculated for $\nu \leq 4$ in the strong field limit by the direct method in the Hartree–Fock approximation. It was shown that two closely spaced lines appear at $\nu = 2$, in accordance with the results obtained in [14].

In this work, the method suggested for calculating the collective excitations in strong magnetic fields is applied to the spectra of intersubband excitations of various types over a wide range of magnetic fields for different quasimomenta. The spectra of intersubband excitations are calculated for small **k** values, $\nu \leq 10$, and $\Delta n = 0, \pm 1$, and ± 2 (Δn is a change in the Landau level number). It is shown that both the Bernstein modes (excitations with $\Delta n \neq 0$) and the $\Delta n = 0$ excitations have a multimode structure; the new modes appear upon filling the new Landau level. Quasimomentum dependence is considered for the new modes, and comparative intensities are estimated for the Raman scattering from various modes.

The spectrum of intersubband collective excitations is calculated as a function of magnetic field H under the following conditions:

(1) The system contains two size-quantization subbands, and the influence of the remaining subbands is ignored. The density n_s of two-dimensional electrons is such that the lower subband E_0 is filled, while the next E_1 is empty. The energies E_0 and E_1 are calculated in the Hartree approximation, and $E_{10} = E_1 - E_0$.

(2) Magnetic field H is applied perpendicularly to the two-dimensional layer. The range of magnetic fields corresponds to $\nu \leq 10$.

(3) Only the processes without spin flip are considered; for simplicity, the electron g factor is assumed to be zero ($\mu_0 g \ll T$, where T is temperature), but spin degeneracy is taken into account.

(4) The long-wavelength limit $ka \ll 1$ and $ka_H \ll 1$ [a is the width of quantum well, and $a_H = (\hbar c/eH)^{1/2}$ is the magnetic length] is considered.

(5) Energy scales are such that $\delta E \ll T \ll \Delta E$ (ΔE is the characteristic spacing between the levels in the system, and δE is the impurity-induced width of the Landau levels).

The energies of collective excitations are determined by the poles of the total polarization operator $\Pi(\mathbf{k}, \omega)$. Since the intersubband and intrasubband excitations can be considered independently in the long-wavelength limit, let us consider the intersubband polarization operator

$$\Pi_{01}(\mathbf{k}, \omega) = \sum_{n, n', \sigma} \Pi_{0n, 1n', \sigma}(\mathbf{k}, \omega)$$

$$= \sum_{n, n', \sigma} \sum_{m, m', \sigma'} \Pi_{0n, 1n', \sigma}^{0m, 1m', \sigma'}(\mathbf{k}, \omega), \tag{1}$$

where m, m', n, and n' number the Landau levels.

For an integer filling factor, all energy-degenerate Landau levels are filled with the probability equal to unity. It will also be assumed that the filling of Landau levels is equally probable for an arbitrary filling factor, because the level widths are small compared to the temperature; otherwise, the zero-temperature Green's function technique will be used [condition (5) is fulfilled]. A comparison of the E_{CD} value calculated in the RPA approximation by this method with the result obtained in [10] by using the finite-temperature technique shows that both values are equivalent under the above-mentioned assumptions.

The set of equations for $\Pi_{0n, 1n', \sigma}$ includes the summation over the ladder and loop diagrams describing, respectively, the excitonic and depolarization effects. The one-particle Green's function takes into account the exchange corrections to the self-energy part. This set of diagrams corresponds to the Hartree–Fock approximation. It was taken into account in [5–7], where the intersubband collective excitations were calculated in the absence of a magnetic field; in [16, 17], devoted to magnetoplasmon-type excitations in purely two-dimensional systems; and, in part, in [18], where the Mott exciton in quasi-two-dimensional semiconductors was considered in a strong magnetic field. In this approximation, the one-particle Green's function in a magnetic field depends only on frequency, while the interaction depends only on momenta. Because of this, the interaction can be averaged over the momenta, whereupon the set of equations becomes algebraic. The interaction responsible for the depolarization shift has the form

$$\alpha_{0n, 1n', \sigma}^{0m, 1m', \sigma'}(k) = V_{01}^{01}(k) I_{nn'}(k, 0) I_{m'm}^*(k, 0) = \alpha_{nn'}^{mm'}(k). \tag{2}$$

The interaction responsible for the excitonic corrections is

$$\beta_{0n, 1n', \sigma}^{0m, 1m', \sigma'}(k) = -\delta_{\sigma\sigma'}(2\pi)^{-1}$$
$$\times \int V_{00}^{11}(q) J_{nm}(\mathbf{q}) J_{n'm'}^*(\mathbf{q}) e^{i a_H^2 q_y k} d\mathbf{q} = \delta_{\sigma\sigma'} \beta_{nn'}^{mm'}(k), \tag{3}$$

where

$$V_{ik}^{jl}(q) = \frac{2\pi e^2}{\varepsilon q} \int \exp(-q|z_1 - z_2|) \psi_i(z_1) \psi_k(z_1)$$
$$\times \psi_j(z_2) \psi_l(z_2) dz_1 dz_2; \tag{4}$$

$$I_{nn'}(q_x, q_y) = \int \phi_n(y) \phi_{n'}(y + q_x a_H^2) \exp(-i q_y y) dy; \tag{5}$$

i, j, k, and l label the subbands; $\psi_i(z)$ are the electronic wave functions in the direction of quantization axis; and $\phi_n(y) = \pi^{-1/4} (a_H 2^n n!)^{-1/2} \exp(-y^2 / 2 a_H^2) H_n(y/a_H)$. The x axis is directed along $\mathbf{k}$.

At $\mathbf{k} = 0$, the transitions with different $\Delta n = n' - n$ can be considered independently from each other. At small $\mathbf{k}$ values [condition (4)], the interaction of levels manifests itself only near the crossing points. For this reason, one can consider the restricted number of transitions for a given energy range; in this work, these are the transitions with $|\Delta n| \leq 2$, which were experimentally observed in [11, 13]. The set of equations for $\Pi_{0n, 1n', \sigma}$ then becomes finite:

$$\Pi_{0n, 1n', \sigma} = \Pi_{0n, 1n', \sigma}^0 + \Pi_{0n, 1n', \sigma}^0 V_{0n, 1n', \sigma}^{0m, 1m', \sigma'} \Pi_{0m, 1m', \sigma'},$$
$$V_{0n, 1n', \sigma}^{0m, 1m', \sigma'} = \alpha_{nn'}^{mm'} + \beta_{nn'}^{mm'} \delta_{\sigma\sigma'}. \tag{6}$$

The zeroth polarization operators including the exchange corrections are

$$\Pi_{0n, 1n', \sigma}^0 = \frac{n_{n\sigma}}{\omega - E_{10} - \Sigma_{1n'\sigma} + \Sigma_{0n\sigma} - \hbar\omega_c(n' - n)}. \tag{7}$$

The exchange corrections to the one-particle energies are

$$\Sigma_{in\sigma} = \sum_m \varepsilon_{nm}^{0i} n_{m\sigma}; \tag{8}$$

$$\varepsilon_{nm}^{0i} = -(2\pi)^{-1} \int V_{0i}^{0i}(q) |I_{nm}(\mathbf{q})|^2 d\mathbf{q}; \quad i = 0, 1,$$

where $n_{n\sigma}$ is the electron density at the $(0, n, \sigma)$ level and $\omega_c = eH/mc$ is the cyclotron frequency.

The poles are found by setting the determinant of Eq. (6) equal to zero,

$$\det \left| \Pi_{0n, 1n', \sigma}^0 V_{0n, 1n', \sigma}^{0m, 1m', \sigma'} - \delta_{nn'\sigma, mm'\sigma'} \right| = 0. \tag{9}$$

Introducing finite damping, one can solve the inhomogeneous set of Eqs. (6) to estimate the relative line intensities for the Raman scattering from the calculated excitations. The number of modes is

$$N_i(\Delta n \geq 0) = [\nu/2] + 1;$$
$$N_i(\Delta n < 0) = [\nu/2] + 1 + \Delta n, \tag{10}$$

where $i = cd$ and sd; no modes exist at negative N values. Note that the modes are separated into the CD and SD types, so that their spectra are determined independently only if the system is spin-nonpolarized ($n_{n, 1/2} =$
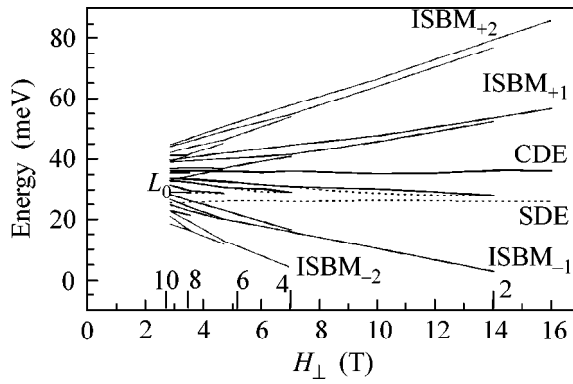
Fig. 1. Energies of intersubband collective excitations in the system of two-dimensional electrons confined in a single quantum well of width 250 Å ($n_s = 6.8 \times 10^{11}$ cm^{-2}) vs. perpendicular magnetic field at $k = 0$. The integer filling factors are marked above the abscissa axis.
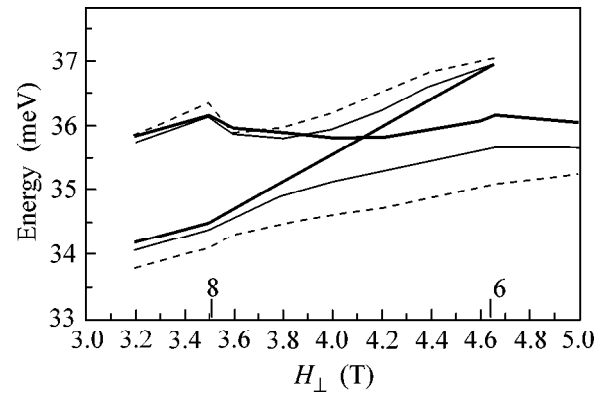
Fig. 2. Energies of intersubband collective excitations vs. magnetic field corresponding to the crossing between the CD and ISBM$_{+1}$ lines for different quasimomenta; $k =$ (solid thick lines) 0, (solid thin lines) 0.4×10^5, and (dotted lines) 0.8×10^5 cm^{-1}.

$n_{n, -1/2}$); however, the number of modes always increases with an increase in the filling factor.

Figure 1 demonstrates the spectra of collective excitations in a rectangular quantum well GaAs/AlGaAs ($a = 250$ Å and $n_s = 6.8 \times 10^{11}$ cm^{-2}) for $k = 0$ and magnetic fields corresponding to $\nu \le 10$. The Bernstein modes are degenerate at $k = 0$ (the ISBM^{cd} and ISBM^{sd} energies coincide). The energies of fundamental CDE and SDE modes as functions of magnetic field weakly oscillate and coincide at integer filling factors. New modes obtained in [15] (CDE1, SDE1, CDE2, SDE2, etc.) are nondegenerate. Their energies have nonzero slopes to the H axis. This multiplet corresponds to the L_0 line that was experimentally observed in [11, 14] and interpreted in [11] as being due to the single-particle excitations.

The quasimomentum dependence of collective excitations calculated for $k \le 1.5 \times 10^5$ cm^{-2} under the same conditions is significant only for the CDE mode in the region of its crossing with the lowest of ISBM$^{cd}_{+1}$ (the degeneracy of ISBM^{cd} and ISBM^{sd} is then removed). The remaining Bernstein modes and the L_0 and SDE modes are virtually dispersionless. Figure 2 illustrates the effect of quasimomentum on the spectrum. One can see that the splitting between the fundamental CD mode and the ISBM$^{cd}_{+1}$ mode is proportional to k. The linear dependence on k is also demonstrated by the CDE energy at $\nu < \nu_c$ (ν_c corresponds to the level crossing). The calculated dependence is consistent with the experimental data and the LDA calculations [13].

The estimation of the Raman intensities from the collective excitations shows that the greatest contribution comes from CDE, SDE, and L_0. The Bernstein modes are much weaker and depend on k. The L_0 multiplet is dominated by the lowest pair of CD and SD lines. However, as new line pairs appear near even integer ν values, the intensities become comparable and the conditions for the observation of a doublet structure are most favorable. The intensity of the lowest line in each group ISBM$_{\Delta n}$ of Bernstein modes is also the highest, and, as for L_0, the doublet structure can be observed as the new modes appear.

In summary, the structure of the intersubband collective excitations in a magnetic field is obtained, its dependence on the momentum is studied, and the contributions of different excitations to the Raman intensities are estimated. The calculations were carried out under the assumption that the energy-degenerate levels are occupied with equal probability at low, though finite, temperature. The results obtained allow the whole spectrum of the experimentally observed collective excitations to be interpreted within the framework of a unified scheme. Finally, the possibility of observing the multimode structure is predicted.

REFERENCES

1. J. K. Jain and S. Das Sarma, Phys. Rev. B **36**, 5949 (1987).
2. D. H. Ehlers, Phys. Rev. B **38**, 9706 (1988).
3. I. K. Marmorkos and S. Das Sarma, Phys. Rev. B **48**, 1544 (1993).
4. A. Pinczuk, S. Smitt-Rink, G. Danan, *et al.*, Phys. Rev. Lett. **63**, 1633 (1989).
5. S. L. Chuang, M. S. C. Luo, S. Schmitt-Rink, *et al.*, Phys. Rev. B **46**, 1897 (1992).
6. M. S.-C. Luo, S. L. Chuang, S. Schmitt-Rink, *et al.*, Phys. Rev. B **48**, 11086 (1993).

7. J. C. Ryan, Phys. Rev. B **43**, 12406 (1991).

8. D. Gammon, B. V. Shanabrook, J. C. Ryan, *et al.*, Phys. Rev. Lett. **68**, 1884 (1992).

9. A. Tselis and J. J. Quinn, Phys. Rev. B **29**, 3318 (1984).

10. L. Wendler and R. Pechstedt, J. Phys: Condens. Matter **2**, 8881 (1990).

11. G. Brosak, B. V. Shanabrook, D. Gammon, *et al.*, Phys. Rev. B **47**, 9981 (1993).

12. V. E. Kirpichev, I. V. Kukushkin, K. von Klitzing, *et al.*, Pis'ma Zh. Éksp. Teor. Fiz. **67**, 196 (1998) [JETP Lett. **67**, 210 (1998)].

13. V. E. Kirpichev, L. V. Kulik, I. V. Kukushkin, *et al.*, Phys. Rev. B **59**, 12751 (1999).

14. I. V. Kukushkin, L. V. Kulik, V. E. Kirpichev, *et al.*, Phys. Rev. B **61**, 12717 (2000).

15. V. E. Bisti, Pis'ma Zh. Éksp. Teor. Fiz. **69**, 543 (1999) [JETP Lett. **69**, 584 (1999)].

16. Yu. A. Bychkov, S. V. Iordanskiĭ, and G. M. Éliashberg, Pis'ma Zh. Éksp. Teor. Fiz. **33**, 152 (1981) [JETP Lett. **33**, 143 (1981)].

17. C. Kallin and B. I. Halperin, Phys. Rev. B **30**, 5655 (1984).

18. I. V. Lerner and Yu. E. Lozovik, Zh. Éksp. Teor. Fiz. **78**, 1167 (1980) [Sov. Phys. JETP **51**, 588 (1980)].

Translated by V. Sakun

Transition to 1D Conduction with Decreasing Thickness of the Crystals of TaS$_3$ and NbSe$_3$ Quasi-1D Conductors

S. V. Zaĭtsev-Zotov*, V. Ya. Pokrovskiĭ*, and P. Monceau**

* Institute of Radio Engineering and Electronics, Russian Academy of Sciences, Moscow, 103907 Russia
** Centre de Recherches sur Les Très Basses Températures, C.N.R.S. 38042 Grenoble Cédex 9, France
Received October 20, 2000; in final form, November 23, 2000

It is found that, with decreasing thickness of the crystals of TaS$_3$ and NbSe$_3$ quasi-1D conductors, the dependences of the conductivity of these crystals on temperature and electric field change from the form typical of bulk samples to a nearly power law behavior typical of 1D electron systems. © *2001 MAIK "Nauka/Interperiodica".*

PACS numbers: 71.10.Pm; 71.30.+h; 71.45.Lr; 72.15.Nj

The behavior of 1D electron systems essentially depends on the effects of Coulomb interaction and electron correlations. For example, in the absence of long-range interaction in 1D metallic systems, one should expect, instead of the electron Fermi liquid, the formation of a Luttinger liquid [1] characterized by a power-law decrease in the tunneling density of states near the chemical potential [2, 3], and, at small concentrations of charge carriers, one can expect the formation of a one-dimensional Wigner crystal [4]. As a result, the behavior of the conductivity of such systems must noticeably differ from the behavior typical of 3D metals. Specifically, one should expect for such 1D systems the power law $G \propto T^{\alpha}$ [2, 3] or the close exponential law $G \propto \exp[-v(\ln T_0/T)^{1/3}]$ [5, 6] for the temperature dependence of conductivity; one should also expect the appearance of nonlinear current–voltage characteristics $I \propto V^{\beta}$ [2, 3].

Currently, active search for objects in which the effects of one-dimensionality can be realized is in progress. In recent years, different methods were developed for fabricating various types of systems in which the manifestations of 1D properties should be expected. For example, chains of metals on the vicinal faces of platinum, palladium, silicon, and other crystals were obtained (see, e.g., [7] and references therein); Si, Ge, and GaAs semiconductor whiskers of diameter less than 10 nm were grown [8, 9]; and Bi nanowires with a diameter of down to 7 nm in an Al$_2$O$_3$ matrix were fabricated [10]. However, the expected 1D behavior of conductivity was observed in none of these objects. The predicted power-law decrease in the tunneling density of states was observed for the edge currents in the quantum Hall effect regime with filling factor $\nu = 1/3$ [11, 12] (Luttinger chiral liquid) and in carbon nanotubes [13, 14]; in the latter, a change in the tunneling conductivity was relatively weak (eightfold). Recently, the power-law dependences of conductivity on temperature and electric field, characteristic of 1D systems,

were observed in InSb quantum nanowires embedded in an asbestos matrix. Although the conductivity range observed for these objects with changing temperature and electric field, was greater than five orders of magnitude, further studies were hampered because of the uncertainty in the doping level and other important parameters of InSb filling the asbestor matrix.

The quasi-1D conductors are promising objects for revealing 1D properties, because they initially (even 3D samples) exhibit effects associated with a reduced dimensionality. One of recent publications describes measurement of the tunneling conductivity of a molecular wire consisting of a Mo$_6$Se$_6$ quasi-1D conductor mounted on gold and pyrolitic graphite surfaces [16]. However, even at $T = 4.2$ K, only a weak decrease in the tunneling density of states near the Fermi level was observed in this experiment; i.e., the electron spectrum retained its metallic character. Below, we report the observation of 1D properties of thin crystals of TaS$_3$ and NbSe$_3$ quasi-1D conductors mounted on an insulator substrate.

Samples of TaS$_3$ and NbSe$_3$ crystals were studied. At room temperature, these materials have a metallic conductivity, judging from the magnitude ($2–5 \times 10^3$ Ω^{-1} cm^{-1}) and the sign of the dG/dT derivative. As the temperature decreases, these materials exhibit a Peierls transition with the formation of a 3D-ordered charge density wave (CDW) [17, 18]. In TaS$_3$, the Peierls transition temperature T_P is 220 K, and, at lower temperatures $T < 220$ K, the conductivity exhibits a semiconductor behavior with an activation energy of about 800 K. In NbSe$_3$, two Peierls transitions occur, with the electron spectrum becoming partially of the insulator type; the transitions occur at temperatures $T_{P1} = 145$ K and $T_{P2} = 59$ K. In this case, those electrons not condensed into the CDW cause metallic behavior of conductivity down to the lowest temperatures. Thin samples of TaS$_3$ and NbSe$_3$ were obtained by splitting them from the bulk samples and placed on a sapphire substrate. The leads
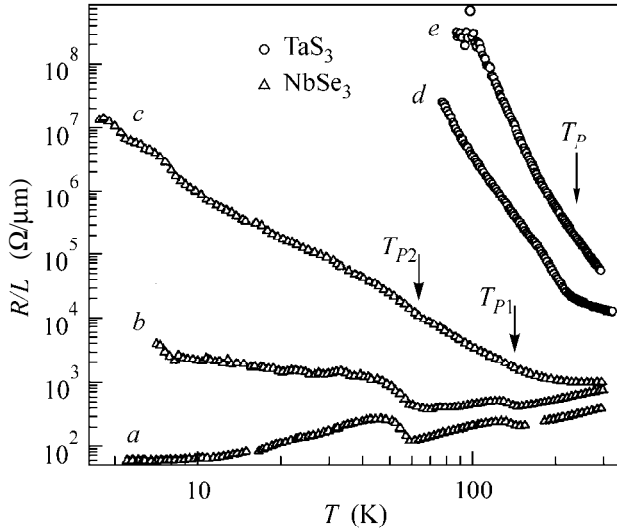
Fig. 1. Temperature dependences of the resistance of the thin TaS_3 and $NbSe_3$ samples. The arrows indicate the positions of the Peierls transitions in usual bulk samples. Curves *b* and *c* correspond to different stages of etching of the $NbSe_3$ sample (curve *a*) in SF_6 plasma. The TaS_3 samples (curves *d* and *e*) are obtained by splitting from bulk samples.

were connected to the samples by cold indium soldering or vacuum deposition of indium. The conductivity was measured by the two-terminal technique. An additional decrease in the thickness of the $NbSe_3$ samples was achieved by SF_6 plasma etching.

Figure 1 presents a set of temperature dependences of the linear resistance of the $NbSe_3$ sample before etching (curve *a*) and after etching for 7 and 9 s (curves *b* and *c*, respectively) at a rate of 3 Å/s; the figure also shows the typical temperature dependences of the linear resistance of two thin TaS_3 samples, one of which retains the traces of the Peierls transition (curve *d*) and the other has lost such traces (curve *e*).[1] One can see that, as the transverse dimensions of the $NbSe_3$ samples decrease (i.e., as their resistance per unit length increases), a gradual transition from metallic behavior of conductivity ($dR/dT > 0$) to nonmetallic behavior ($dR/dT < 0$) is observed first at low temperatures (curve *b*) and, then, at $T < 250$ K (curve *c*). Behavior similar to that of curve *b* was recorded for $NbSe_3$ samples split from the bulk crystal and characterized by $R(300 \text{ K})/L = 0.6$ and 2 kΩ/μm; for the sample with $R(300 \text{ K})/L \sim 10$ kΩ/μm, insulator-type behavior of conductivity, similar to that of curve *c*, was observed.

For the TaS_3 samples with the cross-sectional area $\gtrsim 0.1$ μm^2 ($R/L \lesssim 3$ Ω/μm), $dR/dT > 0$ at room temperature [17–20]. As the transverse dimensions of the samples decrease, the sign of the dR/dT derivative changes

---

[1] The cross-sectional area of the samples with $R(300 \text{ K})/L = 10^3$–$10^4$ Ω/μm can be roughly estimated as 10^3 nm^2, on the basis of the value of the bulk conductivity.

and the Peierls transition is smeared out (see also [19, 21]), as is seen from curve *d*. A further decrease in the transverse dimensions leads to a total disappearance of the traces of Peierls transition (curve *e*).

The current–voltage characteristics of thin samples are nonlinear, and their nonlinearity increases with decreasing temperature. Figure 2 shows a typical set of dependences of the conductivity $L/R \equiv LI/V$ on the electric field $E \equiv V/L$ for the $NbSe_3$ sample etched during a period of 9 s (this corresponds to curve *c* in Fig. 1). One can see that the nonlinearity is distinctly observed at temperatures below 100 K, and, at the lowest temperature, the resistivity changes by more than three orders of magnitude.

To analyze the results, we first consider the temperature dependence of the conductivity. We note the following qualitative changes in conductivity behavior with decreasing sample thickness: the tendency toward insulator behavior (in TaS_3 at room temperature and in $NbSe_3$ at $T > T_{P1} = 145$ K) and the total disappearance of Peierls transitions. It should be emphasized that the disappearance of metallic conductivity at $T > T_P$ in $NbSe_3$ occurs not only when the sample thickness is reduced by etching, but also when thin samples are split from the bulk crystal. This allows one to conclude that the observed tendency toward insulator properties is caused by the smallness of transverse dimensions of the crystals rather than by the changes in the sample composition due to chemical reactions accompanying the etching process.

A decrease in the transverse dimensions of the sample to sizes smaller than the CDW phase correlation length (~1 μm) leads to a decrease in the CDW correlation volume and a decrease in the pinning energy per correlation volume, thereby promoting the phase slip process. All these effects give rise to the growth of the fluctuation conductivity at $T < T_P$ and to the spreading of the threshold field corresponding to the appearance of a nonlinear conduction [21–23]. These effects were studied in detail on samples with much greater transverse dimensions than those used in our experiment. As for the behavior of the conductivity of quasi-1D conductors at $T > T_P$ with decreased dimensions, it is poorly understood. The data reported in the literature testify that, when the cross-sectional area of the TaS_3 [19] and $NbSe_3$ [22, 23] samples decreases, the fluctuative spreading of the Peierls transition causes a slight increase in their resistance at $T > T_P$, including temperatures much higher than T_P. This experimental fact was not considered earlier, although it deserves attention. In principle, one should not rule out the possibility that a decrease in the stiffness of the crystal lattice near the surface contributes to the formation of the CDW, thus leading to an increase in the order parameter of the CDW near the surface of the quasi-1D conductor. In this case, one can expect that a decrease in the sample dimensions is accompanied by an increase in the effective value of the order parameter, i.e., by the appearance of additional insulator features in the electron spec-
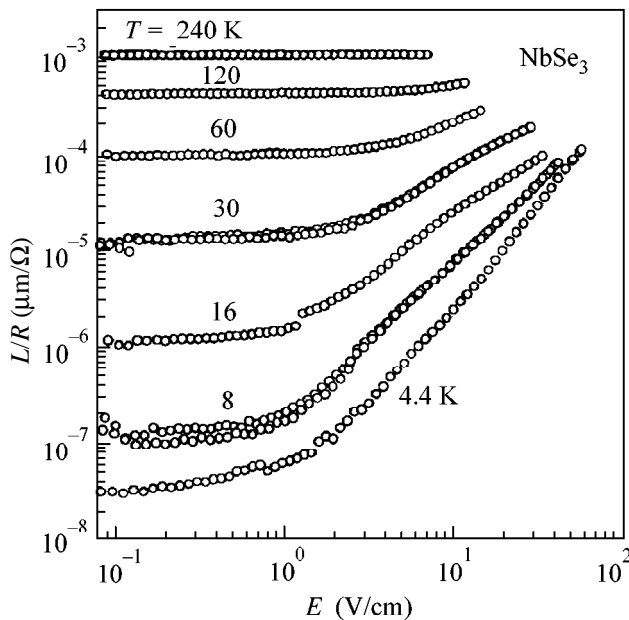
Fig. 2. Conductivity of a thin NbSe$_3$ sample (curve c in Fig. 1) versus electric field at different temperatures.

trum, as compared to the bulk sample. The enhancement of the surface effects can also be responsible for the coherent depinning of the CDW fluctuations, as was observed recently [20] in thin TaS$_3$ samples (R(300 K)/L = 15 Ω/μm) at temperatures far above T_P.

The observed tendency toward insulator properties with decreasing crystal thickness agrees well with the expected behavior of a 1D electron system. In fact, at zero temperature, the conductivity of a 1D electron system in the presence of impurities must be zero, at least in the one-electron approximation [24]. The spreading and disappearance of the Peierls transition with decreasing thickness of quasi-1D conductors also points to the transition from quasi-1D to 1D electron spectrum: as is known, phase transitions in 1D systems are impossible. The realization of a 1D electron system depends on the electron and impurity concentrations, the strengths of the Coulomb and electron–phonon interactions, the type of screening, and other parameters of the physical system of interest. The experimental dependences (Figs. 1, 2) are adequately described by power laws [2, 3] or laws close to them [5, 6], both typical of 1D systems. This means that, in fact, we observe a continuous transition from the conduction typical of quasi-1D conductors with CDW to the conduction of 1D systems. In this case, the Peierls gap is smeared by fluctuations and becomes a pseudogap characteristic of 1D electron systems.

REFERENCES

1. F. D. M. Haldane, J. Phys. C: Sol. St. Phys. **14**, 2585 (1981).
2. C. L. Kane and M. P. A. Fisher, Phys. Rev. Lett. **68**, 1220 (1992).
3. C. L. Kane and M. P. A. Fisher, Phys. Rev. B **46**, 15233 (1992).
4. H. J. Schultz, Phys. Rev. Lett. **71**, 1864 (1993).
5. M. Fabrizio, A. O. Gegolin, and S. Schedel, Phys. Rev. Lett. **72**, 2235 (1994).
6. N. Nagaosa and A. Furasaki, J. Phys. Soc. Jpn. **63**, 413 (1994).
7. A. Dallmeyer, C. Carbone, W. Eberhardt, *et al.*, Phys. Rev. B **61**, R5133 (2000).
8. Ch. M. Lieber, Solid State Commun. **107**, 607 (1998).
9. X. Duan, J. Wang, and Ch. M. Lieber, Appl. Phys. Lett. **76**, 1116 (2000).
10. J. Heremans, C. M. Thrush, Y.-M. Lin, *et al.*, Phys. Rev. B **61**, 2921 (2000).
11. F. P. Milliken, C. P. Umbach, and R. A. Webb, Solid State Commun. **97**, 309 (1996).
12. A. M. Chang, L. N. Pfeiffer, and K. W. West, Phys. Rev. Lett. **77**, 2538 (1996).
13. M. Bockrath, D. H. Cobden, J. Lu, *et al.*, Nature **397**, 598 (1999).
14. J. Kim, K. Kang, J.-O. Lee, *et al.*, cond-mat/0005083.
15. S. V. Zaitsev-Zotov, Yu. A. Kumzerov, Yu. A. Firsov, and P. Monceau, J. Phys.: Condens. Matter **12**, L303 (2000).
16. L. Venkataraman and Ch. M. Leiber, Phys. Rev. Lett. **83**, 5334 (1999).
17. P. Monceau, in *Electronic Properties of Inorganic Quasi-One-Dimensional Conductors*, Ed. by P. Monceau (D. Reidel, Dortrecht, 1985), Part 2.
18. *Proceedings of International Workshop on Electronic Crystals ECRYS 93, ECRYS 99*; J. Phys. IV **3** (1993); **9** (1999).
19. D. V. Borodin, S. V. Zaĭtsev-Zotov, and F. Ya. Nad', Zh. Éksp. Teor. Fiz. **93**, 1394 (1987) [Sov. Phys. JETP **66**, 793 (1987)].
20. V. Ya. Pokrovskii, S. V. Zaitsev-Zotov, and P. Monceau, Phys. Rev. B **55**, 13377 (1997).
21. V. Ya. Pokrovskii and S. V. Zaitsev-Zotov, Phys. Rev. B **61**, 13261 (2000).
22. J. C. Gill, Synth. Met. **43**, 3917 (1991).
23. J. McCarten, M. Maher, T. L. Adelman, *et al.*, Phys. Rev. B **43**, 6800 (1991).
24. B. I. Shklovskiĭ and A. L. Éfros, *Electronic Properties of Doped Semiconductors* (Nauka, Moscow, 1979; Springer-Verlag, New York, 1984).

Translated by E. Golyamina

Hexavacancies in Crystalline Silicon

A. S. Kaminskiĭ

Institute of Radio Engineering and Electronics, Russian Academy of Sciences, Moscow, 103907 Russia
e-mail: kam@mail.cplire.ru
Received October 9, 2000; in final form, November 23, 2000

The kinetics of disorientation of B_{80}^4 centers is studied. The reorientation energy of the centers is determined to be ~1.5 eV. Based on the fact that this value is close to the energy of hexavacancy transition from the ground state to the first metastable state, it is concluded that the B_{80}^4 center is a ring hexavacancy. The reorientation mechanism is explained by the hexavacancy transition to the metastable state and, then, to a state with a new orientation. © *2001 MAIK "Nauka/Interperiodica".*
PACS numbers: 71.35.-y; 71.55.Cn

Earlier, in studying B_{80}^4 isoelectronic centers[1] and excitons bound to them, it was found that these centers are formed in pure silicon containing a large number of vacancies upon its annealing at ~375°C [1–3]. The centers belong to the trigonal system and are characterized by a point symmetry group no lower than C_{3V}. In addition, it was shown that excitons bound to B_{80}^4 belong to the "triplet–singlet" type, and a Hamiltonian describing all their properties was constructed [3]. Later [4], it was demonstrated that the B_{80}^4 centers can be almost totally oriented in one of the $\langle 111 \rangle$ directions. This paper presents the results obtained by studying the kinetics of disorientation of the B_{80}^4 centers.

Samples with dimensions $17 \times 1.25 \times 1.25$ mm were cut along the [111] direction from pure silicon that was preliminarily irradiated with neutrons (cadmium number ~50 and a dose of 10^{17} cm^{-2}). To initiate the formation of B_{80}^4 centers oriented in the [111] direction, the samples were subjected to uniaxial compression along this direction and annealed in the compressed state at 375°C for 30 min. If the samples already contained B_{80}^4 centers, the orientation of the latter in the desired direction could be achieved by annealing the compressed samples at a lower temperature of 250°C for ~30 min. To excite the samples, the radiation of a 200-mW argon laser was used. The spectral analysis of the recombination radiation (RR) was performed on an SDL-1 spectrometer. The RR detector was a cooled photomultiplier operating in the photon counting mode. The spectra were analyzed with a resolution of ~300 μeV. In the samples containing oriented B_{80}^4, the RR is polarized

---

and its spectral composition is strongly distorted on passing through the optical channel. To obtain correct results, the spectra of two RR components with mutually orthogonal polarizations were recorded and then combined.

According to [4], the intensity ratio I_1/I_2 of the $X_{80}^4 (J_1)$ and $X_{72}^4 (J_2)$ lines observed in the RR spectrum of the excitons bound to B_{80}^4 depends on the relations between the concentrations n_1, n_2, n_3, and n_4 of the centers oriented in the [111], [$\bar{1}$11], [$\bar{1}\,\bar{1}$1], and [1$\bar{1}$1] directions, respectively. When the centers are oriented in the [111] direction (i.e., $n_2 = n_3 = n_4$) and the radiation is detected in the direction perpendicular to [111], the ratio I_1/I_2 is determined by the expression [4]

$$I_1/I_2 = \frac{w(3 + 13x)}{3 + 5x}, \qquad (1)$$

where $x = n_2/n_1$ is the ratio of the concentration of the centers oriented in one of the equivalent directions [$\bar{1}$11], [$\bar{1}\,\bar{1}$1], or [1$\bar{1}$1] to the concentration of the centers oriented in the [111] direction, and the quantity w is determined from the experiment at $x \longrightarrow 1$ or $t \longrightarrow \infty$.

Introducing the vector $\mathbf{n} = \{n_1, n_2, n_3, n_4\}$ with the components whose sum is equal to the total concentration of centers, one can represent the time dependence of $\mathbf{n}$ in the form

$$\mathbf{n}(t) = G\mathbf{n}(0), \quad G = gI_4 + (1 - g)M/4, \qquad (2)$$

where G is the evolution operator of the vector $\mathbf{n}(t)$ for trigonal centers, $g = \exp(-4t/\tau)$, τ is the time of center reorientation, M is a matrix with elements all equal to unity, and I_4 is the identity matrix. When the centers are oriented along [111], the initial state of the centers can
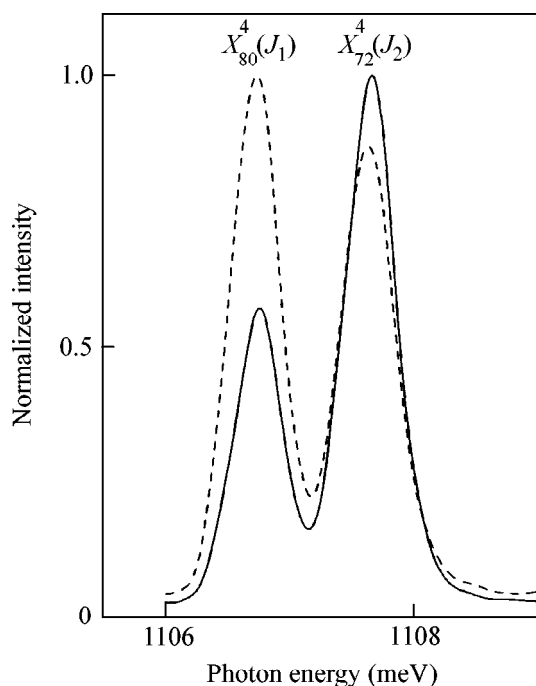
Fig. 1. Spectral distribution of the RR of excitons bound to the B_{80}^4 centers in undeformed silicon at 4.2 K. The annealing temperature is 375°C. The symbols in parentheses correspond to the line notations used in [1]. The RR spectra shown by the dashed and the solid lines refer to silicon annealed without compression and under a pressure of 0.24 GPa applied along the [111] direction, respectively. The spectra are not corrected for the distortions introduced by the optical channel.

be represented in the form $\mathbf{n}(0) = \{1 - 3p, p, p, p\}n$, where $p = n_2/n = n_3/n = n_4/n$. Then, one obtains from Eqs. (2)

$$x = n_2/n_1 = \frac{1 - g(1 - 4p)}{1 + 3g(1 - 4p)}. \tag{3}$$

One can see from Eqs. (1)–(3) that the dependences of the ratio I_1/I_2 on the time t of annealing at a fixed tem-

perature T can be used to determine the time of center reorientation $\tau(T)$. Assuming that the relationship [5]

$$1/\tau = a\exp(-E/kT) \tag{4}$$

is valid, one also obtains the reorientation energy E.

Figure 1 shows two spectra of the RR in silicon: one of them (solid line) corresponds to the beginning of the disorientation process, when the threefold axes of the majority of B_{80}^4 centers are parallel to [111], and the other (dashed line) corresponds to the end of the process, when the orientation of the centers corresponds to the equilibrium state.

Figure 2 presents two typical dependences of the ratio I_1/I_2 on the annealing time for different annealing temperatures. From the comparison of these experimental dependences with the dependences calculated by Eqs. (1) and (3), the reorientation times of the centers were determined at different temperatures. As a result, the experimental dependence of τ on T was obtained, from which the energy of center reorientation and the preexponential factor in Eq. (4) were determined: $E = 1.503$ eV and $a = 6 \times 10^{13}$ min^{-1}. Note that Eq. (4) fits well with the experiment in the temperature interval from 190 to 240°C.

To explain the results obtained above, it is natural to consider the centers consisting of vacancies, because the centers under study occur in abundance in pure silicon containing large numbers of vacancies (e.g., silicon irradiated with fast neutrons). The most suitable center that was not observed before and that belongs to the trigonal symmetry class is the theoretically predicted hexavacancy (V_6) [6]. Among the centers consisting of vacancies, the ring hexavacancy is the most stable. It can be represented as a cavity formed as a result of the elimination of six silicon atoms from the vertices of a spatial hexagon having the shape of a "chair" with the threefold axis parallel to [111]. In this case, the broken bonds are completely closed to each other. As a result, V_6 is electrically inactive [6], does not luminesce, and has an anomalously small dipole
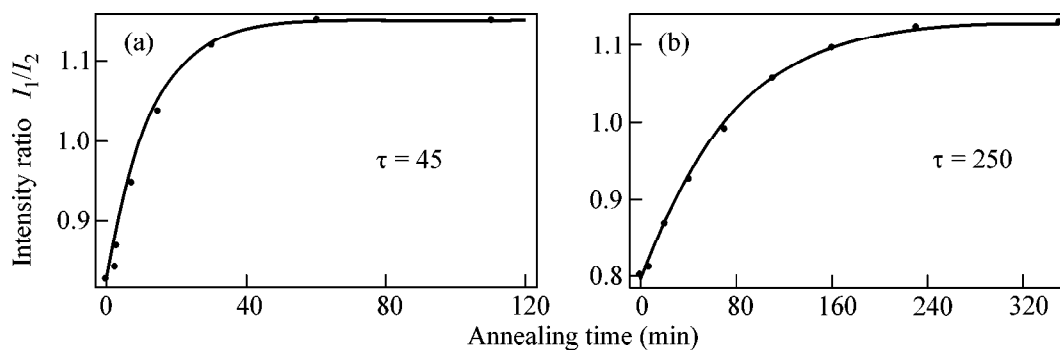
Fig. 2. Intensity ratio I_1/I_2 of the X_{72}^4 (J_1) and X_{80}^4 (J_2) lines versus the time of annealing at different annealing temperatures: (a) 217.5°C and (b) 195°C. The solid lines show the dependences calculated by Eqs. (1)–(3) at $w = 0.575$ and $p = 0.11$. The centers were oriented under a uniaxial compression ($P = 0.24$ GPa) of the samples along the [111] direction at 375°C.

moment. This all makes hexavacancies almost unde-tectable by conventional methods. According to theo-retical predictions, a large family of new centers can be formed on the basis of hexavacancies (in particular, the hexavacancy may contain two hydrogen atoms) [7].

The distinctive feature of V_6 is its ability to pass to a nonring metastable state with binding energy that, according to estimates [6], is lower than the binding energy of V_6 by ~0.87 eV. Taking into account that the reorientation energy of B_{80}^4 is close to this value, one can conclude that B_{80}^4 and V_6 are identical. Then, the reorientation process can be explained in the following way. As a result of thermal excitation, V_6 passes to the metastable hexavacancy state, after which it collapses into V_6 with a different orientation. The results pre-sented in this paper agree well with the theoretical study [7], where the idea that the ring hexavacancies V_6 should be identified with the B_{80}^4 centers was boldly put forward.

Thus, it is experimentally demonstrated that the B_{80}^4 centers can be identified with hexavacancies, and an unconventional mechanism of their reorientation is proposed.

REFERENCES

1. R. Sauer and J. Weber, Physica B (Amsterdam) **116**, 195 (1983).

2. A. S. Kaminskiĭ, A. N. Safonov, and É. V. Lavrov, Fiz. Tverd. Tela (Leningrad) **33**, 859 (1991) [Sov. Phys. Solid State **33**, 488 (1991)].

3. A. S. Kaminskiĭ and É. V. Lavrov, Zh. Éksp. Teor. Fiz. **108**, 1081 (1995) [JETP **81**, 595 (1995)].

4. A. S. Kaminskii and E. V. Lavrov, Solid State Commun. **108**, 751 (1998).

5. G. D. Watkins and J. W. Corbett, Phys. Rev. **121**, 1001 (1960).

6. J. L. Hastings, S. K. Estreicher, and P. A. Fedders, Phys. Rev. B **56**, 10215 (1997).

7. B. Hourahine, R. Jones, A. N. Safonov, *et al.*, Phys. Rev. B **61**, 12594 (2000).

Translated by E. Golyamina

New Scenario for the Decay
of Spin-Peierls State in CuGeO₃ : Fe.
Onset of a Quantum Critical Point

S. V. Demishev*, R. V. Bunting, L. I. Leonyuk[†], E. D. Obraztsova, A. A. Pronin,
N. E. Sluchanko, N. A. Samarin, and S. V. Terekhov

General Physics Institute, Russian Academy of Sciences, ul. Vavilova 38, Moscow, 119991 Russia

* *e-mail: demis@lt.gpi.ru*

It is found experimentally that the introduction of 1% Fe in the CuGeO₃ matrix gives rise to a strong disorder in the magnetic subsystem and leads to an appearance of the $\chi \sim 1/T^{\alpha}$ ($\alpha \approx 0.36$) low-temperature asymptotic form for magnetic susceptibility over a wide temperature range $1.7 \le T \le 30$ K. A model attributing this anomaly to the suppression of spin-Peierls state as a result of the formation of the quantum critical point is proposed. © 2001 MAIK "Nauka/Interperiodica".

PACS numbers: 75.30.Cr; 75.40.-s; 75.50.Lk

1. It is well known that the doping suppresses the spin-Peierls transition in CuGeO₃. Numerous studies devoted to the effect of impurities such as Zn, Si, Ni, Co, Mg, and Mn have demonstrated that the transition temperature T_{sp} decreases with increasing impurity concentration x and, for $x > x_c$, the dimerization coexists with antiferromagnetism at $T < T_N$ (see [1–4] and references cited therein).

For example, the microwave magnetic-resonance spectra of CuGeO₃ show at $T < T_N$ the antiferromagnetic resonance lines coexisting with electron paramagnetic resonance (EPR) of impurities and (or) lattice defects. Theoretically, this effect is explained by the fact that the impurity or the defect in a dimerized matrix is surrounded by a "cloud" of antiferromagnetically correlated spins, and the overlap between such clouds gives rise to the long-range magnetic order [5, 6].

A further increase in the impurity concentration completely suppresses the spin-Peierls transition and only the transition to the antiferromagnetic state is retained. The $T_N(x)$ dependence is nonmonotonic; the Néel temperature first increases with concentration, passes through a maximum, and then starts to decrease at high doping levels. Interestingly, the concentration phase diagrams can be brought to the universal form upon scaling the x axis [2]. This is ordinarily considered as evidence for a universal mechanism [5, 6] of destruction of the spin-Peierls state, regardless of the

chemical nature of the impurity. In our opinion, such a universal scenario is not the only possible mechanism of the doping effect on the spin-Peierls state of CuGeO₃. Let us consider, as an alternative, the results of theoretical works [7–11], where the effect of disorder was studied for various low-dimensional spin systems such as one-dimensional chains with antiferromagnetic and ferromagnetic interactions, two-dimensional Ising glass, three-dimensional heavy-fermion systems with antiferromagnetic correlations, and the dimerized $S = 1/2$ chains. An analysis carried out in [7–11] showed that, independently of the type of interaction and the dimensionality, such spin systems exhibit very similar behavior: the disorder smears the phase transition in such a way that the $T = 0$ point becomes critical [so-called quantum critical point (QCP)]. Simultaneously, the thermodynamic properties at $T \longrightarrow 0$ become dominated by the sparse strongly correlated (compared to the mean values) clusters giving rise to the Griffiths singularities [12]. This results in the low-temperature divergence of magnetic susceptibility

$$\chi \propto 1/T^{\alpha}, \qquad (1)$$

where $\alpha < 1$. An analogous result was also obtained for the one-dimensional $S = 1/2$ chain with antiferromagnetic interaction [7, 10], for which the antiferromagnetic transition is absent at low temperature. Note that the possibility of QCP appearing follows from the standard scenario of the decay of spin-Peierls state, because $T_N(x) \longrightarrow 0$ as $x \longrightarrow \infty$. However, the possible deviations

---

[†] Deceased.
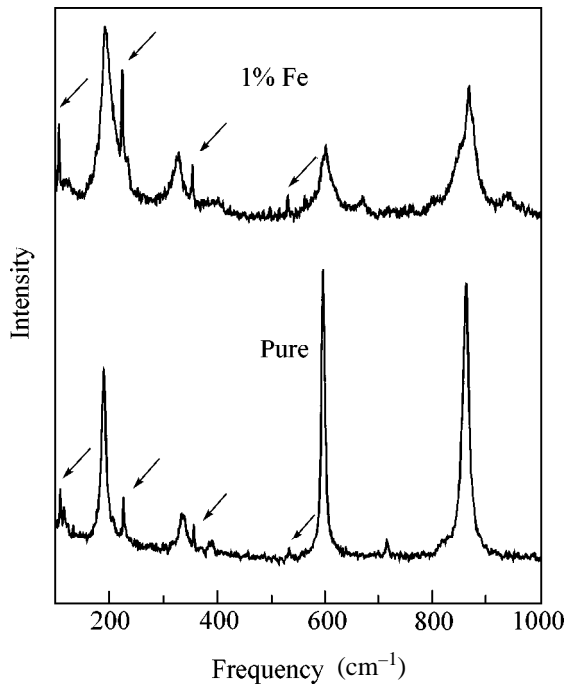
Fig. 1. Raman spectra of pure and iron-doped $CuGeO_3$ at $T = 300$ K. Arrows indicate the discharge lines.
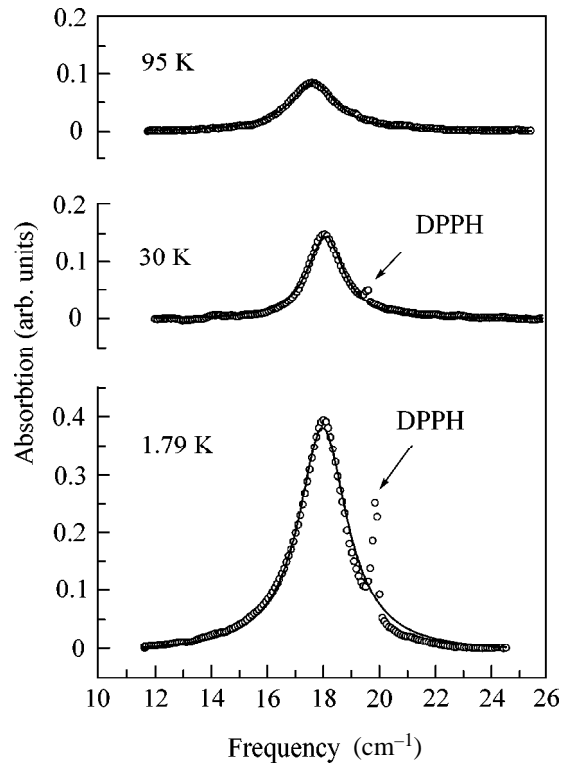
Fig. 2. EPR spectra of $CuGeO_3$: Fe at different temperatures.

from the Curie law $\chi \sim 1/T$ were either not observed for $CuGeO_3$ at $T \longrightarrow 0$ or interpreted within the framework of the antiferromagnetic ordering model [3].

In this work, we present experimental data indicating that the decay of spin-Peierls state in $CuGeO_3$ can be caused by the formation of a quantum critical point and, generally, is not associated with the formation of the long-range antiferromagnetic order.

2. Iron-doped $CuGeO_3$ samples were chosen for the investigation. The samples were synthesized by the method described in [13, 14] and identical to that used in [2]. Chemical analysis suggested that the $CuGeO_3$: Fe samples contained 1% iron. The sample structure was monitored by X-ray diffraction and by the Raman scattering spectra. To reveal the disorder effects, samples of pure $CuGeO_3$ synthesized by the same method were used as a reference (their physical properties had been studied earlier in [13, 14]).

The magnetic properties of the samples were studied by EPR. Experimentally, transmittance was recorded as a function of magnetic field H for a cylindrical cavity with the sample (TE_{011} mode, $Q = 10^4$, resonance frequency $f \sim 60$ GHz); BWT-based radiation sources were used. The external magnetic field was parallel to the crystallographic a axis. A DPPH crystal was placed in the cavity for the accurate determination of the g factor.

3. The X-ray structural data did not show a noticeable change in the lattice parameters of $CuGeO_3$ upon doping with iron. At the same time, the Raman spectra suggest a strong disorder effect. One can clearly see in Fig. 1 that the introduction of Fe into the $CuGeO_3$ matrix brings about a strong broadening and decrease in amplitude for the main A_g modes [15] at 187, 332, 594, and 859 cm^{-1}. The 594 and 859 cm^{-1} modes, corresponding to different vibrations of oxygen atoms [15], are strongly suppressed compared to the 187 cm^{-1} mode (the in-phase vibrations of the Ge and O atoms).

Since the doping does not shift the main frequencies due, according to [15], to the vibrations of the GeO_3^{2-} complexes, the replacement of the germanium atoms by the impurity iron atoms seems to be improbable, so that one may assume that the iron atoms in $CuGeO_3$: Fe are built in the copper chains.

The magnetic resonance spectrum of $CuGeO_3$: Fe shows a single EPR line over the entire temperature range studied (1.7–300 K, Fig. 2). It should be emphasized that the low-temperature spectra of the doped samples did not show any satellites [13] or several absorption lines with comparable amplitudes [16], or even antiferromagnetic resonance lines (the latter was checked by us additionally in the frequency range 20–120 GHz using nonresonance technique described in [13]).

Line shape analysis showed that it is described well by a Lorentzian at all temperatures studied (Fig. 2). The
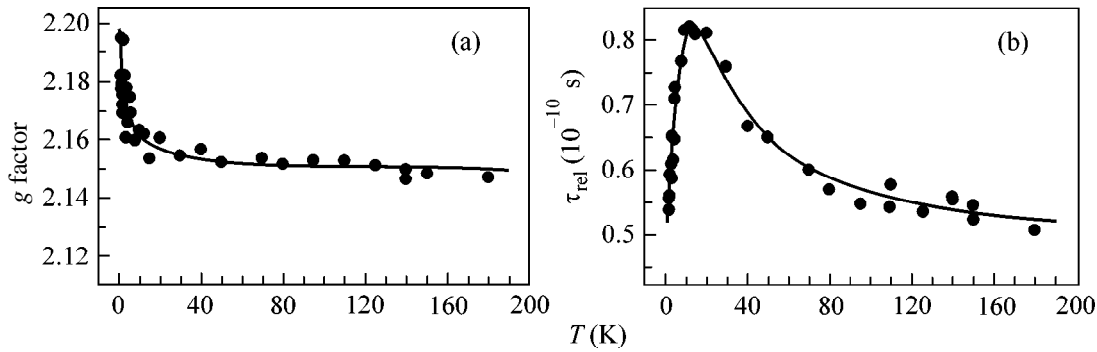
Fig. 3. Temperature dependence of (a) the g factor and (b) the relaxation time.

temperature dependences of the g factor, the relaxation time τ_{rel}, and the integrated intensity χ were calculated for the best fit of the experimental spectra to the Lorentzian curve. The latter parameter is proportional to the magnetic susceptibility of free spins [17]. The resulting data are shown in Figs. 3 and 4. At $T > 20$ K, the g factor of $CuGeO_3$: Fe equals 2.15 and is independent of temperature (Fig. 3a). Notice that this value is observed for the **H** ∥ **a** geometry in pure $CuGeO_3$. However, contrary to pure $CuGeO_3$, for which the g factor remains constant down to $T \sim 0.5$ K [13], in $CuGeO_3$: Fe this parameter increases approximately by 2% upon lowering the temperature from 20 to 1.7 K (Fig. 3a). It is likely that the temperature renormalization of the $CuGeO_3$: Fe g factor is due to the increased role of the interaction between the copper and iron magnetic moments at $T \leq 20$ K. Interestingly, the relaxation time passes through a maximum (Fig. 3b) and then decreases in the range $T \leq 20$ K; accordingly, the resonance width, being inversely proportional to τ_{rel}, increases at these temperatures (Figs. 2, 3b). Such behavior can also be explained by the dominant role of the disorder effects at $T \leq 20$ K in $CuGeO_3$: Fe (otherwise the relaxation time should increase with lowering temperature [17]).

The most pronounced distinction between the samples of doped and pure $CuGeO_3$ is observed in the temperature dependences of their integrated intensities (Fig. 4). A broad maximum in the vicinity of $T \sim 80$ K in the $\chi(T)$ curve of the pure sample gives way to an exponential decrease at $T < T_{sp}$ because of the appearance of a gap in the spectrum of magnetic excitations. At the same time, the $\chi(T)$ dependence in $CuGeO_3$: Fe has a cardinally different type: the integrated intensity first increases following the Curie law $\chi(T) \sim 1/T$ with decreasing temperature in the range 70–180 K (Fig. 4, curve 1), whereupon the temperature dependence has a plateau $\chi(T) \approx$ const in the range 30–70 K. A further decrease in temperature at $1.7 \leq T \leq 30$ K gives way to a new portion of $\chi(T)$ increase described by Eq. (1) with exponent $\alpha \approx 0.36$ (Fig. 4, curve 2 and inset in Fig. 4). The data in Fig. 4 allow the conclusion to be drawn that

the spin-Peierls state is completely suppressed by the introduction of 1% Fe in the $CuGeO_3$ matrix. This conclusion correlates with the absence, up to 50 T, of the low-temperature magnetic transition,[1] which is observed for pure $CuGeO_3$ in a field of ~13 T and is a characteristic feature of the spin-Peierls state [14].

4. Thus, we have shown that the doping with iron and the ensuing disorder of the spin-Peierls copper chains suppresses the spin-Peierls transition and leads to the appearance of a low-temperature asymptotic law $\chi(T) \sim 1/T^\alpha$ that is substantially different from the standard Curie law.

It is worth noting that the anomalous temperature dependence $\chi(T)$ is observed over a wide range of $1.7 \leq T \leq 30$ K, where the temperature changes by more than 17 times (Fig. 4). No deviation from dependence (1) was observed in our experiments down to the lowest attainable temperature. Since antiferromagnetic resonance was not observed, such behavior occurs in the absence of the long-range antiferromagnetic order, which, according to the standard scenario, should appear upon doping $CuGeO_3$ with impurity atoms [5, 6]. It would thus be logical to rationalize the unusual low-temperature asymptotic behavior $\chi(T) \sim 1/T^{0.36}$ for $CuGeO_3$: Fe in terms of the formation of the quantum critical point.

This interpretation is in full agreement with the prediction made in [10] for a one-dimensional antiferromagnetic $S = 1/2$ chain in a random dimer (RD) phase. For a weak dimerization, the spectrum of the RD phase is gapless and, instead of decreasing, the susceptibility would increase following Eq. (1) with the index $\alpha < 1$, typical of the Griffiths phase in the vicinity of QCP [10].

According to [10], the exponent α is not a universal quantity because it depends on the bond distribution function. Nevertheless, both theoretical calculations [8] and experimental results [18] yield for QCP the values $\alpha \sim 0.30$–0.33, which are close to $\alpha \approx 0.36$ obtained in

---

[1] L. Weckhuysen, private communication.
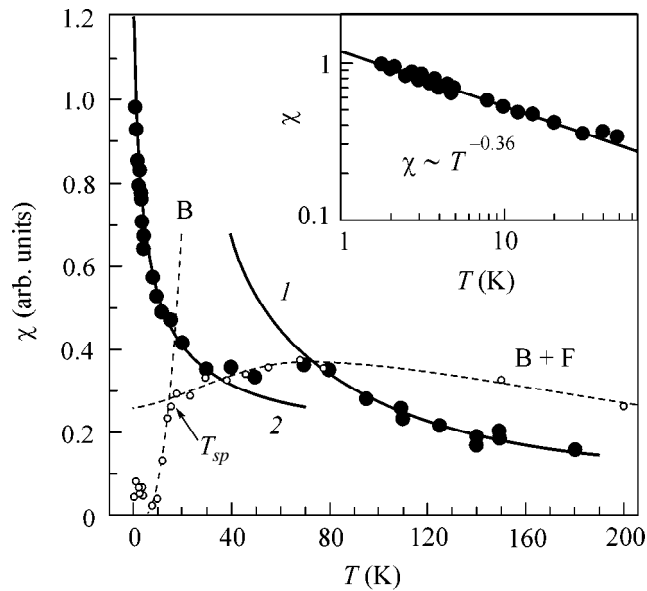
Fig. 4. Temperature dependence of the integrated intensity $\chi(T)$ for the samples of (light circles) pure and (dark circles) iron-doped $CuGeO_3$: (*1*) Curie law $\chi(T) \sim 1/T$ and (*2*) asymptotic form $\chi \sim 1/T^\alpha$ with $\alpha = 0.36$. Inset: log–log plot of the low-temperature asymptotic power-law dependence $\chi(T)$. Experimental data for the pure sample are taken from [13]; the dashed lines are the calculated $\chi(T)$ dependences: (B–F) Boner–Fisher law and (B) Bulaevskiĭ law (from [13]).

this work. This also may serve as an additional argument in favor of the suggested explanation.

The analysis carried out in this work indicates that $CuGeO_3$: Fe, apparently, exhibits a new scenario of suppressing the spin- Peierls state through the formation of the quantum critical point. In this connection, it would be quite promising to study the magnetic properties of the doped spin-Peierls compounds, in particular, $CuGeO_3$: Fe, at ultralow temperatures.

REFERENCES

1. M. Hase, J. Magn. Magn. Mater. **177–181**, 611 (1998).
2. B. Grenier, J.-P. Renard, P. Veillet, *et al.*, Phys. Rev. B **57**, 3444 (1998).
3. P. E. Anderson, J. Z. Liu, and R. N. Shelton, Phys. Rev. B **56**, 11014 (1997).
4. V. N. Glazkov, A. I. Smirnov, O. A. Petrenko, *et al.*, J. Phys.: Condens. Matter **10**, 7879 (1998).
5. H. Fukuyama, T. Tanimoto, and M. Saito, J. Phys. Soc. Jpn. **65**, 1182 (1996).
6. M. Mostovoy, D. Khomskii, and J. Knoester, cond-mat/9712098 (1997).
7. D. S. Fisher, Phys. Rev. Lett. **69**, 534 (1992); Phys. Rev. B **50**, 3799 (1994); Phys. Rev. B **51**, 6411 (1995).
8. H. Reiger and A. P. Young, cond-mat/9512162 (1995).
9. M. Fabrizio and R. Melin, Phys. Rev. Lett. **78**, 3382 (1997).
10. R. A. Hyman, K. Yang, R. N. Bhutt, and S. M. Girvin, Phys. Rev. Lett. **76**, 839 (1996).
11. A. Rosch, in *Abstracts of LT22, Helsinki, 1999*, p. 389.
12. R. B. Griffiths, Phys. Rev. Lett. **23**, 17 (1969).
13. S. V. Demishev, A. V. Semeno, N. E. Sluchanko, *et al.*, Zh. Éksp. Teor. Fiz. **112**, 1727 (1997) [JETP **85**, 943 (1997)].
14. S. V. Demishev, L. Weckhuysen, J. Vanacken, *et al.*, Phys. Rev. B **58**, 6321 (1998).
15. Z. V. Popović, S. D. Dević, V. N. Popov, *et al.*, Phys. Rev. B **52**, 4185 (1995).
16. A. I. Smirnov, V. N. Glazkov, A. N. Vasil'ev, *et al.*, Pis'ma Zh. Éksp. Teor. Fiz. **64**, 277 (1996) [JETP Lett. **64**, 305 (1996)].
17. S. A. Al'tshuler and B. M. Kozyrev, *Electron Paramagnetic Resonance* (Fizmatgiz, Moscow, 1961; Academic, New York, 1964).
18. B. Andraka and A. M. Tsvelik, Phys. Rev. Lett. **67**, 2886 (1991).

Translated by V. Sakun

Relativistic Effects in PtF$_6$ and Isoelectronic Octahedral Groups: Magnetic Susceptibility, ^{19}F NMR, and *ab initio* Calculations

S. P. Gabuda*, V. N. Ikorskiĭ, S. G. Kozlova, and P. S. Nikitin

Institute of Inorganic Chemistry, Siberian Division, Russian Academy of Sciences, pr. Akademika Lavrent'eva 3, Novosibirsk, 630090 Russia
* e-mail: gabuda@casper.che.nsk.su
Received December 1, 2000

The temperature-independent paramagnetism and high O_h symmetry of PtF$_6$ molecules in solids (at 77 K) and of the octahedral molecular complexes [IrF$_6$]$^-$ in KIrF$_6$ and [OsF$_6$]$^{2-}$ in K$_2$OsF$_6$ are shown to be consistent with the model of strong spin–orbit coupling of $5d^4$ electrons. © *2001 MAIK "Nauka/Interperiodica"*.

PACS numbers: 31.30.Jv; 75.30.Cr

PtF$_6$ molecules are characterized by regular octahedral structure and point group symmetry O_h in both the gas phase [1–5] and two crystalline modifications, bcc and orthorhombic [3]. At the same time, a similar PdF$_6$ hexafluoride is unknown, while the isoelectronic [RuF$_6$]$^{2-}$ anions in the M$_2$RuF$_6$ (M = K, Rb, and Cs) compounds are known to be characterized by the tetragonal distortion of the Jahn–Teller type [1–3]. One may assume that the instability of the hypothetical PdF$_6$ molecule is caused by vibronic effects [4]. If so, the question arises of the mechanism of stabilization of high O_h symmetry and suppression of vibronic instability of the PtF$_6$ molecules and the isoelectronic [IrF$_6$]$^-$ and [OsF$_6$]$^{2-}$ anions in compounds of the M$_2$OsF$_6$ and MIrF$_6$ type [1–3].

Experimental evidence for a high symmetry of the PtF$_6$ molecules and the isoelectronic [IrF$_6$]$^-$ and [OsF$_6$]$^{2-}$ anions [3] is provided by solid-state high-resolution ^{19}F NMR data. In this work, we examine how the anomalous ^{19}F NMR chemical shifts correlate with the van Vleck paramagnetism of PtF$_6$, KIrF$_6$, K$_2$OsF$_6$, and K$_2$RuF$_6$ and with the symmetry predicted for octahedral molecules and molecular ions by the quantum-chemical *ab initio* calculations.

Samples of KIrF$_6$, K$_2$OsF$_6$, and K$_2$RuF$_6$ were prepared by the method described earlier in [5, 6]. Temperature measurements of magnetic susceptibilities χ of the compounds were performed by the Faraday method in the range 4.2–300 K in magnetic fields of up to 1 T. Co[Hg(SCN)$_4$] salt was used as a reference for calibration [6]. Instrumental error in χ was ±1%. The diamagnetic contributions χ_d were calculated using the additive Pascal scheme [7]. The resulting χ_d values are presented in Table 1. The temperature-independent (van

Vleck) paramagnetic contribution χ_p was separated from the measured paramagnetic susceptibility χ by subtracting the temperature-dependent paramagnetism, according to the Curie–Weiss law:

$$\chi = C/(T - \theta) + \chi_0, \tag{1}$$

where $\chi_0 = \chi_d + \chi_p$ is the temperature-independent component of magnetic susceptibility and χ_d is the correction for the diamagnetism of the sample. The results of measurements are presented in the figure and analyzed in Table 1.

The experimental magnetochemical data for PtF$_6$ were obtained earlier in [8]. It was found that the magnetic susceptibility of PtF$_6$ is also independent of temperature and, hence, corresponds to the van Vleck paramagnetism with $\chi_p(\text{PtF}_6) = 812 \times 10^{-6}$ cm^3/mol. This fact was considered as evidence of the spin-paired $5d^4$ state of the Pt^{6+} ion in platinum hexafluoride. The
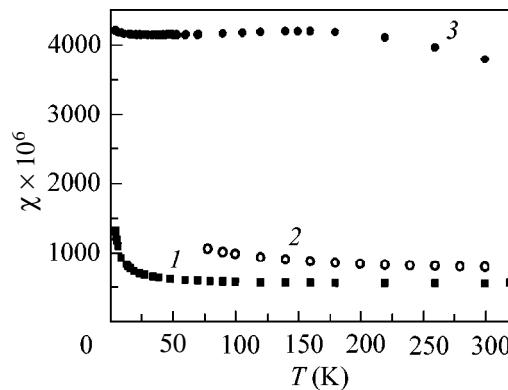
Temperature dependences of magnetic susceptibilities of (*1*) K$_2$RuF$_6$, (*2*) KIrF$_6$, and (*3*) K$_2$OsF$_6$.

Table 1. Magnetic susceptibility components of $KIrF_6$, K_2OsF_6, and K_2RuF_6

	$\chi_p \times 10^6$, cm³/mol	$-\chi_d \times 10^6$, cm³/mol	$C \times 10^3$, (cm³ K)/mol	$-\theta$, K
$KIrF_6$	685 ± 7	99	30.5	3.1 ± 1.5
K_2OsF_6	538 ± 5	121	4.04	0.9 ± 0.2
K_2RuF_6	4138 ± 42	110	0.276	-0.7 ± 0.6

temperature-independent paramagnetism is due to the mixing (induced by the external magnetic field) of the ground and excited states of the Pt^{6+} ion having electronic configuration $5d^4$. The applied external magnetic field polarizes the electronic shell of the Pt^{6+} ion, i.e., admixes the excited-state wave functions to the ground state and, thus, partially "freezes out" the orbital angular momentum of the spin-paired $5d^4$ electrons. As a result, the ion ground state acquires an induced magnetic moment parallel and proportional to the applied magnetic field [9, 10]. Such an induction gives rise to the induced local magnetic fields at the nuclei of surrounding atoms, leading to the broadening and shifting of the NMR spectra. In the NMR spectrum of a van Vleck paramagnet, the shift σ_{iso} is linearly related to the magnetic susceptibility χ_p [11]:

$$\sigma_{iso} = (2\pi A_s / g\mu_B \gamma h)\chi_p, \qquad (2)$$

where g is the nuclear g factor, μ_B is the Bohr magneton, γ is the nuclear gyromagnetic ratio, and h is Planck's constant. The experimental parameter A_s is the constant of hyperfine interaction of the ^{19}F nucleus with the spin density induced at the 2s orbitals of the fluoride ion.

Table 2 presents the experimental σ_{iso} values measured earlier [1–3] for the compounds of interest, as well as the longitudinal ($\sigma_\parallel$) and transverse ($\sigma_\perp$) components of the ^{19}F magnetic shielding tensor. In Table 2, the absolute scale of fluorine NMR chemical shifts is used, for which the shielding of the ^{19}F nucleus of a free $[F]^-$ ion is taken as a reference; in this scale, the shielding constant of the gaseous fluorine nuclei is $\sigma(F_2) = -713$ ppm [2, 12]. The corrections suggested in [3] for the interference of the anisotropy effects in magnetic

shielding and dipole–dipole interactions of the ^{19}F nuclei (so-called cross-singular distortions [3]) are taken into account in Table 2. The $\sigma_\parallel$ and $\sigma_\perp$ parameters for two overlapping $K_2[RuF_6]$ NMR lines were newly calculated using the spectra obtained in [1, 2]. The uncertainty in these parameters is 2–3%, as in the other cases. Both cross-singular distortions and high-resolution ^{19}F NMR spectra obtained in [3] for $K_2[RuF_6]$ in fields of 2.1 and 5 T were taken into account in the analysis.

The data on χ_p and σ_{iso} and Eq. (2) were used to calculate the A_s coefficients (Table 2). These coefficients allow the estimation of the $f_s = A_s/A_s[F^0]$ values characterizing the fraction of unpaired 2s-electron density at the F^- ion nuclei in the compounds considered. The calculations were carried out using the tabulated value $A_s[F^0] = 4.51 \times 10^{10}$ Hz that is adopted for the free fluorine atoms [12]. The results correlate well with the f_s values measured earlier [13] for the fluorine nuclei in binary iridium and rhodium pentafluorides IrF_5 [$f_s(2F_1) = 0.45\%$; $f_s(2F_2) = 0.38\%$; and $f_s(F_3) = 0.12\%$] and RhF_5 [$f_s(2F_1) = 0.04\%$; $f_s(2F_2) = 0.34\%$; and $f_s(F_3) = 0.89\%$].

Two main features of $K_2[RuF_6]$ (palladium group) are worthy of notice: the small parameters A_s and f_s, on the one hand, and the structural distortion of the octahedral $[RuF_6]^{2-}$ ions, resulting in the positional nonequivalence of the fluorine atoms (F_1 and F_2), on the other. To elucidate the origin of the structural distortion, *ab initio* quantum-chemical calculations were performed for the molecular and electronic structures of the coordination hexafluoro groups $[MF_6]^{n-}$ [$n = 0, 1,$ and 3, and M is the transition metal with electronic configuration $4d^4$ (palladium group) or $5d^4$ (platinum group)] with inclusion of the vibronic interactions. The calculations were carried out by the Hartree–Fock method using the Jaguar 3.5 program package for quantum-chemical calculations [14]. For Pt, Ir, and Os atoms, a quasi-relativistic atomic basis set was chosen [15], and, for F atoms, the 6–31$G(p, d)$ atomic basis was used [16]. It is essential that the spin–orbit interaction was disregarded in this method. The calculated geometries of the PtF_6 molecule and isoelectronic molecular anions $[IrF_6]^-$ and $[OsF_6]^{2-}$ are given in Table 3.

Table 2. Experimental values of principal components of ^{19}F magnetic shielding tensor, hyperfine interaction constants A_s, and fraction of unpaired electrons at the 2s orbitals of fluoride ions

	$-\sigma_\parallel$, ppm	$-\sigma_\perp$, ppm	$-\sigma_{iso}$	λ^{so}, cm^{-1}	A_s, 10^6	f_s, %
PtF_6	6900	3700	4800	12082	263.6	0.585
$K[IrF_6]$	3360	1900	2390	10256	155.7	0.346
$K_2[OsF_6]$	1880	1240	1560	8464	129.4	0.287
$K_2[RuF_6]$ ($2F_1$)	8860	5370	6530	2854	70.5	0.156
″ ($4F_2$)	9660	6170	7330	″	78.9	0.175

According to the calculations, the expected symmetry of the PtF_6 molecule and $[IrF_6]^-$ and $[OsF_6]^{2-}$ anions lowers because of the Jahn–Teller orthorhombic distortion of point group symmetry D_{2h}. Nevertheless, the degree of deviation from tetragonal symmetry is small for orthorhombically distorted molecules: the calculated distinctions for the four shortest $4D(M–F_2)$ bonds appear only in the fifth decimal place. Thus, the calculated symmetry is quasi-tetragonal for all octahedral groups and corresponds to the octahedra stretched along the C_4 axis. The calculated energy spectra and electron distributions over the states suggest that the triplet state t_{2g} is split in the tetragonal field into a singlet and a lower lying doublet, with four $5d^4$ electrons occupying the $5d_{xz}$ and $5d_{yz}$ atomic orbitals in the spin-paired state.

A comparison of the data in Tables 2 and 3 shows that the agreement between the *ab initio* calculations and the experiment holds only for $K_2[RuF_6]$. Indeed, the ~6% relative difference in the $D(Ru–F_1)$ and $D(Ru–F_2)$ distances is in qualitative agreement with the experimentally observed difference of ~10% between $\sigma_{iso}(2F_1)$ and $\sigma_{iso}(4F_2)$. The relation between σ_{iso} and $D(M–F)$ follows from Eq. (1) and the fact that the hyperfine interaction constant A_s is proportional to the overlap integral between the orbitals of the central atom and the ligands and, hence, depends on the interatomic distance as $\exp(–D/D_0) \approx 1 – D/D_0$. At the same time, there are no indications of the structural distortions in the coordination hexafluoro groups PtF_6, $[IrF_6]^-$, and $[OsF_6]^{2-}$; their point group symmetry was found to be O_h. This fact gives evidence for the occurrence of a mechanism that "switches off" or "suppresses" the vibronic effects in platinum metal hexafluoro coordination compounds.

The mechanism of stabilizing the high-symmetry (O_h) octahedral configurations of the PtF_6 molecule and $[IrF_6]^-$ and $[OsF_6]^{2-}$ anions may be associated with the large spin–orbit coupling constant λ^{so}, which was disregarded in the *ab initio* calculation. The spin–orbit coupling splits the atomic d levels into pairs of sublevels, the lower $d_{3/2}$ doublet and the upper $d_{5/2}$ triplet, with the splitting being equal to λ^{so}. The λ^{so} values calculated by the Dirac–Fock method [17] for Pt, Ir, Os, and Ru atoms are given in Table 2. One can see that the λ^{so} value for Ru is approximately an order of magnitude

smaller than the value of $10Dq \approx 15–20 \times 10^3$ cm^{-1} typical of octahedral palladium group complexes. This allows the λ^{so} parameter to be treated as a perturbation with respect to the crystal field. In this case, the ground state of the system is spin-paired, which corresponds to the occupation of the $4d_{xz}$ and $4d_{yz}$ orbitals of the central atom. The spin–orbit perturbation mixes this ground (singlet) state with the nearest excited $4d_{xy}$ state and, hence, is responsible for the observed orbital paramagnetism.

By contrast, the spin–orbit interaction in platinum metals is on the order of the crystal-field energy of their ions. Qualitative electrostatic considerations suggest that the lower relativistic $d_{3/2}$ ($m = \pm 3/2; \pm 1/2$) level of the electronic $5d^4$ configuration remains spin-paired and ground state in the octahedral field. The crystal field is strong in this case and cannot be treated as a perturbation, while the ion ground state is mixed with the excited $d_{5/2}$ ($m = \pm 1/2$) state. Therefore, because of a relatively strong spin–orbit interaction, the ground-state wave functions of the PtF_6 molecule and $[IrF_6]^-$ and $[OsF_6]^{2-}$ anions are essentially different from the ground-state wave functions of the analogous molecules and anions of palladium metal hexafluoro coordination compounds. This distinction may be the main reason for a drastic (by a factor of ~5) difference in the magnetic susceptibilities and the A_s and f_s parameters of $K_2[RuF]$, on the one hand, and of PtF_6, $KIrF_6$, and K_2OsF_6, on the other.

The above analysis also provides the qualitative explanation of the enhanced stability of PtF_6, as compared to PdF_6. In our *ab initio* calculations (without regard for the spin–orbit interaction), we determined the energies of formation from elements for PtF_6 and PdF_6 molecules. The dissociation energy of both PdF_6 and PtF_6 molecules is positive: $U_e(PdF_6) = +6.60$ eV and $U_e(PtF_6) = +0.03$ eV, indicating that both systems are unstable (if the spin–orbit interaction is neglected). However, the inclusion of the spin–orbit interaction diminishes the calculated U_e value by a value on the order of $3/5\lambda^{so}$. For PdF_6 molecules [$\lambda^{so}(Pd) \approx 0.5$ eV], this contribution has no effect on the stability, whereas for PtF_6 [$\lambda^{so}(Pt) \approx 1.5$ eV] the contribution of the spin–orbit interaction is large enough for providing the stability of PtF_6 hexafluoride.

The study presented in this work demonstrates that relativistic effects play the important part in the inter-

Table 3. Results of *ab initio* Hartree–Fock calculations of the intramolecular M–F distances in the octahedral molecular complexes $[MF_6]^{n-}$ ($n = 2, 1,$ and 0)

$[MF_6]^{n-}$	$[RuF_6]^{2-}$	$[RhF_6]^-$	PdF_6	$[OsF_6]^{2-}$	$[IrF_6]^-$	PtF_6
Point group	D_{2h}	D_{2h}	D_{2h}	D_{2h}	D_{2h}	D_{2h}
$2D(M–F_1)$, Å	1.97435	1.87753	1.8378	2.0165	1.912	1.862
$4D(M–F_2)$, Å	1.88344	1.80165	1.76507	1.9111	1.826	1.781

pretation of the properties of the compounds of platinum transition elements.

REFERENCES

1. S. V. Zemskov, S. P. Gabuda, and V. N. Mit'kin, Zh. Strukt. Khim. **17** (3), 483 (1976).

2. S. V. Zemskov and S. P. Gabuda, Zh. Strukt. Khim. **17** (5), 904 (1976).

3. É. P. Zeer, V. E. Zobov, and O. V. Falaleev, *New Effects in NMR of Polycrystals* (Nauka, Novosibirsk, 1991).

4. B. Weinstock, J. Phys. Chem. Solids **18**, 86 (1961).

5. R. Glauber and V. Schomaker, Phys. Rev. **89**, 667 (1953).

6. V. T. Kalinnikov and Yu. V. Rakitin, *Introduction to Magnetochemistry: Method of Static Magnetic Susceptibility* (Nauka, Moscow, 1980).

7. P. W. Selwood, *Magnetochemistry* (Interscience, New York, 1956; Inostrannaya Literatura, Moscow, 1958).

8. R. Blinc, E. Pirkmajer, J. Slivnik, and I. Zupancic, J. Chem. Phys. **45** (5), 1488 (1966).

9. J. H. van Vleck, *Theory of Electric and Magnetic Susceptibilities* (Oxford Univ. Press, Oxford, 1932).

10. S. V. Vonsovskiǐ, *Magnetism* (Nauka, Moscow, 1971; Wiley, New York, 1974).

11. S. A. Al'tshuler and M. A. Teplov, in *Magnetic Resonance of van Vleck Paramagnets*, Ed. by L. E. Kononenko (Nauka, Moscow, 1978).

12. S. P. Gabuda, Yu. V. Gagarinskiǐ, and S. A. Polishchuk, *NMR in Inorganic Fluorides* (Atomizdat, Moscow, 1978).

13. T. Cyr, Can. J. Spectrosc. **19** (5), 136 (1971).

14. *Jaguar 3.5* (Schrodinger, Portland, 1998).

15. W. R. Wadt and P. J. Hay, Chem. Phys. **82** (1), 284 (1985).

16. P. C. Hariharan and J. A. Pople, Theor. Chim. Acta **28**, 213 (1973).

17. J. P. Desclaux, At. Data Nucl. Data Tables **12**, 311 (1974).

Translated by V. Sakun

Ground State of a Mixture of Resonant Condensates

L. A. Manakova

Russian Research Center Kurchatov Institute, pl. Kurchatova 1, Moscow, 123182 Russia

It is shown that a two-component mixture of resonant condensates can be unstable toward the transition to the state with spontaneous Josephson oscillations in the absolute minimum of thermodynamic potential. The transition occurs stepwise at a certain critical value of the total number of particles or chemical potential. © *2001 MAIK "Nauka/Interperiodica".*

PACS numbers: 03.75.Fi; 05.30.Jp; 32.80.Pj; 74.50.+r

1. Since the discovery of two-component condensates [1], the phenomena caused by phase coherence of two condensate modes attract considerable interest, both experimental and theoretical (see, e.g., [2, 3]). In numerous studies devoted to the Josephson effect (see [4] and references therein) in a system of two condensates in different m_F states [3, 5] or in a double-well potential [6, 7], coherent Josephson oscillations were considered for various dynamic regimes caused by the competition between tunneling and intracondensate interaction (nonlinearity). For a relatively weak interaction, the particle number oscillations between the condensates are complete. They are suppressed when the total number of atoms in the condensates exceeds a critical value and the behavior of the system is governed by the nonlinearity [7]. However, the thermodynamic stability of the states with a fixed relative phase between the condensates has yet to be analyzed.

In this work, the thermodynamically stable state with spontaneous Josephson oscillations is obtained for two resonant condensates. This state is formed as a results of the competition between the inter-condensate interactions, one of which depends on the relative phase and the other is of the "density–density" type.

2. Let us consider two condensates in different internal states though in the same trap. Experimentally, this may be a mixture of two ^{87}Rb condensates in the $|F = 2, m_F = 2\rangle$ and $|F = 1, m_F = -1\rangle$ states. Since the spatial region of overlap between the condensates can be controlled experimentally [3], only a uniform overlap is considered below for simplicity. As is known [3, 5], a weak driving field can be used in the overlap region to create a certain relative initial phase for the condensates. In this work, a mechanism of transition of a mixture of resonant condensates with a given initial phase to the thermodynamically stable state in the presence of

only internal (i.e., independent of the external fields) interactions is described.

The proposed mechanism is also operative for the condensates in an asymmetric double-well potential formed by two different traps with a barrier between them. The barrier is created by the laser light, and its height is directly proportional to the laser power and, thus, can be varied with ease [2]. In particular, for a very high barrier (mutually independent condensates), the condensates can be created with their own initial phases or, what is the same, in different coherent states in each of the traps. After removal of the barrier, the condensates start to overlap, and one again arrives at the problem of possible ground state of a mixture of condensates with a given initial relative phase. In this work, the two-mode model is used, with the noninteracting condensates each being described by the "zero-mode" model. The Hamiltonian of the system has the form

$$\hat{H}_0 = \sum_{i=1,2} \hat{H}_i = \sum_{i=1,2} \left[\mu_{0i} \hat{a}_i^+ \hat{a}_i + \frac{1}{2} \lambda_i \hat{a}_i^+ \hat{a}_i^+ \hat{a}_i \hat{a}_i \right], \quad (1)$$

where $\hat{a}_i^+$ and $\hat{a}_i$ are, respectively, the creation and annihilation operators for the atoms of the condensate mode, while the constants λ_i of intracondensate interaction are scaled to the volume of condensate mode: $\lambda_i = U_0/V_{\text{eff}}$. As is well known, the coherent state $\hat{a}_i |\Psi_i\rangle = a_i |\Psi_i\rangle$, where a_i are complex numbers, minimizes the mean energy $\langle \Psi_i | \hat{H}_i | \Psi_i \rangle$ with $|a_i| = (n_i - 1/2)^{1/2} \approx n_i^{1/2}$. Hence, the wave functions of the condensate modes can be written as $\Psi_i = n_i^{1/2} \exp(i\theta_i)$. A uniform wave function describes the condensate states in a trap either with vertical wells or with parameters slowly varying at interatomic length scale, when the condensate wave

functions are independent of coordinates. The energies of both condensates are independent of their phases and are given by the expressions $\varepsilon_i(n_i) = \mu_{0i}n_i + \frac{1}{2}\lambda_i n_i^2$. In the equilibrium state with $d\varepsilon_i/dn_i = 0$, the "chemical potential" $\mu_{0i} < 0$ specifies the mean particle (occupation) numbers $n_i = \langle \hat{a}_i^+ \hat{a}_i \rangle \gg 1$ for the condensates; i.e., for a given μ_{0i} value one has $n_{0i} = |\mu_{0i}|/\lambda_i$ and $\varepsilon_{0i} = -|\mu_{0i}|^2/2\lambda_i$ in the equilibrium state. In the general case considered below, $d\varepsilon_i/dn_i \neq 0$. The total Hamiltonian of a mixture of interacting condensates is $H = H_0 + H_{int}$, where $H_0(n_1, n_2) = \varepsilon_1(n_1) + \varepsilon_2(n_2)$; with the canonically conjugate "action–angle" variables, the interaction of n_i and θ_i can generally be written as

$$H_{int} \equiv g(n_1, n_2; \theta_1, \theta_2)$$
$$= \sum_{l_1 l_2 \geq 0} [g_{l_1 l_2}(n_1, n_2)e^{i(l_1\theta_1 - l_2\theta_2)} + \text{h.c.}], \quad (2)$$

where l_1 and l_2 are integers describing a change in the number of particles upon switching on the interaction between the condensates. Phase-dependent intercondensate interactions (2) are primarily due to the nonorthogonality of the coherent states. The resonance condition

$$l_{1r}\frac{d\varepsilon_1}{dn_1} - l_{2r}\frac{d\varepsilon_2}{dn_2} = 0, \quad (3)$$

where the pair of numbers l_{1r} and l_{2r} specifies the resonance type, depends on the particle numbers and should be self-consistently taken into account when determining the state of a nonlinear system. In this respect, two key factors should be kept in mind. First, the resonance condition determines the phase $\phi_r = l_{1r}\theta_1 - l_{2r}\theta_2$, which varies anomalously slowly with time, because it is an approximate integral of motion in the absence of particle number fluctuations: $d\phi_r/dt \approx l_1 d\varepsilon_1/dn_1 - l_2 d\varepsilon_2/dn_2 \approx 0$, so that $\phi_r^{(0)} \approx \text{const} \neq 0$. Second, due to this relationship, the term with phase $\phi_r(t)$ can be set off in sum (2). All remaining terms in this sum are rapidly oscillating perturbations and will be disregarded in this work. Thus, for each type of resonance, a certain type of phase-dependent intercondensate interaction is specified (it will be called Josephson interaction for brevity). If the interaction is independent of time, the difference between the occupation numbers n_1 and n_2 monotonically increases with time, as follows from the equations of motion; i.e., dynamic instability takes place. This instability corresponds to the internal Josephson effect and is "removed" by the coherent density oscillations between the condensates. It should be emphasized that the instability arises only if the initial relative phase $\phi_r^{(0)}$ is nonzero. Contrary to the well-known Josephson

effect, e.g., in superconductors, the Josephson interaction in the case at hand depends on a macroscopic number of particles, so that both values are determined self-consistently from the condition for minimum of the thermodynamic functions. It is this circumstance that is responsible for the appearance of a new ground state.

If the total number of particles $n_0 = n_1 + n_2$ is conserved ($dn_0/dt = 0$), the resonant condensate populations n_{1m} and $n_{2m} = n_0 - n_{1m}$ are found from Eq. (3). Let us consider the state with particle number fluctuations in the region of a simple resonance: $l_{1r} = l_{2r} = 1$ and $\phi_r = \theta_1 - \theta_2$. In this case, the leading term in Eq. (2) has the form

$$g_1(n_{1m}; n_{2m}; \phi_r)$$
$$= g_1 n_{1m}^{1/2} n_{2m}^{1/2} \cos(\theta_1 - \theta_2) \equiv g_{1m}\cos(\theta_1 - \theta_2) \quad (4)$$

and corresponds to the uniform overlap of condensates. Using the fact that the Hamiltonian H_0 of noninteracting condensates is a function of a single dynamic variable, e.g., n_1, it is straightforward to write the Hamiltonian near the resonance to the first nonvanishing order in particle number fluctuations:

$$H_m = H_{0m} + \lambda(\Delta n_1)^2 + g_{1m}\cos\phi_r,$$
$$\lambda = \left(\frac{d^2 H_0(n_0; n_1)}{dn_1^2}\right)_m = \lambda_1 + \lambda_2. \quad (5)$$

Here, $H_{0m} \equiv H_0(n_{1m}, n_{2m})$, $(\Delta n_1) = n_1 - n_{1m}$, and $(\Delta n_2) = -(\Delta n_1)$. In what follows, the notation $(\Delta n_1) \equiv (\Delta n)$ is used. The expansion in (Δn) in Eq. (5) is written on the assumption that the width of the near-resonance region (determined by the particle number fluctuations) is large at the characteristic interaction variation scale. In other words, Hamiltonian (5) and the "resonance" solution obtained below are valid if the following conditions are fulfilled for each n_0:

$$(\Delta n)_{max} \ll n_{1m}, n_{2m},$$
$$\lambda(\Delta n)_{max} \gg (dg(n_0; n_1)/dn_1)_m, \quad (6)$$

where $(\Delta n)_{max}$ is the maximum possible change in the number of particles near the resonance. This quantity will be calculated below. Due to the second inequality, terms with the derivatives of interaction are absent in Eq. (5). Writing the terms linear in (Δn) in $d\phi_r/dt$, with allowance made for conditions (6), one finds that the ϕ_r and (Δn) variables are canonically conjugate. The change in the number of particles near the minimum is also a macroscopic variable, $(\Delta n) \gg 1$. This follows from the fact that the energy changes only slightly upon changing the number n_{im} of particles by $l_{ir} \ll n_{im}$: $H_{0m}(n_0; n_{1m} + l_{1r}) - H_{0m}(n_0; n_{1m}) \sim l_{1r}^2\lambda$, whereas g_{1m} is a macroscopic quantity. Because of this, the interaction

leads to the reconstruction of a large number of states, $(\Delta n) \sim (g_{1m}/l_{1r}^2 \lambda)^{1/2} \gg 1$. This allows the use of a quasiclassical approximation for determining quantum states of the system governed by Hamiltonian (5).

The resonance corresponds to the minimum of function H_0 at $\lambda > 0$; only in this case can it make the main contribution to the partition function and thermodynamic functions. In the quantum regime, the region of finite motion of Hamiltonian (5) [where the phase changes within $-\arccos(\varepsilon/g_{1m}) < \phi_r < \arccos(\varepsilon/g_{1m})$ for every $\varepsilon \equiv H_m - H_{0m}$] corresponds to the discrete quasiclassical spectrum of particle number fluctuations near the minimum of function $H_0(n_0; n_1)$ at n_{1m}. The states of this spectrum represent the quantum analogue of Josephson oscillations. Substituting $(\Delta n) \longrightarrow -i\partial/\partial\phi_r$, one finds that the Schrödinger equation for Hamiltonian (5) takes the form of Mathieu's equation. As known, the eigenvalues of Mathieu's equation form a continuous spectrum at $\varepsilon > g_{1m}$ and allowed narrow bands at $-g_{1m} < \varepsilon < g_{1m}$. Neglecting the corresponding bandwidths, one may speak about the discrete spectra in the wells. Since the number of states in the well is large, the number of the discrete level is determined by the Bohr–Sommerfeld quantization rule

$$\nu(\varepsilon) = \oint \frac{d\phi_r}{\pi} \left[\frac{2}{\lambda}(\varepsilon - g_{1m}\cos\phi_r) \right]^{1/2}$$
$$= n_c[E(\kappa) - (1 - \kappa^2)K(\kappa)]; \tag{7}$$

accordingly, the density of states $\rho_d(\varepsilon)$ in the discrete spectrum is

$$\rho_d(\varepsilon) = \frac{1}{2\pi}\frac{d(\nu)}{d\varepsilon} = \frac{2^{1/2}K(\kappa)}{\pi^2\omega_m}; \quad n_c = \frac{8}{\pi}\left(\frac{g_{1m}}{\lambda}\right)^{1/2};$$
$$\kappa^2 = \frac{\varepsilon + g_{1m}}{2g_{1m}} \equiv \sin^2\frac{\phi_r^{(0)}}{2}, \tag{8}$$

where $K(\kappa)$ and $E(\kappa)$ are the complete elliptic integrals of the first and second kind, respectively. The maximum number of levels in the well is $n_c \equiv (\Delta n)_{max} \gg 1$. In the continuous spectrum, $\nu(\varepsilon)$ and the density of states ρ_c are

$$\nu(\varepsilon) = \frac{4}{\pi^2}\left(\frac{g_{1m}}{2\lambda}\right)^{1/2} E(\kappa^{-1});$$
$$\rho_c(\varepsilon) = \frac{\kappa^{-1}K(\kappa^{-1})}{2^{1/2}\pi^2\omega_m}. \tag{9}$$

The quantity $\omega_m = (\lambda g_{1m})^{1/2} \ll g_{1m}$ has a meaning of the maximum level spacing in the discrete spectrum. It follows from these expressions that the density of states has a logarithmic singularity at the edges of continuous

and discrete spectra: $\rho_{d,c}(\varepsilon) \sim \omega_m^{-1}\ln|1 - \varepsilon/g_{1m}|^{-1}, \varepsilon \longrightarrow g_{1m}$. This corresponds to an infinite period of coherent oscillations, i.e., to the loss of phase coherence. All the quantities depend parametrically on the total number n_0 of particles. This parameter can be determined from the conditions for the minimum of the thermodynamic potential.

3. Let us now determine the conditions for and the character of instability toward the transition to the current state upon changing the number of particles or the chemical potential of the mixture. With the known density of states (8) and (9), one obtains the following expressions for the thermodynamic potential in the discrete and continuous regions [ε in Eqs. (8) and (9) should be replaced by μ, with μ being measured from H_{0m}]:

$$\Omega(\mu) = -4E_c[(4\kappa^2 - 2)E(\kappa)$$
$$+ (3\kappa^2 - 2)(\kappa^2 - 1)K(\kappa)]; \quad -g_{1m} < \mu < g_{1m}; \tag{10}$$

$$\Omega(\mu) = -4E_c\kappa^3[(4 - 2\kappa^{-2})E(\kappa^{-1})$$
$$- (\kappa^{-2} - 1)K(\kappa^{-1})]; \quad \mu > g_{1m}. \tag{11}$$

In both cases,

$$\left(\frac{\partial\Omega}{\partial g_{1m}}\right)_\mu = \frac{(3/2)\Omega + \mu N}{g_{1m}}; \quad E_c = \frac{g_{1m}}{9}\frac{n_c}{2\pi}. \tag{12}$$

According to the definition given in Eq. (8), the chemical potential and g_{1m} depend on the initial relative phase. The g_{1m} value determines the amplitude and frequency of Josephson oscillations [see Eqs. (7) and (8)]. At the same time, it monotonically depends on n_0, so that the behavior of the derivative $\partial\Omega/\partial g_{1m}$ completely determines the behavior of the system upon changing the population n_0. It follows from Eqs. (10)–(12) that $\Omega < 0$ over the entire range of g_{1m} from 0 to ∞, so that the thermodynamic potential Ω monotonically decreases with increasing g_{1m}; i.e.,

$$\left(\frac{\partial\Omega}{\partial g_{1m}}\right)_\mu < 0. \tag{13}$$

Thus, the system is thermodynamically unstable toward the growth of Josephson oscillations. The increase in g_{1m} is equivalent to the increase in either the total population n_0 or the intercomponent scattering length. To determine the equilibrium $\bar{g}_{1m}$ value, account must be taken of the phase-independent repulsive interaction between the condensates [i.e., the term with $l_1, l_2 = 0$ in Eq. (2)]: $g_{0m}(n_1, n_2) = g_0 n_{1m}(n_0 - n_{1m}) \sim \alpha g_{1m}^2$, where $\alpha \sim 1/|\mu_{02} - \mu_{01}|$. This interaction characterizes the "rigidity" of the system against the increase
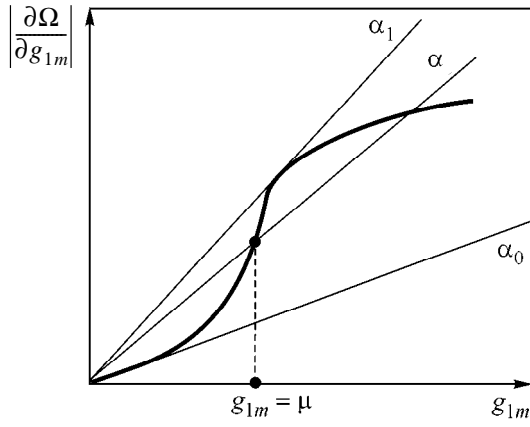
Figure.

in g_{1m}. With allowance made for this interaction, the Landau functional can be written as

$$F = \Omega(\mu, g_{1m}) + \alpha g_{1m}^2. \tag{14}$$

The equilibrium $\bar{g}_{1m}$ values are found from the condition for the minimum of this functional; i.e., they are solutions of the equation

$$\left|\frac{\partial\Omega}{\partial g_{1m}}\right|_{g_{1m} = \bar{g}_{1m}} = \alpha\bar{g}_{1m}. \tag{15}$$

The nonzero equilibrium $\bar{g}_{1m}$ value defines the total number of particles $\bar{n}_0$ for which spontaneous Josephson oscillations occur in the system. In other words, the system has the current ground state; namely, for the chemical potential coinciding with the energy of one of the discrete levels (7), the equilibrium value of the maximum Josephson current is

$$\left|\bar{j}_{\max}^{(\nu)}\right| = \frac{d(\bar{\Delta}n)}{dt} = \bar{g}_{1m}\sin\frac{\bar{\mu}_\nu}{\bar{g}_{1m}}. \tag{16}$$

In turn, $\bar{g}_{1m} = 0$ in the ground state implies that the mixture of condensates is thermodynamically unstable in the presence of Josephson interaction. This state corresponds to the nonzero population of one of the mixture components and, correspondingly, to the absence of the Josephson current. In this case, short-lived dynamic oscillations are only possible for an arbitrary (i.e., different from equilibrium) number of particles.

The qualitative behavior of the derivative $|\partial\Omega/\partial g_{1m}|$ is illustrated in the figure. The domains of g_{1m} values to the right and left of the $g_{1m} = \mu$ point correspond to the discrete and continuous spectra, respectively. In this figure, $|\partial\Omega/\partial g_{1m}| \sim g_{1m}/(\mu\lambda)^{1/2}$ at $\mu \gg g_{1m}$, $|\partial\Omega/\partial g_{1m}| \sim (g_{1m}/2\lambda)^{1/2}$ at $\mu \ll g_{1m}$, and $|\partial^2\Omega/\partial g_{1m}^2| \sim \ln|g_{1m} - \mu|^{-1}$ as

$|\mu - g_{1m}| \longrightarrow 0$. The tangent to the $\partial\Omega/\partial g_{1m}$ curve at the zero point is $\alpha_0 = \frac{1}{\pi}(\mu\lambda)^{-1/2}$. Graphical solution of Eq. (15) (see figure) yields the following results. At $\mu > 0$ and $\alpha < \alpha_0$, the state with $\bar{g}_{1m} = 0$ is absolutely unstable; in the ground state of the system, $\bar{g}_{1m} \neq 0$. At $\alpha_0 < \alpha < \alpha_c$ ($\alpha_c \approx 1.14\alpha_0$), the state with $\bar{g}_{1m} = 0$ becomes metastable; the system still has the current ground state. At $\alpha_c < \alpha < \alpha_1$, where $\alpha_1 \approx 1.25\alpha_0$, the state with $\bar{g}_{1m} \neq 0$ becomes metastable. Finally, at $\alpha > \alpha_1$, Eq. (15) has no solutions with $\bar{g}_{1m} \neq 0$. Note that the states with $\bar{g}_{1m} \neq 0$ and $\bar{g}_{1m} = 0$ correspond to discrete and continuous spectra, respectively. It follows from the definition of α_0 that the stronger the intracondensate interaction λ, the narrower the domain of existence of the current state. Using Eq. (8), one can readily show that the chemical potential $\mu > 0$ decreases with an increase in the initial phase $\phi_r^{(0)}$; hence, the domain of existence of the current state becomes more extended.

At $\mu < 0$, the condensate in the region of discrete levels exists regardless of the α value. One can readily show that the $\mu = 0$ value defines the most unstable state corresponding to the number of particles $n_{0c} = 0.2n_c$. At the same time, if the total number of particles decreases at a fixed α value, the transition to the current state proceeds jumpwise at $\mu = \mu_c = \alpha^2/\lambda$.

The competition between the Josephson interaction $g_1(n_1, n_2)$ and the density–density-type interaction $g_0(n_1, n_2)$ gives rise to the current ground state and plays in the resonance region the role similar to the role the competition between the tunneling and intracondensate interaction plays for the dynamic nonresonance solutions [4, 7]. The transition considered in Section 1 for the dynamic solutions corresponds to the transition in the resonance region from the current ground state to the state in which the mixture of condensates with Josephson interaction is thermodynamically unstable because $\bar{g}_{1m} = 0$. Note also that, inasmuch as Hamiltonian (5) describes the oscillations with amplitudes much smaller than the resonance populations [the first inequality in Eq. (6)], the resonance region, by definition, corresponds to the strongly nonlinear regime.

It is worth noting that the resonance region defined by Eqs. (3) and (6) was not considered in [4, 7]. However, one can easily show that conditions (6) for applicability of the resonance solution are identically fulfilled for the same condensates. Therefore, the solutions obtained in [4] for the identical condensates without regard for the resonance condition are, at least, thermodynamically unstable. The fact that the resonance condition defines the populations of the mixture components was not taken into account in [5]. For this reason, the dynamic solution found in [5] is likely invalid.

For the resonances with l_{1r}, $l_{2r} \neq 1$, the relevant expressions differ from the above formulas by numerical multipliers compiled of l_{1r} and l_{2r}. As the number of particles in the mixture increases, the main contribution to the thermodynamic functions may come from resonances of increasingly high order, because $g_{l_1 l_2}(n_1, n_2) \sim n_1^{l_{1r}/2} n_2^{l_{2r}/2}$ in Eq. (2). The corresponding characteristic frequency ω_m of Josephson oscillations increases as l_{ir}, and, simultaneously, the widths of resonance regions increase as $\sim\lambda(\Delta n)_{\max} \sim \omega_m$. If the resonance regions start to overlap at a certain critical number of particles, the phase coherence breaks and a stochastic regime prevails with randomly varying phase.

REFERENCES

1. C. J. Myatt, E. A. Burt, R. W. Christ, *et al.*, Phys. Rev. Lett. **78**, 586 (1997).

2. A. Rohrl, M. Naraschewski, A. Schenzle, and H. Wallis, Phys. Rev. Lett. **78**, 4143 (1997).

3. D. S. Hall, M. R. Mattews, C. E. Wieman, and E. A. Cornell, Phys. Rev. Lett. **81**, 1543 (1998).

4. S. Raghavan, A. Smerzi, S. Fantoni, and V. B. Shenoy, Phys. Rev. A **59**, 620 (1999).

5. J. Williams, R. Walser, J. Cooper, *et al.*, Phys. Rev. A **59**, R31 (1999).

6. M. R. Andrews, C. G. Townsend, H.-J. Meisner, *et al.*, Science **275**, 637 (1997).

7. G. J. Milburn, J. Corney, E. M. Wright, and D. F. Walls, Phys. Rev. A **55**, 4318 (1997).

8. H.-J. Meisner, D. M. Stamper-Korn, J. Stengler, *et al.*, Phys. Rev. Lett. **82**, 2228 (1999).

Translated by V. Sakun

Magnetic Field Effects on the Nonohmic Impurity Conduction of Uncompensated Crystalline Silicon

A. P. Mel'nikov*, Yu. A. Gurvich*, L. N. Shestakov**, and E. M. Gershenzon*

* Moscow State Pedagogical University, Malaya Pirogovskaya ul. 1, Moscow, 119891 Russia
e-mail: melnikov@rpl.mpgu.msk.su
** Seaside State University, Arkhangel'sk, 163006 Russia
Received December 6, 2000; in final form, December 18, 2000

The impurity conduction of a series of crystalline silicon samples with the concentration of major impurity $N \approx 3 \times 10^{16}$ cm^{-3} and with a varied, but very small, compensation K was measured as a function of the electric field E in various magnetic fields $H - \sigma(H, E)$. It was found that, at $K < 10^{-3}$ and in moderate E, where these samples are characterized by a negative nonohmicity ($d\sigma(0, E)/dE < 0$), the ratio $\sigma(H, E)/\sigma(0, E) > 1$ (negative magnetoresistance). With increasing E, these inequalities are simultaneously reversed (positive nonohmicity and positive magnetoresistance). It is suggested that both negative and positive nonohmicities are due to electron transitions in electric fields from impurity ground states to states in the Mott–Hubbard gap. © *2001 MAIK "Nauka/Interperiodica".*

PACS numbers: 72.20.My; 72.80.Cw

1. It is commonly known that the conduction of doped semiconductors at low temperatures (T) and a small compensation (K) is due to the hopping motion of carriers (vacancies in n-type semiconductors at $K \ll 1$) over ground states of impurity atoms (σ_3 conduction). A theory of σ_3 conduction has been developed that provides a quantitative description of the phenomenon at $K \longrightarrow 0$ (see, for example, [1]). In fact, relationships predicted by this theory are observed only at $K > 10^{-3}$. Significant discrepancies exist between the theory and experiment at lower K. Our investigations of such materials revealed a number of new effects. For example, contrary to theoretical predictions [1], the activation energy for hopping conduction (ε_3) in the ohmic region significantly increases with decreasing K ($K < 10^{-3}$). With increasing N at $K = $ const, ε_3 grows weaker [2] than is predicted by the theory.

These discrepancies are explained by the existence of impurity molecules (D_2^0) whose single-ionization energy is lower than the ionization energy of an isolated impurity. As a consequence, an additional peak of density of states appears in the lower Hubbard impurity band with an energy of ≈ 3 meV relative to the ground state [2]. We believe that the existence of states in the Mott–Hubbard gap is another reason (essential mainly in the nonohmic region) for the discrepancies [4].

This article describes the first results of studying the magnetic field effects on the impurity conduction in the nonohmic region ($E > E_1$).

2. Figure 1 displays the $\sigma(E)$ curves at $T = 8$ K for Si : B samples with $N = $ const $= 3.6 \times 10^{16}$ cm^{-3} and different concentrations NK of the compensating impurity.

Samples *3–8* were obtained from the same cut of an ingot with $NK = 8 \times 10^{12}$ cm^{-3}; changes in NK were accomplished by transmutation doping. It is evident that, as E increases, the ohmic region ($E < E_1$) for the samples with small K is followed by a portion of a drop in σ (negative nonohmicity), which is succeeded by a rise in σ at $E > E_2$. The value of E_2 increases with increasing K. As E further increases ($E > E_3$), the $\sigma(E)$ dependence becomes stronger.

As an example, Fig. 2 demonstrates distinctions between $\sigma(E)$ curves at $H = 0$ (dot-and-dash line) and $H = 2$ T for samples *4* and *6*. It is seen that the magnetic field at $E > E_1$ increases the conductivity and shifts the point E_1 toward higher E. At $E > E_2$, the greater σ, the stronger the decrease in conductivity in magnetic field H.

Figure 3 demonstrates the dependence of the σ_H/σ_0 ratio on E at $H = 2$ T. In the ohmic region, $\sigma_H/\sigma_0 = 1$; at $E_2 < E < E_1$, the conductivity increases by a factor of 2–2.5 and the magnetoresistance (MR) is negative. At $E > E_2$, the magnetoresistance is positive and increases with E. At $E > E_3$, the positive magnetoresistance increases even more strongly.

Figure 4 demonstrates the dependence of the current on E for sample *6* at $T = 8$ K and H (T) = (*1*) 0, (*2*) 1, (*3*) 1.5, and (*4*) 2. It is clear that the magnetic field shifts the point E_1 toward higher E: for this series of samples, $E_1 = E_1^0(1 + \beta H^2)$, where $\beta \approx 0.34$ T^{-2} and slightly varies with T. At $E_1 < E < E_2$, the current hardly increases with increasing E. Oscillations of the σ_3 conductivity with time are observed in the $j(E)$ saturation region [3].

This region is shown in Fig. 4 by the dotted line. The magnetic field effect on the oscillation amplitude and period will be considered separately.

3. Let us discuss the results obtained. A large negative magnetoresistance is observed in the region $E_1 < E < E_2$. On the other hand, a positive magnetoresistance is observed at $E > E_2$. The observation of the negative magnetoresistance in the region of negative nonohmicity and the sign reversal of the magnetoresistance together with the sign reversal of the nonohmicity is the main result of this work. We emphasize that the magnetic fields in which these effects are observed are weak in the sense that these magnetic fields do not affect the radius of an isolated impurity center.

Let us first consider the region $E > E_2$. We have demonstrated previously that the conduction at $E > E_2$ is due to the electron motion over states lying 10–15 meV below the free band bottom [4] (30–35 meV higher than the impurity ground state; the consideration relates to an n-type material). We called this region of fields the region of high-temperature variable range hopping conduction (σ_M) [5]. Similar to the conventional Mott conduction [1], σ_M is characterized by the dependence $\sigma_M \sim \exp(-(T/T_0)^{0.25})$ and increases with E as $\sigma_M \sim \exp(\alpha E)$.

In order to explain these results, we proposed a model of a long tail of states extending in energy down to the Fermi level in the upper Hubbard impurity band [6]. Electrons in an electric field hop over these states (both activationless and with phonon absorption), traveling up in energy. The hopping distance is variable. It decreases with increasing E and electron energy ε (it is assumed that the density of states in the tail increases with ε). Eventually, electrons reach a certain "transport" level $\varepsilon = \varepsilon_{tr}$ whose position is determined by equal probabilities of hopping up and down in energy. Hopping over the ε_{tr} level determines the conductivity in this region of fields. The energy ε_{tr} grows with increasing E [7]. Simultaneously, the number of electrons in the vicinity of the ε_{tr} level increases.

The ε_{tr} level concept readily explains the evolution of conductivity with increasing concentration of the compensating impurity NK at $H = 0$ (Fig. 1) in the region of positive nonohmicity. The rise of the electron concentration in the vicinity of the ε_{tr} level is limited by the recombination process. The corresponding lifetime $\tau \sim (NK)^{-1}$. The concentration drops with increasing NK: $n(\varepsilon_{tr}) \sim (NK)^{-1}$. The greater NK, the lower, generally, the position of the ε_{tr} level at a given E. This leads to the additional dependence $\sigma(NK)$. If a vertical section of curves in Fig. 1 is mentally drawn in the region of positive nonohmicity, it can be verified that $\sigma(E = \text{const}) \sim (NK)^{-\alpha}$, where $\alpha > 1$. At the same time, the field in which a given value of σ is attained must increase with increasing (NK). This is directly seen in Fig. 1.

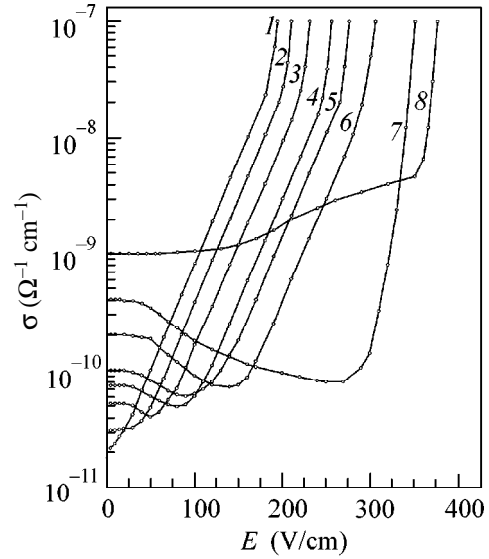As NK increases, recombination is enhanced, electrons have no time to attain the states with high mobil-

Fig. 1. Curves $\sigma(E)$ at $T = 8$ K for a series of samples with $N = 3.6 \times 10^{16}$ cm^{-3} and various NK (10^{12} cm^{-3}): (*1*) 3, (*2*) 5, (*3*) 8, (*4*) 15, (*5*) 20, (*6*) 30, (*7*) 60, and (*8*) 150.
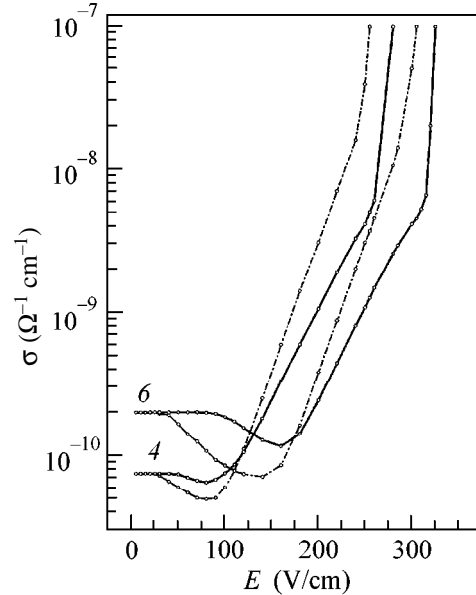

Fig. 2. Curves $\sigma(E)$ for samples *4* and *6* at $H = 0$ (dot-and-dash line) and $H = 2$ T.

ity, and σ_M is not observed at all (Fig. 1, curve *7*). Conduction via the band of states with $E > 35$ meV appears at $E > E_3$, when a band of delocalized states is formed below the increasing band bottom [4, 8, 9].

At higher NK, when the recombination probability becomes higher than the probability of electron transition from the states in the vicinity of the Fermi level to the states in the Mott–Hubbard gap, not only σ_M disappears but the negative nonohmicity disappears as well:
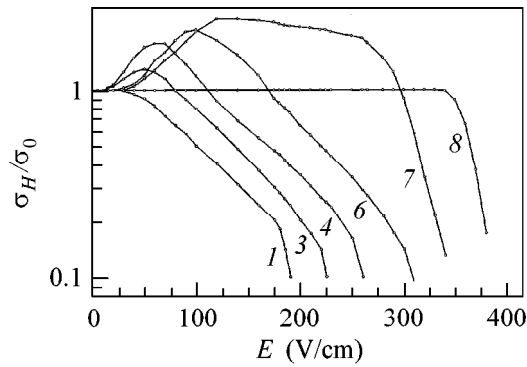
Fig. 3. Curves $\sigma_H/\sigma_0(E)$ at $T = 8$ K and $H = 2$ T for samples *1*, *3*, *4*, *6*, *7*, and *8*.
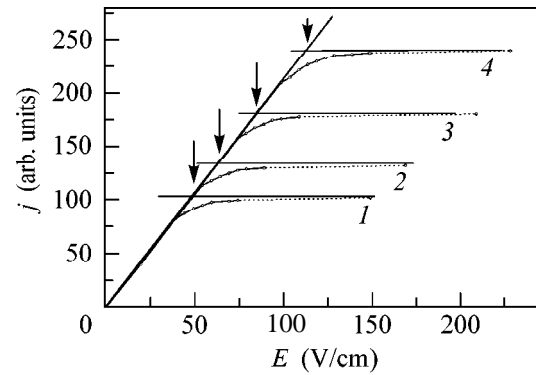
Fig. 4. Current vs. *E* for sample *6* at $T = 8$ K and *H* (T): (*1*) 0, (*2*) 1, (*3*) 1.5, and (*4*) 2. Arrows mark changes in E_1 with *H*.

σ_3 grows with *E* as predicted by the theory (Fig. 1, curve *8*), and $\sigma_H/\sigma_0 = 1$ (see Fig. 3, curve *8*).

Figures 2 and 3 demonstrate that the positive magnetoresistance increases with increasing σ_M. Note that ε_{tr} and, hence, the electron localization radius $a(\varepsilon)$ increase with increasing *E*. The larger $a(\varepsilon)$, the stronger the effect of *H* on the overlap of states (all other factors being equal). In addition, we cannot exclude the decrease in the density of states in the vicinity of ε_{tr} with increasing *H* [10].

Let now consider the region $E < E_2$. At $E < E_2$, conduction occurs via the states of the main impurity band. As it must, $\sigma_3 \sim NK$ in the ohmic region at high temperatures. With increasing *E*, σ_3 drops. To account for the drop in σ_3 conductivity with decreasing *E* [3], the model of "dead ends" was proposed. According to this model, vacancies move mainly in the direction of the field and arrive at the ends of chains of impurity centers, around which the concentration of impurities is small. Vacancies are localized, and the number of moving vacancies is reduced. We believe that the effect must be significant at small *N* and *K* (*KN* < the number of "dead ends") at temperatures close to the depletion of σ_3 conduction. At low *T*, the decrease in the activation energy with *E* (Frenkel–Pool effect) in the region of an exponential growth of the conductivity affects σ_3 more strongly, and σ_3 grows with *E*.

Note two points. In our experiments (small *N* and very small *K*), a drop in σ_3 with *E* is also observed in the region of an exponential growth of σ_3, down to the lowest *T*. Small magnetic fields do not affect the conductivity in the ohmic region. However, small *H* shift E_1 toward large *E* significantly (up to 2–2.5 times).

We failed to explain the occurrence of a negative magnetoresistance in the region of negative nonohmicity within the model of "dead ends." A negative magnetoresistance may occur in the case of variable range hopping conduction because of the effect of *H* on interference processes. This effect is significant in two-dimensional structures. A negative magnetoresistance may also arise from a decrease in the density of states at *H* in the case when the Fermi level lies in the region of an abrupt drop in the density of states with decreasing energy (see [10] and references therein). Both these mechanisms are irrelevant to our situation: three-dimensional structure, nearest-neighbor hopping (σ_3 conductivity), and Fermi level lying in the region of a smoothly descending tail of the lower Hubbard impurity band.

We observed previously a large negative magnetoresistance in more heavily doped and more compensated samples [11]. In that work, we explained the negative magnetoresistance by the presence of D_2^0 molecules (see the beginning of the article), which are traps for vacancies. With an increase in *H*, these traps are destroyed, the vacancy concentration in the main peak of the lower Hubbard impurity band increases, and the conductivity increases as well. This effect must also be observed in the ohmic region. This is not confirmed by experiments. Apparently, the molecules decay at large *H*, and our results are due to a different process.

We believe that the drop in σ_3 with decreasing *E* cannot be explained if the consideration is restricted to only the ground impurity states. The strong effect of *H* on σ_3 and σ_M suggests that the drop in σ_3 with decreasing *E* is also associated with the electron transition from the states in the vicinity of the Fermi level to the states in the Mott–Hubbard gap. At $E < E_2$, electrons do not reach states with high mobility, and their contribution to the conductivity is not conspicuous: $\sigma_M < \sigma_3$. The moving vacancies are attracted by immobile nonequilibrium electrons and recombine on them. The number of free vacancies is reduced. Electrons must be activated to states in the vicinity of the Fermi level to generate free vacancies. A magnetic field decreases the localization radius of electrons and, correspondingly, the probability of electron transition to vacancies. We

relate the shift of E_1 toward large E and the increase in σ_3 with increasing H to this phenomenon.

REFERENCES

1. B. I. Shklovskiĭ and A. L. Éfros, *Electronic Properties of Doped Semiconductors* (Nauka, Moscow, 1979; Springer-Verlag, New York, 1984).
2. A. P. Mel'nikov, Yu. A. Gurvich, L. N. Shestakov, and E. M. Gershenzon, Pis'ma Zh. Éksp. Teor. Fiz. **71**, 28 (2000) [JETP Lett. **71**, 17 (2000)].
3. D. I. Aladashvili, Z. A. Adamiya, K. G. Lavdovskiĭ, and B. I. Shklovskiĭ, Pis'ma Zh. Éksp. Teor. Fiz. **47**, 390 (1988) [JETP Lett. **47**, 466 (1988)].
4. A. P. Mel'nikov, Yu. A. Gurvich, L. N. Shestakov, and E. M. Gershenzon, Pis'ma Zh. Éksp. Teor. Fiz. **66**, 240 (1997) [JETP Lett. **66**, 249 (1997)].
5. E. M. Gershenzon, Yu. A. Gurvich, A. P. Mel'nikov, and L. N. Shestakov, Pis'ma Zh. Éksp. Teor. Fiz. **51**, 204 (1990) [JETP Lett. **51**, 231 (1990)].
6. Yu. A. Gurvich, A. P. Mel'nikov, L. N. Shestakov, and E. M. Gershenzon, Pis'ma Zh. Éksp. Teor. Fiz. **60**, 845 (1994) [JETP Lett. **60**, 859 (1994)].
7. B. I. Shklovskii, E. I. Levin, H. Fritzshe, and S. D. Baranovskii, *Transport Correlation and Stuctural Defects*, Ed. by H. Fritzshe (World Scientific, Singapore, 1990), p. 161.
8. Yu. A. Gurvich, A. P. Mel'nikov, L. N. Shestakov, and E. M. Gershenzon, Pis'ma Zh. Éksp. Teor. Fiz. **61**, 717 (1995) [JETP Lett. **61**, 730 (1995)].
9. A. P. Mel'nikov, Yu. A. Gurvich, L. N. Shestakov, and E. M. Gershenzon, Pis'ma Zh. Éksp. Teor. Fiz. **63**, 89 (1996) [JETP Lett. **63**, 100 (1996)].
10. M. E. Raikh, Y. Cringon, Qiu-Yi Ye, *et al.*, Phys. Rev. B **45**, 6015 (1992).
11. E. M. Gershenzon, Yu. A. Gurvich, A. P. Mel'nikov, and L. N. Shestakov, Pis'ma Zh. Éksp. Teor. Fiz. **54**, 639 (1991) [JETP Lett. **54**, 646 (1991)].

Translated by A. Bagatur'yants

Giant Second Harmonic Generation in Microcavities Based on Porous Silicon Photonic Crystals

T. V. Dolgova[1], A. I. Maĭdikovskiĭ[1], M. G. Martem'yanov[1], G. Marovsky[2], G. Mattei[3], D. Schuhmacher[2], V. A. Yakovlev[4], A. A. Fedyanin[1], and O. A. Aktsipetrov[1],*

[1] *Moscow State University, Vorob'evy gory, Moscow, 119899 Russia*
* e-mail: aktsip@shg.phys.msu.su
[2] *Laser-Laboratorium Göttingen, D-37077 Göttingen, Germany*
[3] *Instituto di Metodologie Avanzate Inorganiche, CNR, Monterotondo Scalo 00016, Italy*
[4] *Institute of Spectroscopy, Russian Academy of Sciences, Troitsk, Moscow region, 142092 Russia*
Received November 28, 2000

The experimental spectral dependence of the intensity of the second harmonic (SH) generated in microcavities based on porous silicon photonic crystal demonstrates resonant intensity enhancement (by a factor of $\sim 2 \times 10^2$) in the vicinity of the cavity mode and at the edges of the photonic band gap. The enhancement is due to the combined effect of pump radiation localization inside the microcavity, multiple SH interference in the photonic crystal, and two-photon resonance of the porous silicon quadratic susceptibility at the SH frequency. © 2001 MAIK "Nauka/Interperiodica".

PACS numbers: 42.65.Ky; 42.70.Qs

Photonic crystals (PCs) are the microstructures with periodically modulated optical (including high-order) susceptibility with a period on the order of the optical wavelength. They possess unique physical properties and are of great practical interest. The presence of a photonic band gap, i.e., the range of optical frequencies where the electromagnetic field exponentially decays inside the PC, renders them candidates for use in optical switches and optical transistors [1], as well as in PC lasers with extremely low lasing threshold [2]. PCs exhibit unique optical effects such as giant optical dispersion [3], optical bistability [4], and light localization [5]. So far, most attention in studying the nonlinear optical properties of PCs has been given to efficient frequency doubling, because the conditions for quasi-phase-matching are fulfilled in PCs. Quasi-matching can be attained (1) in nonlinear PCs with quadratic susceptibility periodically modulated in one or two directions and uniform linear susceptibility [6] and (2) in PCs with modulated linear susceptibility [7, 8]. In the latter case, the quasi-matching condition can be fulfilled if either the pump frequency or the second harmonic (SH) frequency falls on the edge of the photonic band gap in the PC. Naturally, such PCs were fabricated from noncentrosymmetric materials with large bulk quadratic susceptibility: lithium niobate [6], gallium arsenide [7], and zinc sulfide [8]. Of particular interest is the investigation of the nonlinear optical response of a PC fabricated from centrosymmetric materials, e.g., porous silicon (PS) [9]. Porous silicon PCs are grown using a comparatively simple electrochemical technique that provides high reproducibility

of parameters. This method has become part of modern silicon technology, thereby resulting in the high practical importance of porous silicon PCs and microstructures on their base. It is of interest to explore the nonlocal effects in the nonlinear optical response of PC-based microcavities (MCs). The parameters of the distributed PC mirrors of such Fabry–Pérot microcavities determine the MC Q factor. This permits the control of the electromagnetic field localization in the MC at the frequency of the cavity mode, providing enhancement of the MC optical response, e.g., luminescence [10] and Raman scattering [11]. The MC mode within the photonic band gap is analogous to the impurity level within the semiconductor electronic energy gap. The spectral position of the cavity mode in the photonic band gap can be changed by varying the MC parameters [layer thicknesses in PC mirrors and the MC ("impurity") level], allowing the control of the enhancement effects in the nonlocal nonlinear MC optical response.

This work reports the experimental results on the intensity spectrum of the SH generated in porous silicon microcavities. The enhancement of the SH response was observed in the vicinity of the cavity mode and at the edges of the photonic band gap. The SH generation in a multilayer structure with distributed nonlinear sources is phenomenologically described with account taken of the multiple interference of the pump and SH fields. It is shown that the enhancement of SH response at the frequency of the MC mode differs in nature from the enhancement at the edges of the photonic band gap: the mode SH resonance is caused by the
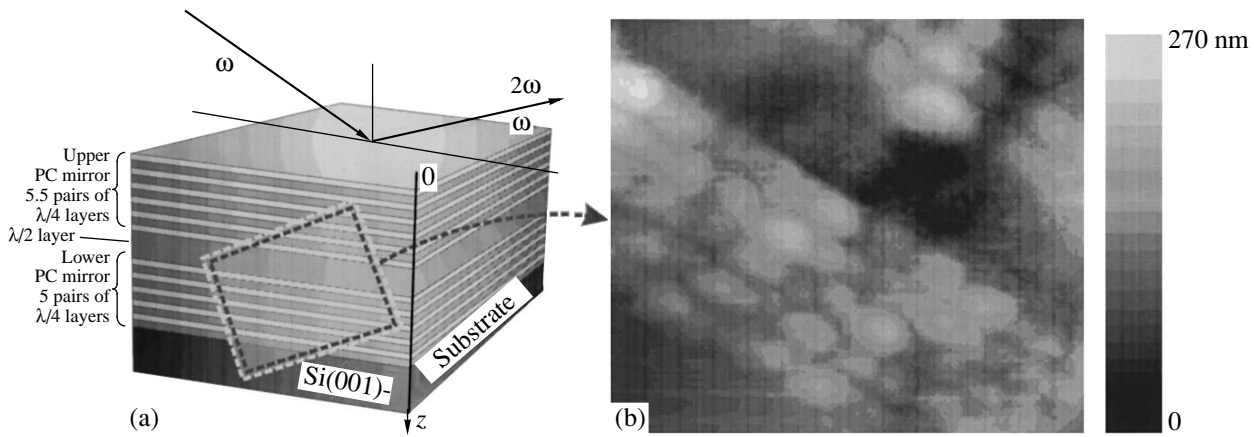
Fig. 1. Left: porous silicon MC structure and geometry of the experiment; light regions correspond to the optically denser PS layers. Right: MC cut image obtained on a scanning microscope with a quasi-friction detector. The gray scale of the displacement of the tip with respect to the MC cleavage face at a constant friction force is given on the right.

localization (amplification) of the standing pump wave in the vicinity of the MC layer, whereas the SH resonance at the edge of the photonic band gap is caused by a uniform amplification of the pump field in the distributed PC mirrors of the microcavity.

Microcavity samples (Fig. 1a) were composed of two one-dimensional PCs formed by five pairs of quarter-wave ($\lambda_0 = 945$ nm) PS layers and a half-wave PS cavity layer as a spacer. The samples were prepared by electrochemical etching [12] of a single-crystal p-type silicon wafer in the crystallographic (001) orientation with a resistivity of 0.01 Ω cm in an electrolyte consisting of a 50% solution of hydrofluoric acid and ethyl alcohol taken in 1 : 2 v/v ratio. The alternating PS layers of different porosity (air volume concentration) were obtained by periodic modulation of the current density flowing through the silicon wafer perpendicularly to its surface. The etching rate was determined by the current density of the electrochemical process and the resistivity of the silicon wafer. The porosities and thicknesses were, respectively, $f_h = 0.77$ and $d_h = 160$ nm for the optically denser PC layers and $f_l = 0.88$ and $d_l = 200$ nm for the less dense layers. The cavity layer was formed from PS with $f_r = 0.88$ and $d_r = 400$ nm. Figure 1b is the MC cut image obtained on a scanning force microscope with a piezoelectric quasi-friction force detector based on a 32.8-kHz quartz tuning-fork. The scanning tip was made from a single-mode fiber by etching in a protective envelope. Light areas in the image correspond to a high longitudinal friction, i.e., to the less porous regions. The strict periodicity in the PS layers and the 5-μm-scale longitudinal homogeneity of the structure confirm the high quality of the prepared samples. However, it was hard to determine the thickness ratio for the PS layers of different porosity because the scanning tip had a large radius (on the order of 50 nm) of curvature, resulting in an asymmetry toward the denser PS layers.

The SH spectra were recorded using a Spectra-Physics MOPO 710 optical parametric oscillator (OPO), tuned in the range 730–1100 nm, with a 10-ns pulse duration and pulse energy of approximately 10 mJ, excited by the third harmonic of a YAG laser. Collinear phase matching in the OPO nonlinear crystal provided a fixed angle of incidence θ for the pump radiation upon frequency tuning. The SH radiation from the MC sample was filtered and focused onto the photomultiplier cathode. To normalize the SH spectrum to the frequency-dependent photomultiplier sensitivity and filter transmission coefficients, a portion of the pump radiation was fed into the reference channel that was identical to the main channel and contained z-quartz crystal as a source of calibrating SH radiation. For linear spectroscopy, the pump radiation reflected from the MC sample was detected by a photodiode and normalized to the intensity of incident light.

For the p- and s-polarized pump radiations (p–p and s–p geometries, respectively), the intensity of the p-polarized SH radiation reflected from the MC was independent of the angle of rotation of the MC sample about its normal, to within the experimental error caused by a weak inhomogeneity of the MC in its plane.

The dependence of the SH intensity $I_{2\omega}$ on the pump wavelength λ_ω, measured for the angle of incidence θ = 45° in the s–p geometry, is shown in Fig. 2a. For comparison, the spectrum of the linear reflection coefficient (R_s) of the s-polarized pump radiation is presented in Fig. 2d. In the vicinity of 780 nm, corresponding to the spectral position of the MC mode, $I_{2\omega}$ increases by a factor of $\sim 2 \times 10^2$, as compared to the SH intensity in the band gap. Another resonance feature is observed in the vicinity of 910 nm (~50-fold enhancement), which coincides with the long-wavelength edge of the photonic band gap. The increase in the SH intensity at the short wavelength edge of the photonic band gap is much
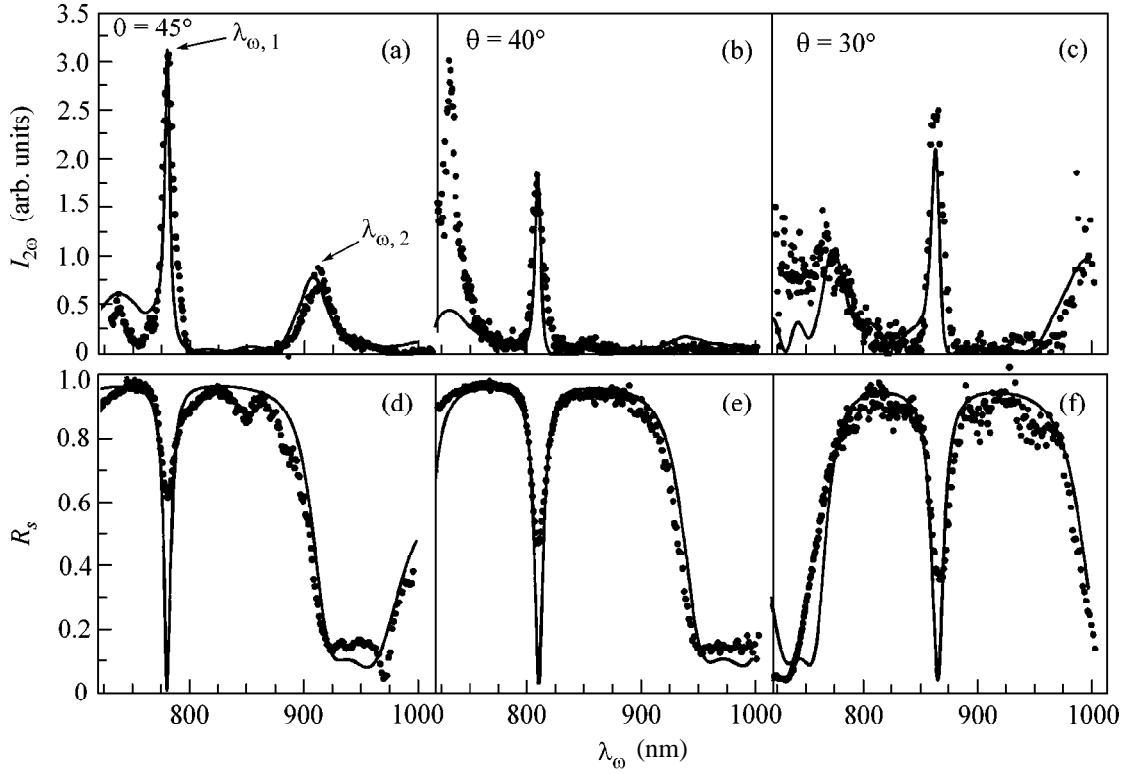
Fig. 2. Intensity of the *p*-polarized SH radiation as a function of the wavelength of *s*-polarized pump radiation, measured in the porous silicon MC at different angles of incidence: θ = (a) 45°, (b) 40°, and (c) 30°. The SH intensities in panels (b) and (c) are given on 7- and 20-fold enlarged scales, respectively. Solid lines are the results of model calculations. Reflectivity spectra are given for the *s*-polarized pump radiation at different angles of incidence: θ = (d) 45°, (e) 40°, and (f) 30°.

smaller. When changing θ to 40° (Fig. 2b) and 30° (Fig. 2c), the SH resonances are shifted to longer wavelengths. This correlates with the angular dependence of the cavity mode in the $R_s(\lambda_\omega)$ spectra (Figs. 2e, 2f). The greatest SH enhancement at the edge of the photonic band gap ($\sim 1 \times 10^2$) is observed at θ = 55° (Fig. 3a).

The spectrum of the SH radiation reflected from the PS microcavity was calculated by using the following phenomenological approach. At the first step, the transfer-matrix formalism was used to solve the problem of multiple interference of pump radiation in a multilayer structure with the dispersion $\varepsilon_{PS}(\lambda)$ calculated for each PS layer in the effective-medium approximation [13] taking the dispersion $\varepsilon_{Si}(\lambda)$ of single-crystal silicon as a basis [14]:

$$(1 - f)\frac{\varepsilon_{Si} - \varepsilon_{PS}}{\varepsilon_{Si} + 2\varepsilon_{PS}} = f\frac{\varepsilon_{PS} - 1}{1 + 2\varepsilon_{PS}}. \tag{1}$$

This was used to calculate the reflection coefficient $R_{s(p)}$ of the polarized pump radiation and the spatial distribution of the amplitude $\mathbf{E}_\omega^{(j)}(z) = \mathbf{E}_\omega^{+(j)}\exp(ik_{\omega,z}^{(j)}z) + \mathbf{E}_\omega^{-(j)}\exp(-ik_{\omega,z}^{(j)}z)$ of the pump standing wave inside the *j*th layer of the microcavity. At the second step, the components of quadratic polarization were calculated for each layer to determine the coupled SH wave field.

It was assumed that the quadratic susceptibility $\chi^{(2)(j)}$ is uniformly distributed inside the *j*th layer and that only the $\chi_{zxx}^{(2)(j)} = \chi_{zyy}^{(2)(j)}$ components are involved in the SH generation by the *s*-polarized pump radiation (the point group of the PS layer was assumed to be ∞m). The spectral behavior of the effective components of quadratic susceptibility was modeled for the *j*th layer by the sum of two Lorentzians, $\chi^{(2)(j)}(2\omega) = (a - b_1/(-\Omega_1 + 2\omega + i\Gamma_1) - b_2/(-\Omega_2 + 2\omega + i\Gamma_2))f_j^{-2}$, with $\hbar\Omega_1 = 3.36$ eV and $\hbar\Omega_2 = 4.3$ eV corresponding to the direct electronic transitions E_0'/E_1 and E_2 in silicon [14]. Next, the nonlinear transfer-matrix formalism, analogous to that applied in [15] to the generation of the third harmonic, was used to solve the problem of interference of the coupled and free SH waves in the *j*th layer and the problem of linear propagation of the SH wave in the structure with multiple interference. The SH amplitude from the whole microcavity was found by summing the SH fields from each of the layers.

The calculated SH and linear reflection spectra are shown in Figs. 2 and 3a by solid lines to demonstrate good qualitative agreement with the experiment. The calculations were carried out for all angles of incidence and the following MC parameters: thicknesses $d_l =$
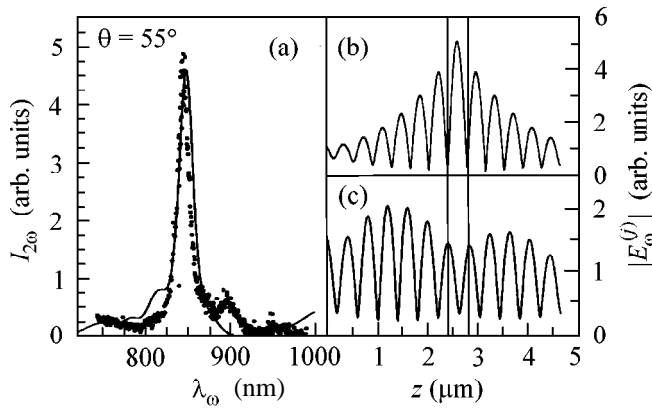
Fig. 3. (a) Intensity of the *p*-polarized SH radiation as a function of the wavelength of *s*-polarized pump radiation, measured in the porous silicon MC at $\theta = 55°$. Solid line is the result of model calculations. (b) Spatial distribution of the pump standing wave amplitude in the MC, calculated for the wavelength $\lambda_{\omega, 1} = 781$ nm corresponding to the microcavity mode at $\theta = 45°$, and (c) $\lambda_{\omega, 2} = 909$ nm corresponding to the edge of the photonic band gap. Vertical lines indicate the boundaries of the cavity layer.

204 nm, $d_h = 165$ nm, and $d_r = 408$ nm and porosities $f_h = 0.774$ and $f_l = f_r = 0.882$. Figures 3b and 3c show the spatial distribution of the absolute value of local amplitude $|\mathbf{E}_\omega^{(j)}(z)|$ of the pump standing wave in the MC at two characteristic wavelengths: $\lambda_{\omega, 1} = 781$ nm (corresponding to the MC mode) and $\lambda_{\omega, 2} = 909$ nm (coinciding with the SH maximum at the long-wavelength edge of the photonic band gap). In the vicinity of $\lambda_{\omega, 1}$, the pump field is mostly localized in the microcavity and the volume energy density of pump radiation exponentially decreases as the outer edges of the PC mirrors are approached. At the wavelength $\lambda_{\omega, 2}$, the pump field is amplified uniformly throughout the MC. Since the induced quadratic polarization is $\mathbf{P}_{2\omega}^{(2)(j)}(z) \propto$ $\mathbf{E}_\omega^{(j)}(z)\mathbf{E}_\omega^{(j)*}(z)$, the resonance enhancement of the SH signal in the vicinity of $\lambda_{\omega, 1}$ is caused by the effects of pump field localization in the MC layer and the adjacent layers of the PC mirrors. Note that, due to the half-wave thickness of the MC layer, its contribution to the SH at $\lambda_{\omega, 1}$ is much smaller than from the nearest lying layers of the PC mirrors, and it is nonzero only due to the dispersion. The increase in the SH intensity in the vicinity of $\lambda_{\omega, 2}$ is caused by the uniform amplification of the pump field. The SH resonance at the short-wavelength edge of the band gap has the same origin: the strong θ dependence of the SH enhancement in this region is caused by the strong dispersion of the PS quadratic susceptibility in the vicinity of 370 nm, which is close to the energy of two-photon resonance of the direct electronic transitions E_0'/E_1 in silicon. This explains why the intensity increase at the edge of the photonic band gap is the largest at $\theta = 55°$ (Fig. 3a).

Thus, when built in the porous silicon photonic crystal, the microcavity layer gives rise to an additional SH resonance, analogous to the resonant increase in the combined density of states for the direct electronic transitions to the impurity level in the semiconductor energy gap. The nonlinear polarization is localized in the vicinity of the microcavity layer. The spectral position of the cavity mode and the radius of localization can be varied by varying the microcavity parameters.

REFERENCES

1. M. Scalora, J. P. Dowling, C. M. Bowden, *et al.*, Phys. Rev. Lett. **73**, 1368 (1994).

2. E. Yablonovitch, Phys. Rev. Lett. **58**, 2059 (1987).

3. A. Imhof, W. Vos, R. Sprik, *et al.*, Phys. Rev. Lett. **83**, 2942 (1999).

4. C. J. Herbert and M. S. Malcuit, Opt. Lett. **18**, 1783 (1993).

5. S. John, Phys. Rev. Lett. **58**, 2486 (1987).

6. V. Berger, Phys. Rev. Lett. **81**, 4136 (1998); N. G. Broderick, G. W. Ross, H. L. Offerhaus, *et al.*, Phys. Rev. Lett. **84**, 4345 (2000).

7. S. Nakagawa, N. Yamada, N. Mikoshiba, *et al.*, Appl. Phys. Lett. **66**, 2159 (1995).

8. A. V. Balakin, V. A. Bushuev, N. I. Koroteev, *et al.*, Opt. Lett. **24**, 793 (1999).

9. L. A. Golovan', A. M. Zheltikov, P. K. Kashkarov, *et al.*, Pis'ma Zh. Éksp. Teor. Fiz. **69**, 274 (1999) [JETP Lett. **69**, 300 (1999)].

10. V. Pellegrini, A. Tredicucci, C. Mazzoleni, *et al.*, Phys. Rev. B **52**, R14328 (1995); M. Cazzanelli and L. Pavesi, Phys. Rev. B **56**, 15264 (1997).

11. L. A. Kuzik, V. A. Yakovlev, and G. Mattei, Appl. Phys. Lett. **75**, 1830 (1999).

12. G. Mattei, A. Marucci, and V. A. Yakovlev, Mater. Sci. Eng. B **B51**, 158 (1998).

13. Yu. E. Lozovik and A. V. Klyuchnik, in *The Dielectric Function of Condensed Systems*, Ed. by L. V. Keldysh, D. A. Kirzhnitz, and A. A. Maradudin (Elsevier, Amsterdam, 1989), Chap. 5, p. 368.

14. D. E. Aspnes and A. A. Studna, Phys. Rev. B **27**, 985 (1983).

15. D. S. Bethune, J. Opt. Soc. Am. B **6**, 910 (1989).

Translated by V. Sakun